An Evaluation of the Mechanical Properties and Microstructure in Uranium Dioxide Doped with Oxide Additives

by

Robert McDonald

A Thesis Presented in Partial Fulfillment
of the Requirements for the Degree
Master of Science

Approved November 2014 by the
Graduate Supervisory Committee:

Pedro Peralta, Chair
Jagannathan Rajagopalan
Kiran Solanki

ARIZONA STATE UNIVERSITY

December 2014

ABSTRACT

The United States Department of Energy (DOE) has always held the safety and reliability of the nation's nuclear reactor fleet as a top priority. Continual improvements and advancements in nuclear fuels have been instrumental in maximizing energy generation from nuclear power plants and minimizing waste. One aspect of the DOE Fuel Cycle Research and Development Advanced Fuels Campaign is to improve the mechanical properties of uranium dioxide (UO_2) for nuclear fuel applications.

In an effort to improve the performance of UO_2, by increasing the fracture toughness and ductility, small quantities of oxide materials have been added to samples to act as dopants. The different dopants used in this study are: titanium dioxide, yttrium oxide, aluminum oxide, silicon dioxide, and chromium oxide. The effects of the individual dopants and some dopant combinations on the microstructure and mechanical properties are determined using indentation fracture experiments in tandem with scanning electron microscopy. Indentation fracture experiments are carried out at room temperature and at temperatures between 450 °C and 1160 °C.

The results of this work find that doping with aluminosilicate produces the largest favorable change in the mechanical properties of UO_2. This sample exhibits an increase in fracture toughness at room temperature without showing a change in yield strength at elevated temperatures. The results also show that doping with Al_2O_3 and TiO_2 produce stronger samples and it is hypothesized that this is a result of the sample containing dopant-rich secondary phase particles.

I would not be where I am today if it wasn’t for the tremendous support I have received over the years. First and foremost, I would like to say thank you to my parents, who always emphasized the beauty of science and ultimately drove me to engineering. To my sister, for all of the good times we’ve had and all of the life lessons I’ve learned from you. To my best friend Eric Liu, you’ve always motivated me to work harder, even if I only did it in order to brag to you later.

Many thanks also go to my coworkers: Andrew Brown, Harn Lim, and the rest of the group. From San Diego to Taco Tuesday to late nights in the lab, I am very grateful to have worked alongside such a smart and funny team. If it wasn’t for your help and support, I’d likely still be stuck running experiments. Special thanks go to my advisor, Dr. Pedro Peralta, for the constant support and guidance he has given me over the years. I have grown in many ways as a student, a scientist, and a person, due to the qualities he demonstrated and the standards he upheld.

And to Bre, thank you for all of the love, support, and care you’ve given me over the years we’ve spent together. You have always been the brightest part of my days. As this chapter ends, a better one is only beginning. I can’t wait to see what it brings.

ACKNOWLEDGMENTS

This project is a part of the Advanced Fuel Cycle Initiative (AFCI) and the Fuel Cycle Research and Development (FCRD). This project was funded by the Department of Energy, Office of Nuclear Energy under grant # DE-NE0000670 and agreement # DE-NE0000134, as well as by Los Alamos National Laboratory, under agreement # DE-AC52-06NA25396.

We gratefully acknowledge the use of facilities with the LeRoy Eyring Center for Solid State Science at Arizona State University.

TABLE OF CONTENTS

Page

CHAPTER

CHAPTER Page

APPENDIX

LIST OF TABLES

LIST OF FIGURES

Figure Page

Figure Page

Figure Page

CHAPTER 1

INTRODUCTION

Uranium oxide is an extremely important material; it is the primary source of fuel for the 435 nuclear power plants (NPPs) operating around the globe producing a large portion of the world's electricity. In total, over 68,000 tons of U_3O_8 (a precursor to UO_2 fuel) are mined each year [1]. Nuclear power is a reliable, sustainable source of energy operating in 31 countries and producing 11% of the world's electricity [2]. In the United States, there were 100 NPPs operating to produce 19% (789 TWh) of the country's annual electricity in 2013 [3]. Nuclear power is also the largest energy source without greenhouse gas emissions in the United States [4]. Since 1950, it is estimated that nuclear power has reduced CO_2 emissions by 28 billion tons [4]. Therefore, from a material point of view, uranium dioxide is a highly utilized resource responsible for a high percentage of the energy required in modern living.

All of the operable NPPs in the United States are classified as light water reactors (LWRs). Among the 100 operating NPPs, 65 are pressurized water reactors and 35 are boiling water reactors [5]. Nuclear power plants take advantage of the heat produced during nuclear fission to produce steam that drives a turbine and generates electrical power. A diagram of a generic pressurized water reactor is shown in Figure 1.1 [6]. A pressurized water reactor has a secondary water loop, whereas a boiling water reactor only has one primary water loop. The diagram in Figure 1.1 shows how the heating cycle works to produce electricity, and a boiling water reactor has many fundamental similarities. Heat produced in the reactor core is used to drive water through the primary loop. In a pressurized water reactor, the primary loop cycles through a heat exchanger that boils water. This produces steam that is then used to rotate a turbine and generate electricity. In a boiling water reactor, the steam in the primary loop is used directly for electricity generation and there is not a need for a heat exchanger.

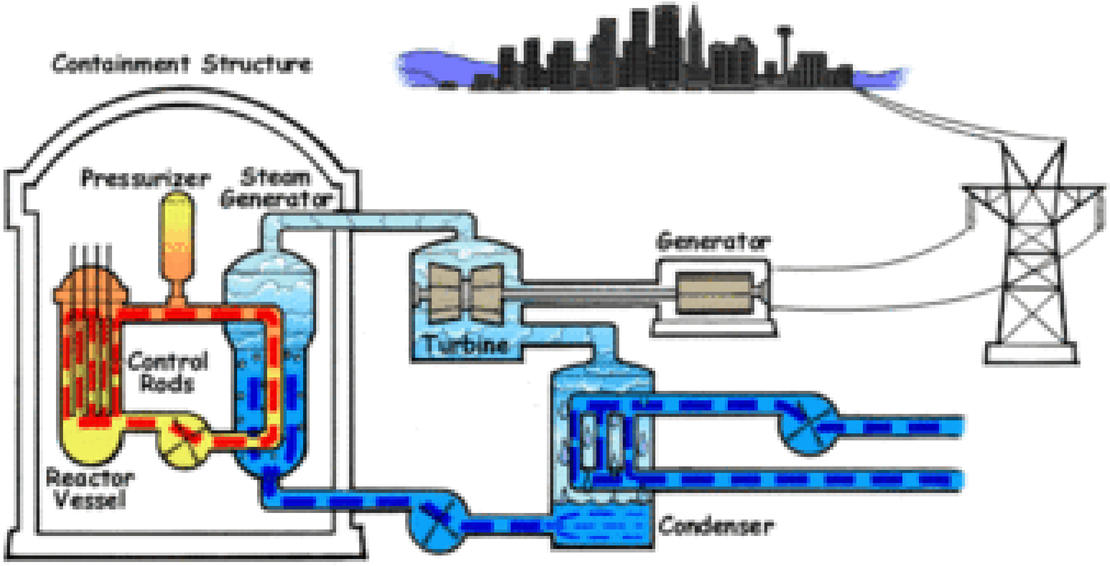

Figure 1.1: Diagram showing the power generation process in a generic NPP [6].

Every light water reactor in the United States uses low-enriched uranium dioxide as fuel. Low-enriched UO_2 contains a maximum of 5% fissile ^{235}U, with the remainder being fertile ^{238}U. High-enriched UO_2, which is used in nuclear submarines and some research reactors, will contain more than 5% ^{235}U. A typical light water reactor fuel rod is shown below in Figure 1.2 [7]. A single fuel rod can contain one to two hundred individual fuel pellets [8]. A fuel pellet is a small cylinder of uranium dioxide, typically 1 cm in diameter and 1.5 cm tall. The fuel pellets are stacked vertically in a fuel rod. At the top of the fuel rod is the plenum, which is an open space provided to accommodate fuel swelling and the various fission gases produced in the fuel during operation.

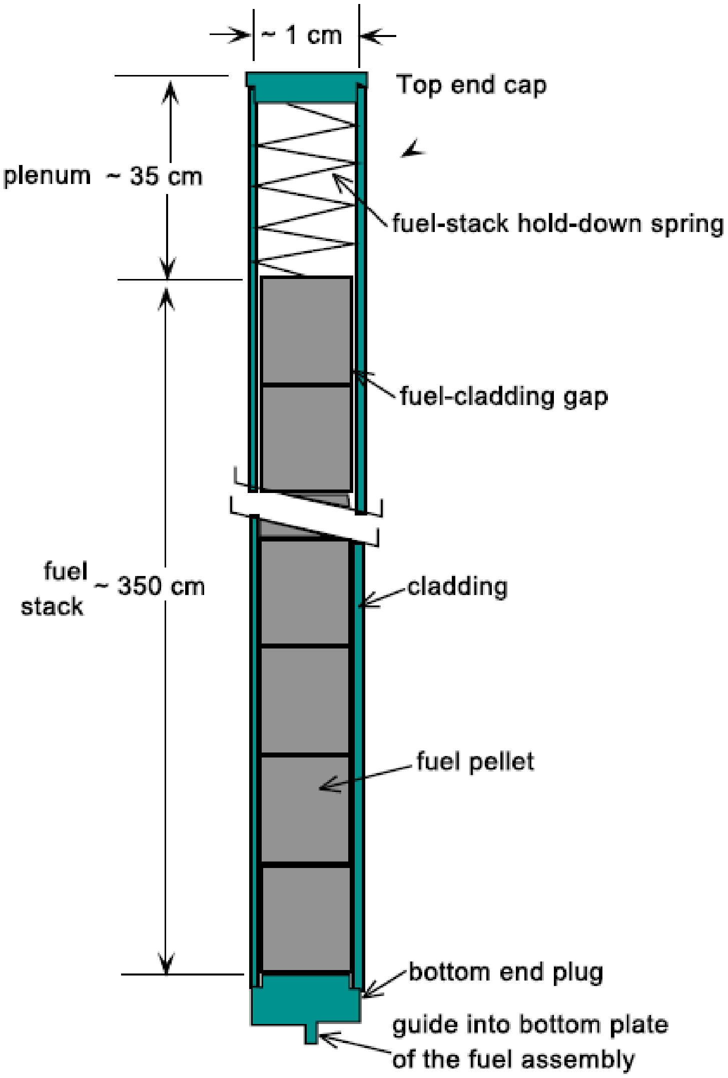

Figure 1.2: Diagram showing the components of a typical fuel rod used in NPP's [7].

Fuel rods are encapsulated in a zirconium/Zircaloy cladding that protects the fuel pellets and prevents them from directly contacting the primary water loop. A spring in the plenum prevents the fuel pellets from moving vertically in the fuel rod. Several hundred fuel rods are bundled together into a fuel assembly that is inserted into the nuclear reactor core. Control rods within the reactor core are used to sustain and manage the nuclear chain reaction and give reactor operators the ability to adjust the energy output of the reactor system [8].

During operation, the reactor core is subjected to an extremely harsh environment. Nuclear fuel operates within a steep radial temperature gradient, from approximately 400 °C at the pellet edge to 1700 °C at the pellet center [9], under a constant flux of neutron bombardment, while withstanding internal pressurization and swelling due to the development of fission gases. The fuel pellets will quickly crack during operation due to thermal stresses and swelling from fission products [7]. Cracking is inevitable and fairly unpredictable, and it can negatively impact the performance and integrity of the fuel bundle [10]. Cracks will grow either radially or circumferentially. A cross-section of an irradiated fuel pellet is shown in Figure 1.3 [9].

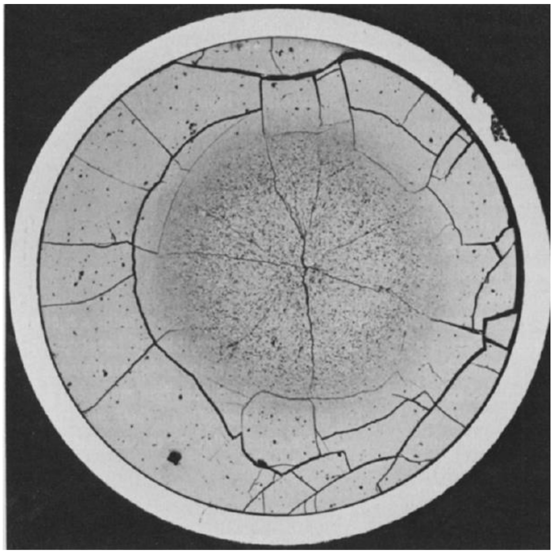

Figure 1.3: An irradiated fuel pellet showing radial and circumferential cracking. Notice

the recrystallization in the central region of the pellet, and the circumferential cracks just outside of that region [9].

Cracks in the material locally diminish the thermal conductivity, and circumferential cracks can retard the release of fission gases by trapping the gas locally within the interior cracks [10]. Circumferential cracks will also result in “hot spots” within the fuel, because the thermal conductivity decreases across the crack, thus trapping heat in the local volume [11].

Fuel cracking can also lead to a more serious problem, namely pellet-cladding interactions (PCI). In PCI, the fuel pellet swells to a point that it is pushing against the cladding, which causes localized stresses and can lead to stress-corrosion cracking (SCC) through interactions at the point of contact [12]. Without delving into too many details about PCI, or the potential SCC mechanisms at play in this scenario, as they are not the main objective of this study, it is important to note that PCI is a fuel-reliability issue that can lead to cladding failure, degradation of the fuel pellets, and the eventual release of fuel into the coolant [12]. Research done in the 1970’s and 1980’s led to the adoption of a pure-zirconium inner cladding tube to significantly reduce the amount of PCI failures [12]. Nonetheless, pellet-cladding interactions pose as a potentially serious problem in nuclear power plants. Figure 1.4 shows PCI that resulted in stress-corrosion cracking in the cladding [7].

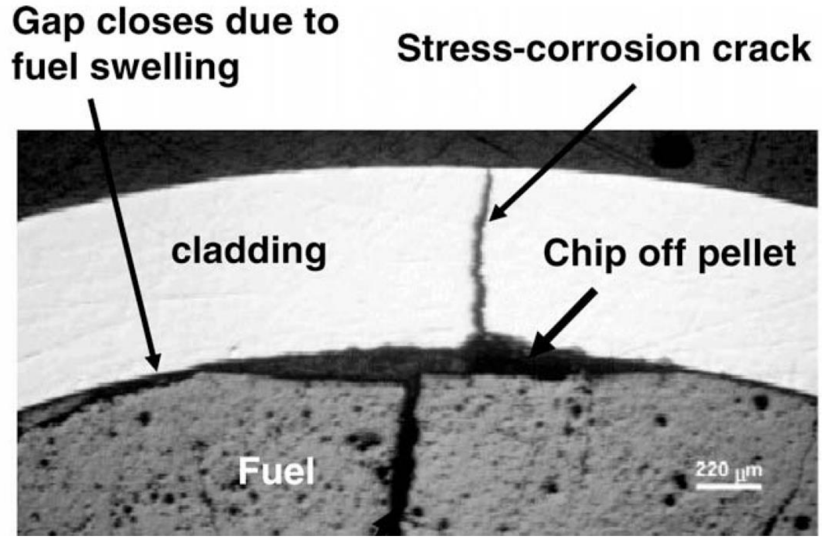

Figure 1.4: Stress-corrosion cracking in fuel cladding due to PCI [7].

With these problems in mind, the work in this thesis is an attempt to mitigate the problems that accompany fuel cracking. The research described in this thesis investigates how to improve the fracture properties of uranium oxide at room temperature as well as at temperatures from 450 °C to 1200 °C. These temperatures were chosen for two distinct reasons. There is an interest in room temperature properties because room temperature acts like a base-line for future studies and experiments on uranium oxide. Also, fuel pellets will occasionally crack and chip during the fuel-loading process. So, a goal of this research is to improve the mechanical properties at room temperature to reduce the potential for cracking during loading. As shown in Figure 1.4, a chipped pellet can lead to localized stresses which drive or accelerate SCC from PCI [7].

The elevated temperature range was chosen because during power operation, the outer portion of the pellet experiences temperatures in this range [9]. Above 1200 °C, uranium oxide has been shown to experience purely ductile fracture, so cracking no longer plays a limiting role in this temperature range [13]. By improving fracture properties, the goal is to reduce the likelihood of brittle fracture and increase the material’s ability to swell without cracking in the outer region during operation.

Nuclear fuel pellets of uranium oxide are typically manufactured using powder compaction and sintering. Controlling parameters such as the pressure during compaction or the time and temperature during sintering are two options for controlling the fuel pellet microstructure to optimize the pellet’s physical and mechanical properties [14]. A more novel approach to control the pellet’s properties is to chemically dope the pellet by introducing specific additive species. Conceptually similar to additives used in metallurgy to enhance mechanical properties, prior studies have shown that adding minute quantities of various oxides to ceramic bodies will have large effects on the mechanical performance and microstructure of the ceramic [15-17].

Before one can understand how the additives affect the material properties, it is essential to build an understanding of how the material typically performs. Due to the global importance of uranium oxide as a nuclear fuel, there is a large, established library of literature that investigates the material, mechanical, chemical and thermal properties of UO_2 across a range of temperatures, compositions, and environments. In the next chapter, several papers and findings are highlighted to establish context and background for this research project.

CHAPTER 2
LITERATURE REVIEW

Uranium oxide has been the subject of numerous research efforts spanning several decades [18-20]. Scientific interest in the material spawned during World War II with the Manhattan Project and a new interest in atomic weapons; since then research has been underway for both atomic weapons and nuclear energy. In the earlier years of nuclear energy research, uranium dioxide received strong support from the U.S. Navy and the Department of Energy due to its ties to nuclear weapons research and development. This propelled the material to become the primary source of nuclear fuel in the United States [21]. This material was chosen because it has a very high melting point, can be easily processed into pellets, and was fairly well understood by the time the first nuclear power plants were being developed.

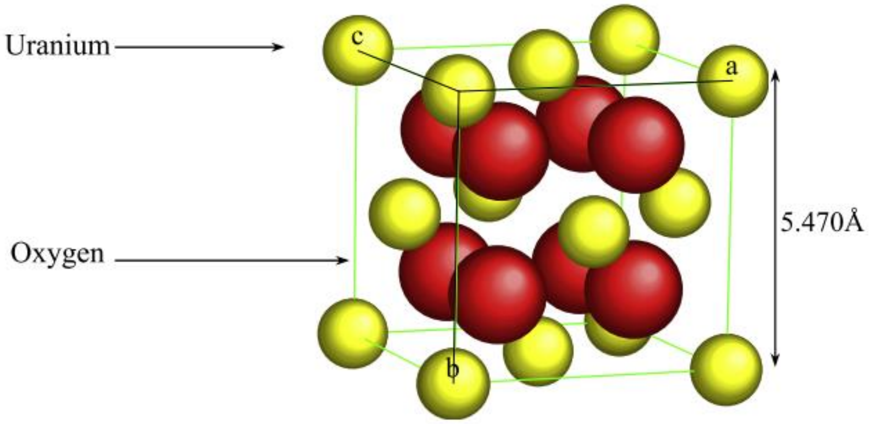

Figure 2.1: Uranium dioxide forms in a fluorite-type crystal structure. The yellow spheres are uranium atoms, and the red are oxygen atoms [22].

Uranium dioxide forms as a cubic structure, specifically the fluorite structure [22]. In Figure 2.1, the uranium atoms are yellow and the oxygen atoms are red. This crystal structure is beneficial because it does not exhibit anisotropy in transferring heat or undergoing thermal expansion [10]. Uranium dioxide is a brittle ceramic that is prone to fracture during handling and operation.

Within the scope of nuclear energy research, many researchers have studied uranium oxide's mechanical, chemical, thermal, and nuclear properties. The next section will provide a brief overview of the mechanical, chemical and thermal properties of uranium oxide, and the following sections will cover how chemical doping has been utilized to alter and improve these properties.

Uranium Oxide Properties

Uranium oxide is a hard, brittle ceramic. Below 600 K, uranium dioxide exists as a stoichiometric compound. At higher temperatures, the phase field allows for a range of oxygen content. Uranium and oxygen can also form phases such as U_3O_8, U_4O_9, and UO_3. A partial uranium-oxygen phase diagram is shown below in Figure 2.2 [18]. Mechanical properties such as Young's modulus, strength, hardness, and fracture toughness have been studied and calculated at various temperatures and with different oxygen contents using methods such as three-point bending, tensile testing, and hardness testing.

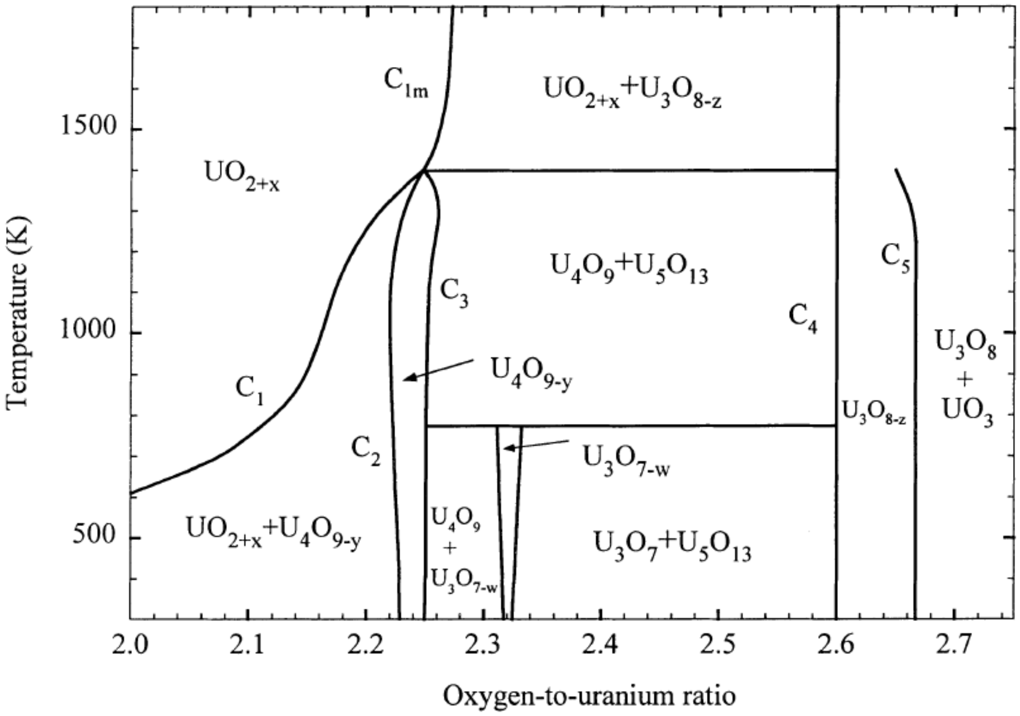

Figure 2.2: U-O phase diagram covering oxygen contents from UO_2 to UO_3 [18].

Young's Modulus

Igata and Domoto measured Young's modulus in uranium oxide at room temperature with respect to porosity, grain size, and excess oxygen and proposed equations dependent on each parameter [20]. These properties were studied by controlling the sintering conditions to produce many different samples with varying densities, grain sizes, and oxygen contents. The equations dependent on oxygen content are not presented here, as the samples used in this study are all near stoichiometry and secondary uranium oxide phases are not present. The authors used an ultrasonic attenuator to measure the Young's modulus and found that it is dependent on porosity and excess oxygen and minimally affected by grain size [20]. The Young's modulus for a stoichiometric, non-porous sample was found to be 219.6 GPa, and its dependence on porosity is described by Equation 2.1 [20]. In Equation 2.1, P refers to the fractional amount of porosity (P = 1 - %TD).

$$E = 2.196 * 10^5 e^{-3.025P}\ (MPa) \qquad \text{(Equation 2.1)}$$

Fracture Strength

Igata and Domoto also reported on the compressive fracture strength of UO_2 with respect to porosity and grain size [20]. Compression testing was used in determining the compressive strength. Here, the term d refers to grain size in cm. Equation 2.2 and Equation 2.3 describe the compressive strength's dependence on porosity and grain size, respectively [20]. A 97% dense pellet will have a strength of 960 MPa, and a pellet with an average grain size of 8 µm will have a strength of 925 MPa.

$$S = 1.067 * 10^3 e^{-3.505P}\ (MPa) \qquad \text{(Equation 2.2)}$$

$$S = 6.92 * 10^2 + 6.60 d^{-1/2}\ (MPa) \qquad \text{(Equation 2.3)}$$

Additionally, Evans and Davidge studied the fracture strength of polycrystalline UO_2 using three-point bend testing, this time investigating its dependence on temperature [13]. In these experiments, several three-point bend specimens were produced, some with an average grain size of 8 µm, others with an average grain size of 25 µm. Both were sintered until reaching a 97%TD. The fracture stresses were calculated from the outer fiber stresses during the three-point bend tests. The authors found that UO_2 underwent a ductile-to-brittle transition temperature between 1200 and 1300 °C, yet extensive plastic flow prior to fracture was reported in tests done above 800 °C [13]. In the small-grained samples, the fracture strength was constant from room temperature up to ~450 °C, and then increased until reaching a peak at ~800 °C. Between 800 °C and 1200 °C, the authors conclude that the fracture strength is similar to the yield strength [13]. Below ~800 °C, the fracture strength is lower than the yield strength, thus the fracture is (mostly) brittle. At room temperature, the authors found the fracture strength to be from 150-180 MPa [13]. This is shown schematically in the Figure 2.3 below [13].

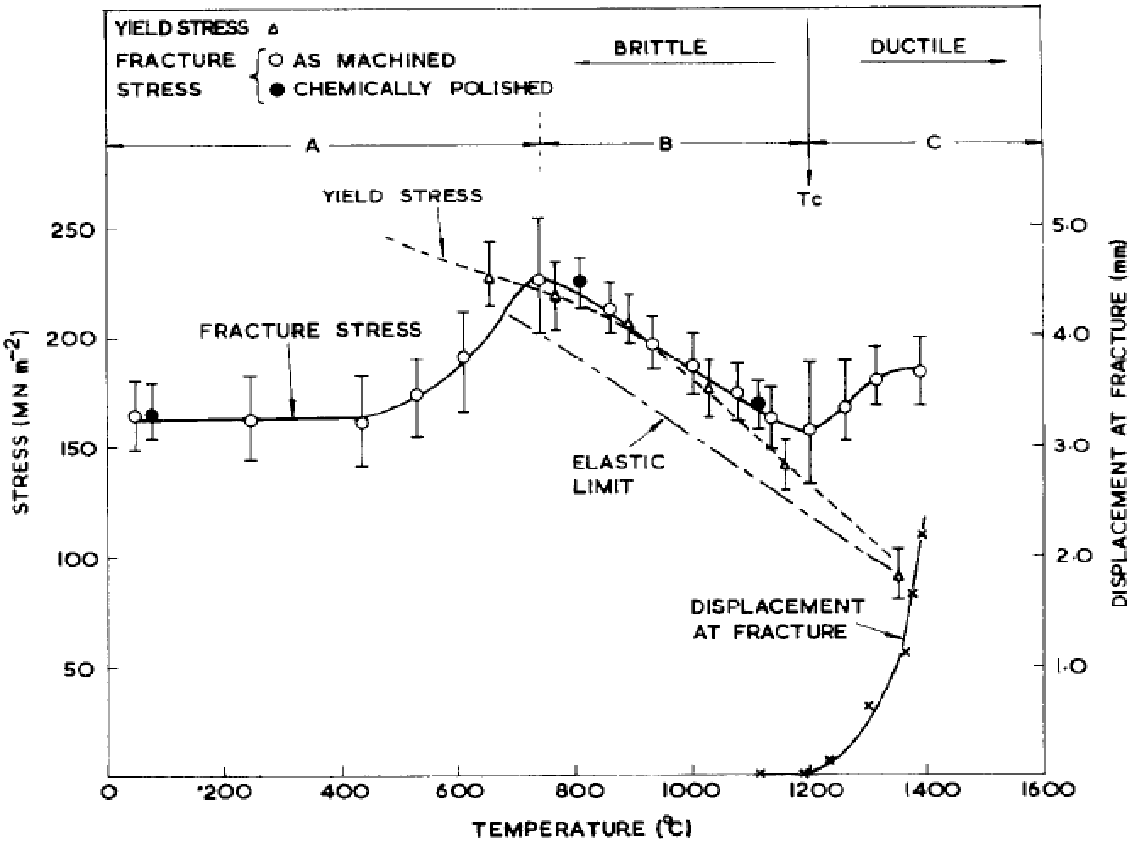

Figure 2.3: Stress-to-failure in UO_2 at temperatures from 25 °C to 1400 °C [13].

The strength reported by Evans and Davidge is five times lower than the strength reported by Igata and Domoto [13][20]. The difference arises because Evans and Davidge studied the fracture strength in UO_2 through three-point bend testing, whereas Igata and Domoto only studied the fracture strength in UO_2 under compressive loading.

Fracture Toughness

There has not been a very large effort to study the fracture toughness in uranium oxide, though a few reports do exist. Kutty et al. [23] used Vickers indentation with equations established by Anstis et al. [24] to study fracture toughness and fracture surface energy in UO_2 samples with different densities. Their indents were done with 294 N loads, producing radial cracks beneath the sample surface. Using least squares analysis, the authors fit an equation to their findings, relating fracture toughness to porosity. The authors found that fracture toughness increased with porosity, and ranged from 0.88 to 1.20 MPa√m [23]. These findings were used to determine the fracture surface energy, using an equation established by Warren [25], and the authors produced an equation relating the fracture surface energy to porosity. Likewise, the fracture surface energy increased with porosity. The authors also introduced a new parameter, the fracture modulus, which is a ratio of the fracture toughness and fracture surface energy [23]. This value should be constant for a material, and their values were nearly constant at ~0.42 [23].

Matzke, Inoue and Warren have also investigated the fracture surface energy of UO_2, using spherical indentation [26]. In this study, samples were made with oxygen to metal ratios (O/M) contents varying from 1.989 to 2.052, yet all contained larger grains, with an average grain size of 20 ± 5 µm, and only 2.7% porosity [26]. For the stoichiometric UO_2, the average fracture surface energy was determined to be 1.8 J/m^2, and using the equation derived by Warren [25], the average fracture toughness was calculated to be 0.91 MPa√m [26]. This value falls within the range found by Kutty et al [23]. Average fracture toughness was not significantly affected by oxygen content, though Matzke and Inoue report a slight increase in fracture toughness with oxygen content [26]. Their data is shown in Figure 2.4 below, and it is apparent that the average fracture toughness values are all within the error range at nearly every O/M ratio [26]. Other researchers have calculated the fracture surface energy of UO_2 and values range from 0.60 to 1.54 J/m^2 [23-27].

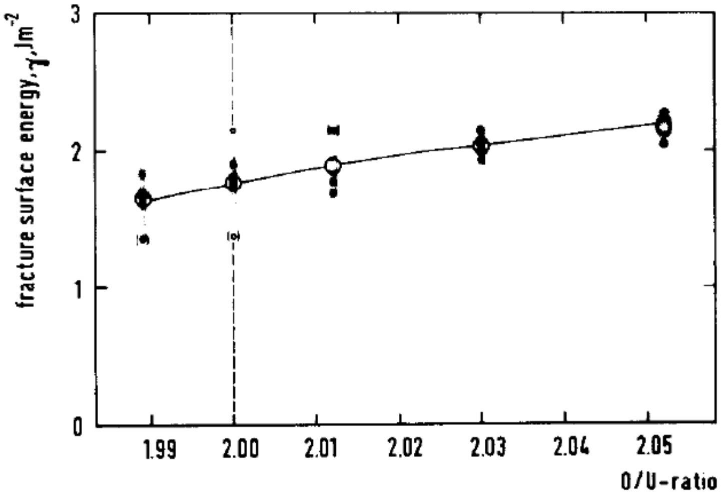

Figure 2.4: Dependence of fracture toughness on the O/M ratio in uranium oxide [26].

Thermal Conductivity

In nuclear energy research, there has always been serious interest in understanding and improving the thermal conductivity of UO_2. One of the detracting factors in using uranium oxide as a nuclear fuel is its low thermal conductivity, which decreases with increasing temperature, up until its melting point [27]. The center of the fuel pellet will be extremely hot, upwards of 1500 °C, and the outer edge of the fuel pellet will be between 300 and 500 °C. This becomes an interesting problem, as heat is being generated within the material and flowing outward towards the cladding, yet the thermal conductivity is the lowest at the pellet center and increases radially outwards.

Fink wrote a very good review paper of the thermo-physical properties of UO_2 in 2000, in which the author takes an in-depth look at the previously reported thermal conductivity data and recommend an equation for thermal conductivity of 95% dense UO_2 established by Ronchi et al. [27, 28]. Thermal conductivity is dependent on temperature and density, and can be expressed as [27]:

$$\lambda = \frac{100}{7.5408+17.692t+3.6142t^2} + \frac{6400}{t^{5/2}} \exp\left(-\frac{16.35}{t}\right) \qquad \text{(Equation 2.4)}$$

Where t = T(K)/1000. Equation 2.4 fits very well with the experimentally established data. In the plot below, the polynomial fit is compared to thermal conductivity measurements in 95% dense UO_2 [28]. Using Equation 2.4 above, the thermal conductivity at room temperature is calculated to be 7.6 W/mK, and it reaches a minimum of ~2.0 W/mK at approximately 1900 K [28].

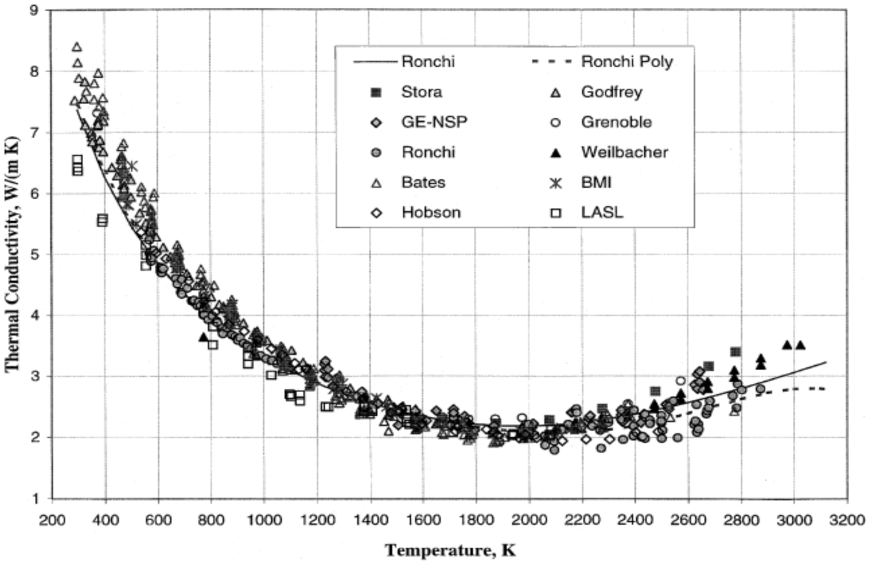

Figure 2.5: A comparison of thermal conductivity data and Equation 3.4 in UO_2 [28].

Diffusion in UO_2

A review paper by Belle compares the coefficients of uranium and oxygen self-diffusion determined through a variety of experimental techniques [29]. Uranium and oxygen self-diffusion in uranium oxide is highly dependent on oxygen content. Belle performed a least-squares regression analysis on three sets of published data for oxygen self-diffusion and established Equation 2.5 as the diffusion equation for near-stoichiometric UO_2 [29]:

$$D = 1.15 * \exp\left(-56700 \pm \frac{1000}{RT}\right) \quad \left(\frac{cm^2}{\sec}\right) \qquad \text{(Equation 2.5)}$$

In hyper-stoichiometric UO_2, the excess oxygen is accommodated in three unique interstitial sites within the lattice [30]. In hyper-stoichiometric samples, experimental measurements found the oxygen self-diffusion coefficients to be highly dependent on the extent of hyper-stoichiometry. A series of papers by Thorn and Winslow [31, 32] present a good equation, Equation 2.6, showing the dependence of the oxygen self-diffusion coefficient on oxygen content [31]. In Equation 2.6, x is the molar fraction of oxygen interstitials.

$$D = 0.02016\left(x + \left[x^2 + 500\exp\left(-\frac{40900}{RT}\right)\right]^{\frac{1}{2}}\right)\exp\left(-\frac{35100}{RT}\right)\ \left(\frac{cm^2}{\sec}\right) \quad \text{(Equation 2.6)}$$

The review paper by Belle found that there was poor agreement among the sets of data for uranium self-diffusion [29]. This lack of agreement is attributed to limitations in the experimental methods which were used, as well as poor control over the specimen stoichiometry. In nominally stoichiometric UO_2, the activation energy of uranium self-diffusion ranged from 70 kcal/mol to 105 kcal/mol [29]. This was partially attributed to the effects of grain boundaries; while others suggested that impurities might be affecting the diffusion measurements [33]. The most accurate equation is found to be one determined by Hawkins and Alcock for near-stoichiometric UO_2 [34]. This equation is provided as Equation 2.7.

$$D = 2.04 \times 10^{-3}\exp\left(-\frac{88900}{RT}\right) \qquad \left(\frac{cm^2}{sec}\right) \qquad \text{(Equation 2.7)}$$

Fission gas diffusion and release from UO_2 has been extensively studied for several decades. In 1980, Matzke published an in-depth review of the research thus far [35] in an attempt to make sense of the unexpected scatter in data seen by other authors [36]. In this review, Matzke attempted to determine an effective diffusion coefficient for fission gases such as Xe and Kr. Fission gas diffusion is complicated by the species and relative concentrations of different gases, the stoichiometry of the uranium oxide, the burn-up of the fuel, and a number of other items [35]. In a separate report by Kashibe and Une, the diffusion coefficient of ^{133}Xe fission gas in near-stoichiometric UO_2 is determined to be [17]:

$$D = 1.7 \times 10^{-12} \exp\left(-\frac{235\left(\frac{kJ}{mol}\right)}{RT}\right) \qquad \left(\frac{m^2}{\mathrm{sec}}\right) \qquad \text{(Equation 2.8)}$$

Research done by Une et al. showed that the diffusion coefficient in UO_2 will increase by a factor of ~3 when the O/U ratio changes from 2.000 to 2.001 [37]. This is in agreement with previous work that showed a tendency for physical properties to greatly change if the material deviated even slightly from stoichiometry [19].

Effects of Dopants on the Behavior of UO_2

There have been efforts by several different research groups to study the effects of doping on different properties of uranium dioxide. These efforts have focused on how dopants affect properties such as thermal diffusivity, fission gas release, grain size, and creep strength. Several papers have specifically shown that adding minute amounts (from 0.05 to 0.2 wt%) of different oxides to uranium dioxide will noticeably alter the material's thermo-mechanical and microstructural properties. A variety of additives have been used with differing levels of success. Some papers contradict the findings of other researchers, and there are disagreements on how and why certain additives perform favorably over others. Here, several of these papers are reviewed and compared.

Microstructural Effects

An addition of 0.5 wt% of TiO_2 to UO_2 has been shown to cause expedited grain growth during sintering, such that the average grain size is three times larger than that of a control sample sintered under the same conditions [38]. This fact has been proven and published several times, yet it is still under debate as to why exactly TiO_2 enhances grain growth so significantly [38, 39].

In a 1964 paper by Arthur and Scott, the authors conclude that during sintering, TiO_2 acts as a liquid-phase sintering aid which greatly enhances grain growth [39]. This study was performed with samples containing between 20 and 60% TiO_2, and sintering was done at temperatures above the melting point of TiO_2 (1645 °C). Yet enhanced grain growth is seen in samples containing as little as 0.1 wt% TiO_2 and sintered below 1645 °C, so another diffusion-enhancing mechanism must be present [38]. Arthur and Scott also reported that during sintering, TiO_2 is reduced to $TiO_{1.57}$, and this free oxygen is absorbed by the uranium oxide lattice [39]. Furthermore, a later paper by Lidiard establishes a model that shows that the self-diffusion coefficient of uranium will increase with the square of x (from UO_{2+x}) [33]. Using this information with the experimental data, Amato reasons that the increased grain growth is likely caused by an increase in the uranium self-diffusion rate which occurs due to the absorption of excess oxygen freed from the TiO_2 additive during sintering [38]. Figure 2.6 shows the massive difference in grain size between pure UO_2 and 0.5 wt% TiO_2-UO_2 samples [38].

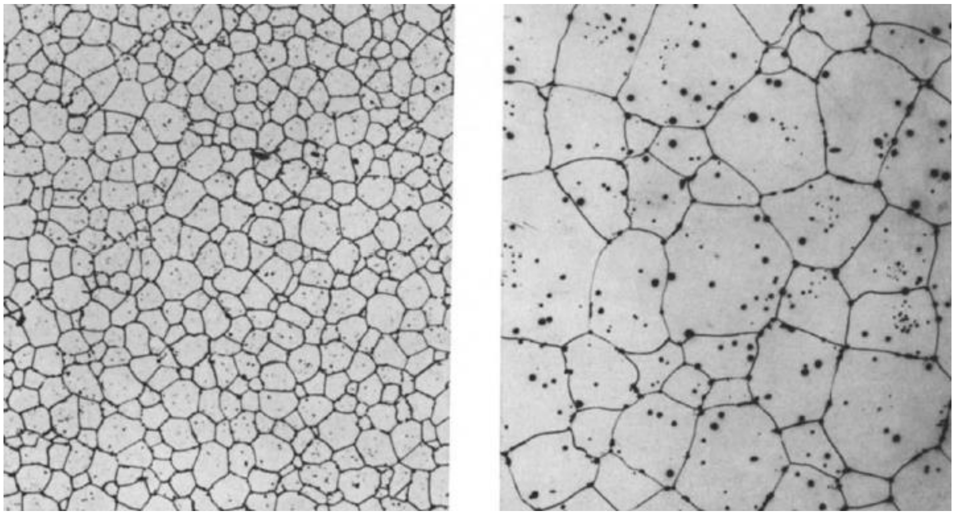

Figure 2.6: Micrographs of pure UO_2 (left) and 0.5 wt% TiO_2-UO_2 (right). 250 X [38].

The converse was seen in UO_2 pellets doped with V_2O_5, where grain growth was inhibited by the doping [40]. In this report by Amato and Ravizza, sample pellets were made containing 0.68, 1.38 and 2.10 wt% V_2O_5 that were sintered for various lengths of time. Pellet density and grain size were studied at different time steps during sintering. This publication concluded that V_2O_5 would on average reduce the grain size by at least half without having a significant effect on the pellet density [40]. Figure 2.7 below shows the microstructures of an un-doped control sample in comparison with the 2.10 wt% V_2O_5-UO_2 sample [40]. This highlights the major change in grain size due to the V_2O_5 additive. A paper with the opposite conclusion was published in 1983 by Radford out of Westinghouse Research Labs [41]. This research found that the addition of vanadium oxide led to sample pellets with a larger average grain size. Contrary to the Amato publication, an increase in grain size was shown to be directly correlated to an increase in the concentration of V_2O_5 [41].

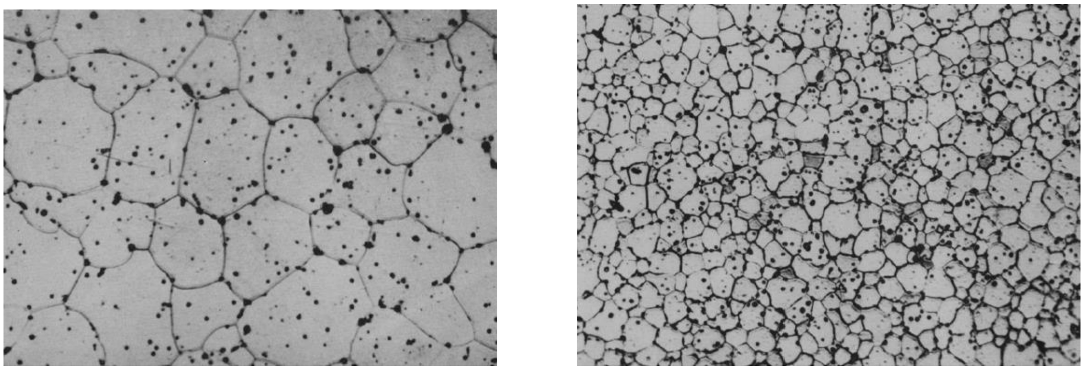

Figure 2.7: Micrographs showing the difference in grain size for pure UO_2 versus 2.1 wt% V_2O_5-UO_2. 300 X [40].

Westinghouse Electric Co. has recently published papers detailing how chromium oxide, magnesium oxide, and aluminum oxide facilitate pellet densification during sintering and promote accelerated grain growth [16]. Some of the physical properties of the samples studied by Arborelius et al. are shown in Table 2.1 on the next page [16]. Their research found that these additives have a positive effect on densification and produce samples with four to five times the grain size, yet the additives do not significantly impact important physical properties such as heat capacity, melting temperature, or the coefficient of thermal expansion. Note that the specimens doped with Cr_2O_3 and Cr_2O_3 + Al_2O_3 led to a large increase in grain size. This research was part of the Westinghouse ADOPT (Advanced Doped Pellet Technology) program, and these findings have been implemented in fuel pellets used in commercial nuclear power plants [16].

Table 2.1: Physical properties of ADOPT pellets. Doping led to increased grain size [16].

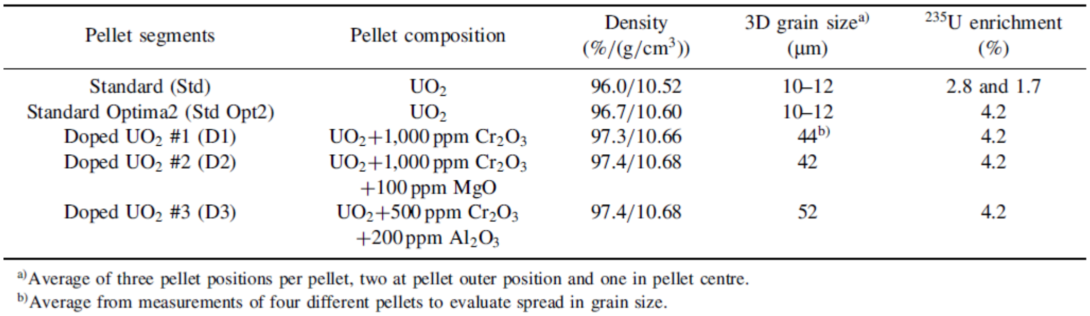

Pellet segments	Pellet composition	Density (%/(g/cm^3))	3D grain size$^{a)}$ (μm)	^{235}U enrichment (%)
Standard (Std)	UO_2	96.0/10.52	10–12	2.8 and 1.7
Standard Optima2 (Std Opt2)	UO_2	96.7/10.60	10–12	4.2
Doped UO_2 #1 (D1)	UO_2+1,000 ppm Cr_2O_3	97.3/10.66	44$^{b)}$	4.2
Doped UO_2 #2 (D2)	UO_2+1,000 ppm Cr_2O_3 +100 ppm MgO	97.4/10.68	42	4.2
Doped UO_2 #3 (D3)	UO_2+500 ppm Cr_2O_3 +200 ppm Al_2O_3	97.4/10.68	52	4.2

$^{a)}$Average of three pellet positions per pellet, two at pellet outer position and one in pellet centre.

$^{b)}$Average from measurements of four different pellets to evaluate spread in grain size.

Fission Gas Diffusion

There has also been an interest in researching how different additives affect gas diffusion and release in UO_2. In one publication by Kashibe and Une, four different additives were used to probe how they altered the diffusional release of ^{133}Xe from lightly irradiated UO_2 fuels [17]. The researchers added 0.065 wt% Cr_2O_3, 0.076 wt% Al_2O_3, 0.085 wt% SiO_2 and 0.50 wt% MgO to sample fuel pellets. After sintering, the concentration of each additive was measured using inductively coupled plasma emission spectrochemical analysis.

It was found that less than half of the Cr_2O_3 additive and only 27% of the Al_2O_3 additive was retained in the sample, whereas the SiO_2 and MgO additives were 82% and 96% retained, respectively [17]. This is an interesting point to note because it shows a very significant difference in the actual additive concentration and the nominal concentration. Kashibe and Une determined that Al_2O_3 and MgO had almost no influence on the fission gas diffusion rate, Cr_2O_3 increased the diffusion coefficient by about three times compared to the un-doped sample, and SiO_2-doping decreased the diffusion coefficient by approximately one order of magnitude [17]. The authors reason that Al_2O_3

does not affect the diffusion rate because it is insoluble in UO_2, thus it cannot affect diffusion through the matrix. They found that MgO did not affect the diffusion rate, even though it is soluble in UO_2, because it forms nanometer precipitates in the grain interiors which are ineffective in altering diffusion. It was reasoned that Cr_2O_3 enhances diffusion by introducing excess uranium vacancies into the lattice, and that SiO_2 suppresses diffusion by introducing oxygen vacancies into the lattice [17]. In research by Une, it is found that adding 0.5 wt% Nb_2O_5 enhances the diffusion coefficient of ^{133}Xe in UO_2 by a factor of 50, and adding 0.2 wt% TiO_2 enhances the diffusion coefficient by a factor of 7 [37].

Thermal Conductivity

The effect of additives on thermal conductivity has been modeled before, based on how the additive species locally distorts the crystal lattice. In a paper by Klemens, an equation is obtained that models the thermal conductivity of a material containing defects at temperatures in the upper range where phonon scattering by point defects is stronger than scattering by the lower-temperature umklapp processes [42]. In a 2014 review report by Massih, this model is used to study the effects of Cr_2O_3-doping and Gd_2O_3-doping on the thermal conductivity of UO_2 [43]. A decrease in thermal conductivity is shown to be directly proportional to the concentration of the added dopant. Additives with a larger ionic radius difference from UO_2 will show a more pronounced change in thermal conductivity, so the calculations done by Massih showed that Cr_2O_3-doping has a larger effect than Gd_2O_3-doping in UO_2 [43]. This effect decreases with increasing temperature [42]. In Figure 2.8, the thermal conductivity is calculated over a large temperature range for various concentrations of Gd_2O_3. The effects are marginal at best below a concentration of 0.2wt% Gd_2O_3. With respect to thermal conductivity, the effects of a dopant are likely to be overshadowed by the effects of density and porosity within the UO_2 matrix.

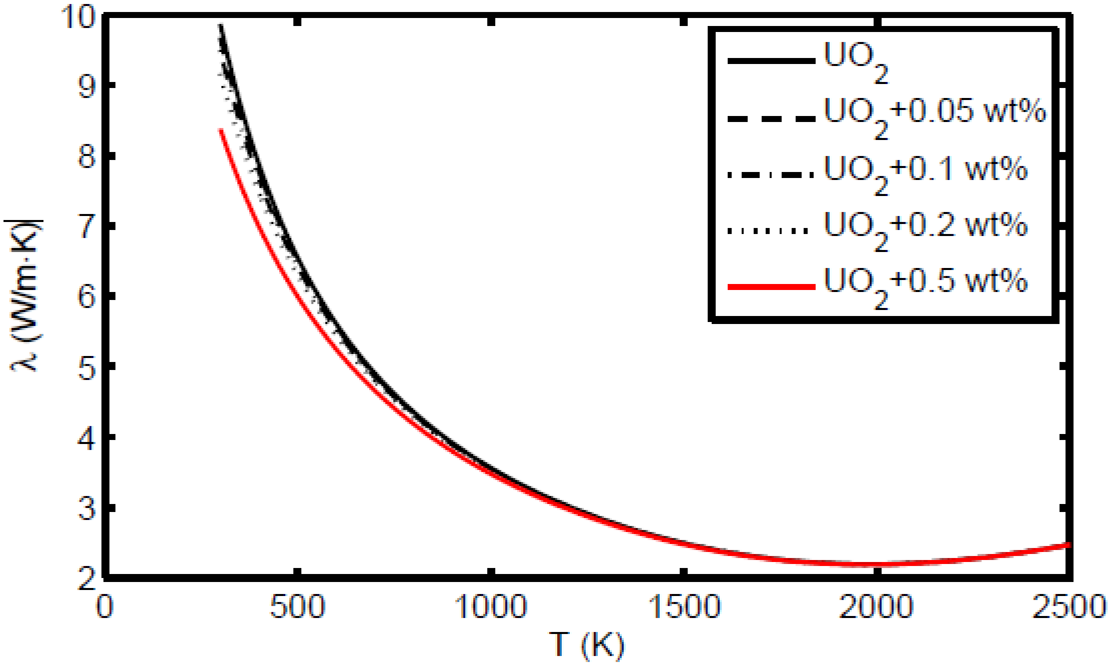

Figure 2.8: Effects of Gd_2O_3-doping on thermal conductivity in UO_2 [43].

Mechanical Properties

One of the first studies into how additives affect the mechanical properties of UO_2 was done in 1981 by Sawbridge et al. at Berkeley Nuclear Laboratories in the UK [44]. The researchers fabricated UO_2 samples containing various concentrations of Nb_2O_5 ranging from 0.1 to 1.0 mol%. Compression creep testing was performed in the stress range of 0.5 to 90 MPa at temperatures between 1150 °C and 1300 °C. At stresses below 70 MPa, they reported that the steady state creep rate was linearly dependent on stress, typical of the diffusion creep mechanism, and that the Nb_2O_5 additions caused a dramatic increase in the steady state creep rate [44]. Samples containing 0.4 mol% Nb_2O_5 showed a creep rate three orders of magnitude higher than the un-doped sample [44]. This is indicative of a softer material, which is desirable in the nuclear reactor environment. The authors conclude by stating that the increase in the creep rate (through the inclusion of Nb_2O_5) can be attributed to the modification of the defect structure by the addition of Nb^{5+} ions, but that these ions will be rapidly reduced in an oxygen-reducing environment, which results in the creep rate reverting back to the rate seen in the un-doped uranium dioxide samples [44].

Studies done by Dugay in 1998 [45] and Nonon in 2004 [46] investigated how Cr_2O_3-doping altered the thermal creep performance in UO_2 at stresses ranging from 20 to 70 MPa. Both research efforts found that Cr_2O_3 additions will greatly increase the steady state creep rate, yet there is a large scatter in the data. Stress-strain curves from creep tests performed at 1500 °C for samples doped with different concentrations of Cr_2O_3 are shown in the Figure 2.9 on the following page [45]. These experiments were done with a constant applied strain rate of 20 µm/min, and it is apparent that the creep stress is strongly affected by the Cr_2O_3 additives.

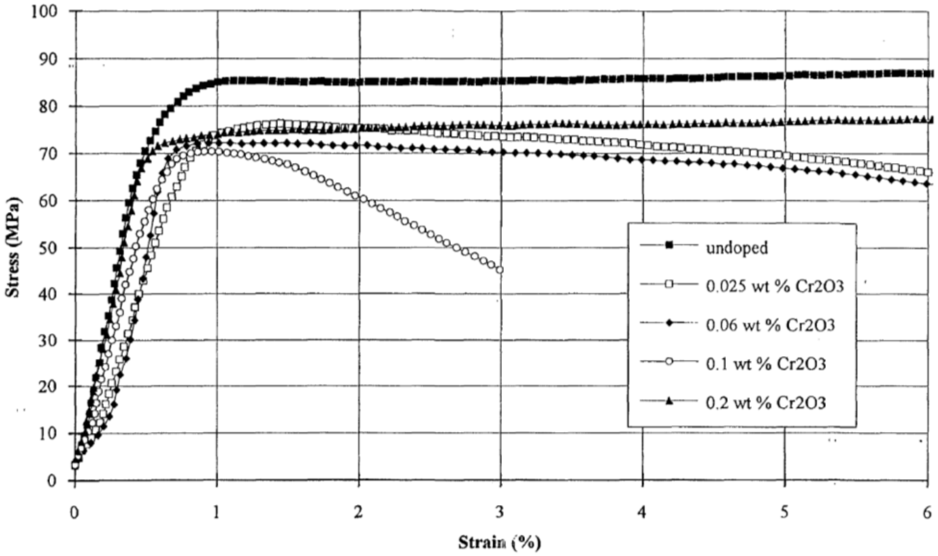

Figure 2.9: Stress-strain curves from creep testing done at 1500 °C for UO_2 doped with different amounts of Cr_2O_3 [45].

Other researchers have studied creep in UO_2 doped with additives such as Al-Si-O and SiO_2-CaO-Cr_2O_3 [47, 48]. Creep testing is the primary method for studying mechanical behavior in doped-UO_2, and there has not been any prior work done using indentation to study how doping affects the material hardness in doped-UO_2.

Indentation Fracture Toughness

Indentation is a powerful and practical tool that can reveal more about a material than just hardness. Below, several publications on analyzing fracture toughness and yield strength from sharp indentation, such as Vickers or Berkovich, are compared and reviewed.

Analyzing fracture toughness in brittle materials can be done using a number of different experimental and analytical methods. Some methods for calculating fracture toughness utilize techniques such as fatigue testing, three-point bending, tensile testing, and finite element analysis. In this thesis, indentation fracture is used to study fracture toughness. This method has several benefits when compared to other experimental methods, as it is a quasi-non-destructive test that probes a very small volume, such that measurements can be repeated several times on a single sample without compromising its overall integrity. Therefore, indentation allows the researcher to maximize the amount of information that can be obtained while only using a minimal amount of material.

Indentation fracture is a relatively new technique for studying fracture toughness. With this technique, the fracture toughness (K_{IC}) of a material can be analyzed by measuring the hardness and crack lengths from a single Vickers indent. Several equations have been derived which attempt to best fit experimental data, and it is imperative to use the correct equation when analyzing fracture toughness. Indents will result in one of two types of cracking, median (half-penny) or Palmqvist (radial) cracks. These cracking types are shown in Figure 2.10 on the following page.

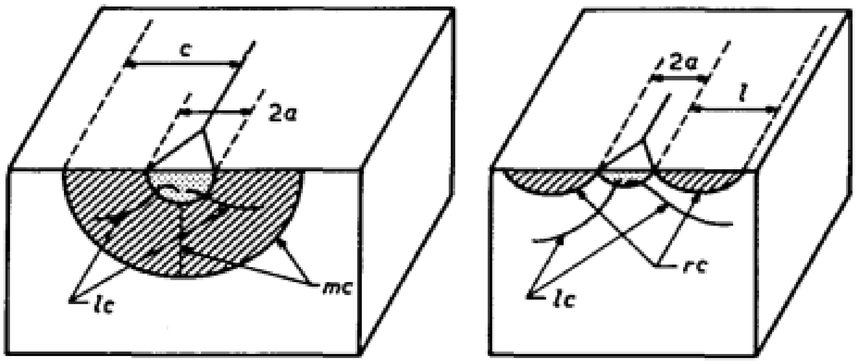

Figure 2.105: The different cracking types from indentation. Left: Median "half penny" cracking. Right: Radial "Palmqvist" cracking [49].

Median cracks often form in brittle materials indented under large loads. Palmqvist cracks form in composite materials and materials indents with low loads (≤ 1 kgf). Equations have been built to specifically handle each type of indentation cracking. If analysis is done correctly, indentation fracture tests can be a very useful tool for making comparisons between fracture toughness' for different materials.

Indentation fracture tests were recognized in the late 1950's by Palmqvist [50] as a way to potentially quantify material toughness, yet an accurate empirical equation was not established until Evans and Charles published their findings in 1976 [51]. Their equation is given below as Equation 2.9.

$$K_{IC} = 0.16H\sqrt{a}\left(\frac{c}{a}\right)^{-1.5} \qquad \text{(Equation 2.9)}$$

The Evans and Charles equation fit a large amount of published data, but the equation was established for median cracking and was inaccurate for low-load indents and materials which exhibited Palmqvist cracks rather than median cracks [51]. Figure

2.11 demonstrates how some experimental data (in the low c/a-ratio range) deviated from the Evans and Charles equation [49].

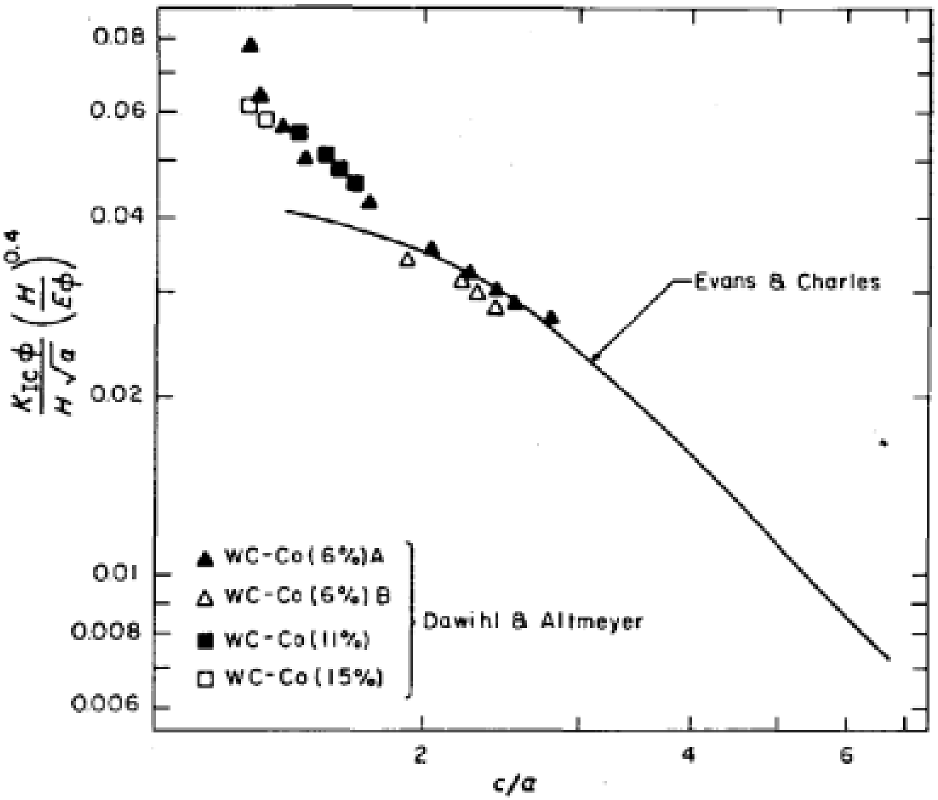

Figure 2.11: Evans and Charles fracture toughness model is compared to experimental data for WC-Co composites. The model deviates from the data at low c/a-ratios [49].

From 1976 through the middle of the 1980's, there were several efforts to develop an improved equation for indentation fracture toughness. In 1981, Anstis et al. [24] published an experimentally-derived equation which improved upon the Evans and Charles equation yet still emphasized median cracks over Palmqvist cracks. The equation established by Anstis is shown below as Equation 2.10 [24].

$$K_{IC} = 0.028(Ha^{0.5})\left(\frac{E}{H}\right)^{0.5}\left(\frac{c}{a}\right)^{-1.5} \qquad \text{(Equation 2.10)}$$

In 1982, Niihara, Morena and Hasselman published a paper that experimentally established an equation for analyzing Palmqvist cracks from Vickers indentation [49]. Their goal was to define an equation which described the data that deviated from the Evans and Charles equation. In the same year, Lankford published a paper with his attempt to form a “universal” equation that would adequately fit both types of cracking [52]. Below, is the Niihara equation (Equation 2.11) [49] followed by the Lankford equation (Equation 2.12) [52].

$$K_{IC} = \frac{0.035}{\emptyset} H\sqrt{a}\left(\frac{H}{\emptyset E}\right)^{-0.4}\left(\frac{l}{a}\right)^{-0.5} \qquad \text{(Equation 2.11)}$$

$$K_{IC} = \frac{0.142}{\emptyset} H\sqrt{a}\left(\frac{H}{\emptyset E}\right)^{-0.4}\left(\frac{c}{a}\right)^{-1.56} \qquad \text{(Equation 2.12)}$$

In this thesis, the Niihara equation (Equation 2.11) is used for calculations of fracture toughness from Vickers indentation. It most accurately represents the physical system of low-load indents in uranium oxide, as the indentation fracture experiments in this present work only show Palmqvist cracking.

Berkovich indents can be similarly analyzed for fracture toughness. In a paper by Dukino [53], comparisons were made between Vickers fracture toughness and Berkovich fracture toughness for a number of different materials. The author concluded that Berkovich indents have a greater extent of cracking than Vickers indents, and that fracture toughness estimates from Berkovich indents are more consistent than from Vickers [53].

Dukino found that fracture toughness from Berkovich indents are best described using an equation established by Laugier [54] with a modification proposed by Ouchterlony [55]. It was shown that Berkovich indents are more likely than Vickers indents to produce Palmqvist cracks due to the nonsymmetrical geometry around the indent which prevents median cracks from forming [53]. The Ouchterlony modification accounts for the number of radial cracks emanating from the central point load [55]. Using the Laugier equation with the Ouchterlony modification, Dukino builds Equation 2.13, provided below [53].

$$K_{IC} = 0.02595 \left(\frac{a}{l}\right)^{1/2} \left(\frac{E}{H}\right)^{2/3} \frac{P}{c^{3/2}} \qquad \text{(Equation 2.13)}$$

In Equation 2.13, E is Young’s modulus, H is hardness, P is the applied load, l is the crack length, a is the indent diagonal, and c is determined by $c = a + l$. The Ouchterlony modification is included in the calibration constant, which is $k = 0.02595$. Equation 2.13 is used in this thesis to analyze fracture toughness in high temperature indents done with the Berkovich indenter.

Indentation fracture is a very efficient method for studying fracture toughness in brittle materials, but it has not been fully accepted as a reliable method for determining absolute values of fracture toughness. This short-fall is due to the uncertainties in probing a microstructural property and relating it to the macroscopic property. Unlike the other experimental methods for studying fracture toughness, indentation fracture only probes the local microstructure of each indent. The local microstructure may be affected by porosity, grain size, or localized damage. Due to this fact, there is a large spread in the fracture toughness data and it is essential to study several indents to obtain an effective average. Regardless, indentation fracture toughness is a useful method in this present study because the ultimate goal is to make comparisons between different additive types with respect to un-doped control samples, so there is less concern with obtaining an absolute fracture toughness value.

Yield Strength from Indentation

In the first attempt to relate indentation hardness and yield strength, Tabor investigated ductile materials using spherical indentation and found a simple equation, Equation 2.14, relating contact pressure and yield strength [56].

$$P_m = cY \qquad \text{(Equation 2.14)}$$

In Equation 2.14, P_m is the mean contact pressure (hardness), Y is the yield strength, and c is a constant approximately equal to 3 [56]. This equation will work with spherical and blunt-wedge indenters in any rigid, perfectly-plastic material that does not exhibit work-hardening [57]. In materials that deviate from the perfectly-plastic model, modifications must be made to the Tabor equation. In strain-hardening materials which do not show a definite yield stress, a representative stress can be used instead. For a Vickers indent system, the representative stress would be the stress at 8% strain [57]. A paper by Johnson covers other equations for very-elastic material systems where elastic deformation cannot be ignored [57].

Giannakopolous et al. published an in-depth analysis of Vickers indentation that covers another method for determining yield strength [58]. In this report, the authors measure the radius of the pile-up zone around a Vickers indent and use that in calculating the yield strength [58]. Pile-up is a material phenomenon that occurs during indentation of semi-plastic materials. It represents the total area of plastic deformation due to indentation. The plastic zone radius can be measured using optical microscopy or profilometry. In Equation 2.15, established by Giannakopolous, P is the indentation load, c is the radius of the plastic zone, and σ_y is the yield strength [58].

$$c^2 = \frac{0.3P}{\sigma_y} \qquad \text{(Equation 2.15)}$$

Cahoon et al. worked to improve upon the original equations established by Tabor by forming an equation which accounted for strain hardening in the material [59]. This insight allowed for the 0.2% offset yield strength to be calculated from hardness in a wider variety of materials. Cahoon's equation was established through experiments on brass, cold-rolled steel, tempered steel, and a few aluminum alloys, to ensure that it is suitable for a wide range of materials which show varying degrees of plastic deformation and strain-hardening [59].

$$\sigma_y = \left(\frac{H}{3}\right)(0.1)^{(m-2)} \qquad \text{(Equation 2.16)}$$

In Equation 2.16, H is Vickers Hardness and m is Meyer's coefficient, which is material dependent. Meyer's coefficient (m) is related to the material's strain hardening coefficient (n) via $n = m - 2$ [59]. Equation 2.16, established by Cahoon, gives a direct means to calculate yield strength from the indentation hardness if the Meyer’s coefficient is available. Equation 2.15, from Giannakopolous, is a straightforward method to calculate yield strength if plastic zone pile-up occurs [58]. In this thesis, Equation 2.15 is used to calculate yield strength from the high-temperature indents that produce material pile-up.

The equations, methodologies and findings presented in this literature review have been influential in guiding the research contained in this thesis project. Without the great work done over the past several decades, this current project would have been impossible.

CHAPTER 3

OBJECTIVE

The main objective of this research project is to determine which dopants produce UO_2 fuel that is less prone to cracking or fracture at ambient and elevated temperatures. Los Alamos National Laboratory (LANL) fabricated doped-UO_2 samples containing various percentages of the following dopants: aluminum oxide (Al_2O_3), chromium oxide (Cr_2O_3), silicon dioxide (SiO_2), titanium dioxide (TiO_2), and yttrium oxide (Y_2O_3). Un-doped samples were also provided so that the properties of the doped samples can be compared to a baseline reference material. The samples are used throughout this project to gain an understanding of how different dopant types will affect the microstructure and mechanical properties of UO_2.

Hardness, fracture toughness, and yield strength were systematically measured and analyzed to characterize the strength of the material. To probe these mechanical properties with respect to temperature, Vickers indentation experiments were performed at room temperature and at various temperatures ranging from 450 °C to 1200 °C. The indents were analyzed using established methods and empirical formulas for hardness, fracture toughness and yield strength. Several indents at each temperature allowed for a limited statistical analysis of the mechanical properties. Due to the different nature of deformation at different temperatures, fracture toughness was only analyzed at room temperature, and yield strength was only analyzed at elevated temperatures.

Pre- and post-experimental analysis was done at Arizona State University primarily using the TESCAN scanning electron microscope available in Dr. Pedro Peralta's Materials Testing Laboratory. Along with using electron microscopy to measure indents and cracking for calculating mechanical properties, each sample microstructure was quantitatively analyzed for grain size using either orientation image mapping (OIM) or the ASTM linear intercept method. With OIM, the grain size distribution data was analyzed to look for bi-modal grain growth. Each sample's microstructure was compared with the microstructure of an un-doped sample processed under similar conditions to determine how the additives affected grain growth and grain size distribution.

To qualify the effects of the dopants on the different mechanical properties, each one was "graded" on how it affected each property in comparison to the un-doped sample. A positive grade implies that the dopant improved the selected material property, and a negative grade indicates that the dopant diminished the material property. The objective of this research was to find dopants that increased fracture toughness and decreased hardness at room temperature. At elevated temperatures, the optimal dopant would a decrease in yield strength, indicative of improved ductility, in comparison to the un-doped sample.

In this sense, the ideal doped material would be less prone to cracking at room temperature, and would show a higher degree of ductility at elevated temperature. Using the "grading system," each additive can be objectively compared, even across fabrication batches, and the best choice for improving the mechanical properties can be determined.

CHAPTER 4

EXPERIMENTAL PROCEDURES

Sample Fabrication

The samples used in this study were fabricated at Los Alamos National Laboratory. Cylindrical pellets were compacted from Areva® depleted-UO_2 powder mixed with the desired concentration of dopants. Samples were produced in separate batches using different processing methods, but the general methodology is given below. A majority of the samples were produced using a “dry” powder compaction procedure. Here, the UO_2 powder precursor is first mixed with ethanol and sonicated to mix and break up any agglomerates. The appropriate concentration of additive precursor is then added to this mixture. Each additive is introduced using a different precursor chemical. For example, to dope with Al_2O_3, aluminum isoperoxide is added. For SiO_2, tetraethylorthosilicate is introduced, and chromium acetylacetonate is used in Cr_2O_3-doping. The uranium oxide powder and additive precursor are then spex-milled for 15 minutes to further break down and mix the powders. The final powder is pressed into pellets under 75 MPa pressure on a uniaxial press. The resulting “green” pellets are sintered at 1600 °C for four hours in inert gas containing ~150 ppm H_2 mixed with ultra-high purity argon to achieve a stoichiometric sample. An in-depth report of this procedure has been produced by Leckie and Luther and is available through LANL [60].

The samples fabricated using a “wet” processing routine followed a similar procedure, but added ethylene bistearamide to act as a binder in the mixed powder prior to sintering.

After the samples were sintered, each sample was characterized to determine its diameter, height, weight and density. This information can be found in Table 4.1 below. Samples were then shipped to Arizona State University for further characterization and mechanical testing.

Table 4.1: Physical characteristics of samples used in this study.

Sample #	Additive Type	Height (mm)	Diameter (mm)	Density (g/cm^3)	% Theoretical Density (%TD)
32	0.1 wt% TiO_2	1.9	5.7	10.41	94.95
33	0.2 wt% TiO_2	1.9	5.7	10.41	94.97
34	0.05 wt% Y_2O_3	1.9	5.8	10.63	97.01
35	0.1 wt% Y_2O_3	1.9	5.8	10.64	97.10
38	None	2.0	5.7	10.72	97.78
39	None	2.0	5.7	10.58	96.55
129	None	1.8	5.8	10.28	93.81
130	None	N/A	N/A	10.31	94.07
371	0.2 wt% Cr_2O_3	2.6	5.5	10.63	97.02
372	0.2 wt% Al_2O_3	2.7	5.5	10.39	94.84
373	0.2 wt% SiO_2	2.7	5.4	10.53	96.11
374	None	2.7	5.5	10.58	96.50

Sample Polishing

Prior to any preliminary characterization, the samples must be polished to a planar, mirror finish. To stop any unwanted dispersion of radioactive material and to prevent any radioactive contamination from occurring, sample polishing was done manually in an inert environment glove-box or in our automated polishing containment enclosure, both shown below. At every step, special care was taken to identify and clean potentially contaminated surfaces, minimize contact with the samples, and account for any loss of material.

Figure 4.1: Left- Inert environment glove-box for radioactive grinding and cutting. Right- Polishing containment enclosure where a majority of the polishing was done.

The polishing procedure was highly dependent on the quality of the sample, with some samples needing additional grinding/polishing steps in the early stages and others just needing the final polishing steps. In Table 4.2 below, a general polishing procedure is listed that covers the full extent of the polishing steps. Grinding was only needed to flatten the sample or remove a layer of epoxy, if necessary. Grinding was not necessary for most of the samples. Polishing was done using a Buehler Minimet® polisher. Using the procedure listed in Table 4.2 with the Minimet® in the polishing enclosure would consistently produce OIM-quality surfaces with minimal damage or grain pull-out.

Table 4.2: General sample polishing procedure

Step	Abrasive	Polishing Pad	Load	RPM	Time (mins)
Grinding	600 grit SiC	Wet SiC paper	None	15	3
Grinding	800 grit SiC	Wet SiC paper	None	15	5
Grinding	1200 grit SiC	Wet SiC paper	None	15	5
Polishing	3 µm diamond suspension	CerMesh®	None	20	5
Polishing	3 µm diamond suspension	CerMesh®	5 N	20	10
Polishing	1 µm diamond suspension	TexPan®	5 N	25	5
Polishing	0.25 µm dia. susp./Siamat®	TexPan®	5 N	25	10
Polishing	Siamat®	BlackChem 2®	5 N	30	20
Polishing	Siamat 2®	BlackChem 2®	5 N	30	40

When working in the polishing containment enclosure, it was very important to prepare a workstation that allowed one to clean each polishing tray quickly between steps. Most importantly, one had to ensure that the polishing tray stays wet during the entire process to prevent any uranium oxide particles removed during polishing from becoming airborne. It is also important that one paid attention to the polishing pad used during each step. The pads will occasionally come loose from the glass backing, and they also may tear if they are used too long or with too high of a load. Since the Buehler

Minimet® is automated it will continue to run even if the polishing pad is damaged, this can result in severe damage to the sample surface. If the polishing pad comes loose, it is likely due to using too much water during that step. In this situation, replace the polishing pad and repeat the given step using less water and solution.

To use diamond polishing solutions when polishing uranium oxide, it was necessary to use water-based suspensions to avoid producing mixed radioactive waste. Colloidal silica is water-based, so this was not an issue. It is important though to thoroughly clean off colloidal silica between each polishing step. The silica suspension will quickly dry and crystallize, forming residue that will scratch the sample surface.

As always when working with radioactive material, it is extremely important to manage and properly dispose of any contaminated waste. Each polishing step will use a significant amount of liquid (water, colloidal silica, or diamond suspension) and this must be soaked up into green absorbent pads and disposed of. Any tools or items that come in contact with contaminated surfaces must be thoroughly cleaned and scanned with the radiation detector to ensure that they are not contaminated. Since cleaning must be done after each polishing step, it is necessary to either scan your gloves with the radiation detector, or simply dispose of them and replace them. A full procedure for polishing radioactive materials in the polishing enclosure is included in Appendix A at the end of this thesis.

Preliminary Characterization

After polishing the samples, preliminary characterization was done in order to obtain information on the initial microstructure, the chemical composition, and any flaws or damage on the sample surfaces. Each sample was examined in the optical microscope to gain an understanding of the general quality of the sample surfaces and to capture a low-magnification image of the samples. From this, it was determined if any sample needed further polishing, and it was also helpful in locating sites to perform microhardness measurements. Extensive preliminary characterization was done using scanning electron microscopy (SEM) on a Tescan Vega II scanning electron microscope. It was important to note any surface cracks or localized pore clusters because these defects will cause local changes in the physical-mechanical properties of the sample and these areas must be avoided during experiments. The majority of the defects were either ring-cracking or surface delamination, which are both undesired consequences of the uniaxial pressing process used to fabricate the samples. Pore clusters are typically a result of out-gassing when the organic binder material is burned away during sintering.

Further preliminary characterization included measuring the average grain size and looking for any grain texture using orientation image mapping (OIM). This is a technique that utilizes electron backscattering diffraction (EBSD) patterns produced in the SEM. By positioning the sample at a 70° vertical tilt underneath the SEM beam column, and using an EBSD detector situated perpendicular to the beam, OIM mapping allows the user to create a grain orientation map of a sample surface [61]. An example of an OIM map is given below. The different colors of each grain correspond to distinct grain orientations with respect to the reference direction (typically the out-of-plane axis) [61]. The colors are dictated by the inverse pole figure (IPF) legend shown to the right of the OIM map. When using IPF with EBSD maps, it is necessary to always cite the reference direction.

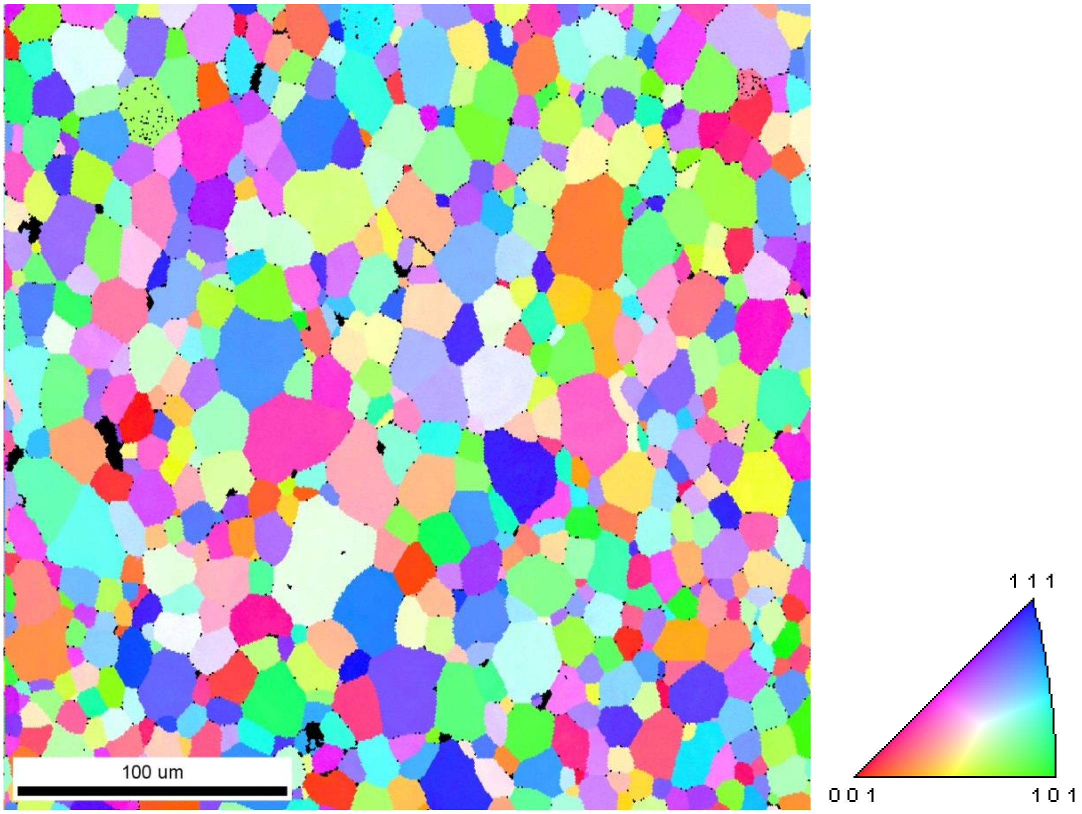

Figure 4.2: OIM of pure UO_2 sample (#374). Grain coloration corresponds to the standard IPF shown to the right.

Mapping from OIM is a very useful tool for analyzing a material's microstructure. It highlights any trends in grain orientation, grain size, and grain boundary misorientation. It can quantify the grain size distribution and can be used to look for correlations between grain growth and grain boundary misorientations. It is also useful in identifying how pores are dispersed throughout the microstructure.

In several samples, grain size was also measured using the ASTM E112-13 linear intercept method on images taken in the scanning electron microscope [62]. In this procedure, 15-20 lines were drawn across each sample surface in random directions. These lines were measured, and the number of grain boundaries that each line intercepted was counted. If the line stopped in the middle of the grain, that was counted as ½ rather than 1. By dividing the line length by the number of intercepts, the average grain diameter was calculated.

The linear intercept method does not provide any indication of the grain size distribution in the sample. Thus using OIM for grain size measurements is a much more powerful tool, as it measures the size of each grain and produces a statistical report of the grain size. This is an essential tool for samples with a heterogeneous or bi-modal distribution of grain sizes. Figure 4.3 shows the grain size distribution chart for the UO_2-0.2 wt% Cr_2O_3 doped sample. The samples in this work all exhibit similar grain size distributions and do not show any signs of bi-modal grain growth.

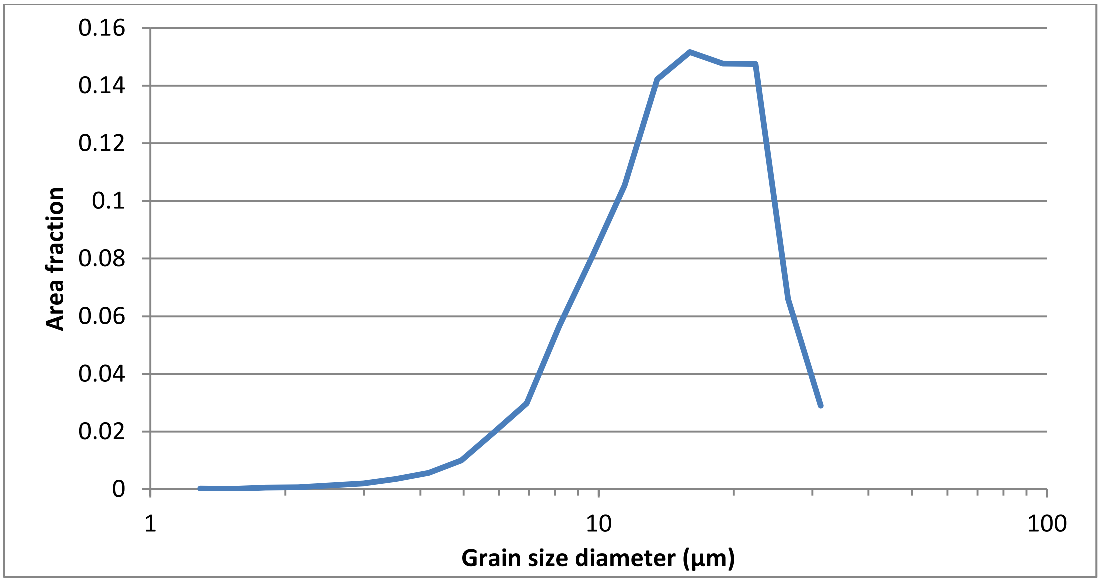

Figure 4.3: Grain size distribution for 0.2 wt% Cr_2O_3-doped Sample 372. Average diameter = 9.7 µm with 5.8 µm standard deviation.

The final step of preliminary characterization was to examine the chemistry of the samples. Chemical analysis of the samples was done using energy dispersive spectroscopy (EDS) on the JEOL JXA-8530F electron microprobe available for use in the John M. Cowley Center for High Resolution Electron Microscopy at Arizona State University. The technique was used to understand how the additive was dispersed throughout the crystalline matrix of uranium oxide. The dopant distribution was found to be unique for each dopant type. Using EDS also provided a quantitative estimate of the actual concentration of each dopant in the sample. This was vital, since prior research has shown that only a fraction of the dopant added initially will be retained in the sample after sintering [17].

Vickers Indentation

Room temperature Vickers indents were done on a Leco M-400-H2 Microindentation Hardness Tester. Vickers indentation testing is a popular experimental method for non-destructive evaluation and characterization of basic mechanical properties of a material. Since only a small volume of material is probed during each experiment, several indents can be made on a single sample. Another advantage of Vickers indentation is the relative simplicity of the testing procedure and the indentation analysis.

In a Vickers indentation test, a four-sided pyramidal diamond is driven into the material of interest until a predetermined load is reached. The load is held constant for 10-15 seconds before the load is released and the indenter is removed. The indenter will leave an impression on the material surface which can be measured directly for hardness readings and can be analyzed further for information on yield strength and fracture toughness. Because these tests yield a good amount of information, can be performed and repeated quickly, and are quasi-non-destructive, Vickers indentation is a convenient method for probing materials to understand their mechanical properties. Each indent was done with one kgf load and measurements were taken either directly at the micro-indenter instrument or using SEM.

High-Temperature Indentation

In order to probe the samples at elevated temperatures, it was necessary to design and build a high-temperature indentation assembly. The assembly consisted of a load frame to apply the load, a furnace to reach the desired temperatures, and an enclosure to prevent oxidation during testing. The end-caps of the enclosure were water-cooled to prevent over-heating of the load cell and load frame actuator, and gettered ultra-high purity argon gas was used as the inert environment. This assembly was incrementally updated and improved over the course of the experiments. For the high temperature indents, each indent was done with approximately 1 kgf load, and the hardness calculation was done using the peak load recorded for each indent

Initially a ThermoScientific F21135 tube furnace, with a maximum temperature limit of 1200°C, was used in the assembly. This is shown in the left image of Figure 4.4 Roughly half-way through the high temperature experiments, the ThermoScientific furnace was replaced with an Instron split-tube furnace, with a maximum temperature of only 1000 °C. This is shown in the right image of Figure 4.4. Indentation experiments were done at temperatures from 450 °C to 1200 °C, typically doing indents at three to five different temperatures per experiment. The assembly has a translation stage to allow for several indents in a single experimental run. Four or five indents were done at each temperature. In a single experimental run with multiple temperatures, the highest temperature indents were always done first and the furnace temperature would be progressively lowered to each subsequent temperature. This was done to prevent any crack-closure or recrystallization around the indents that may occur if the temperature was increased rather than decreased as indents were made.

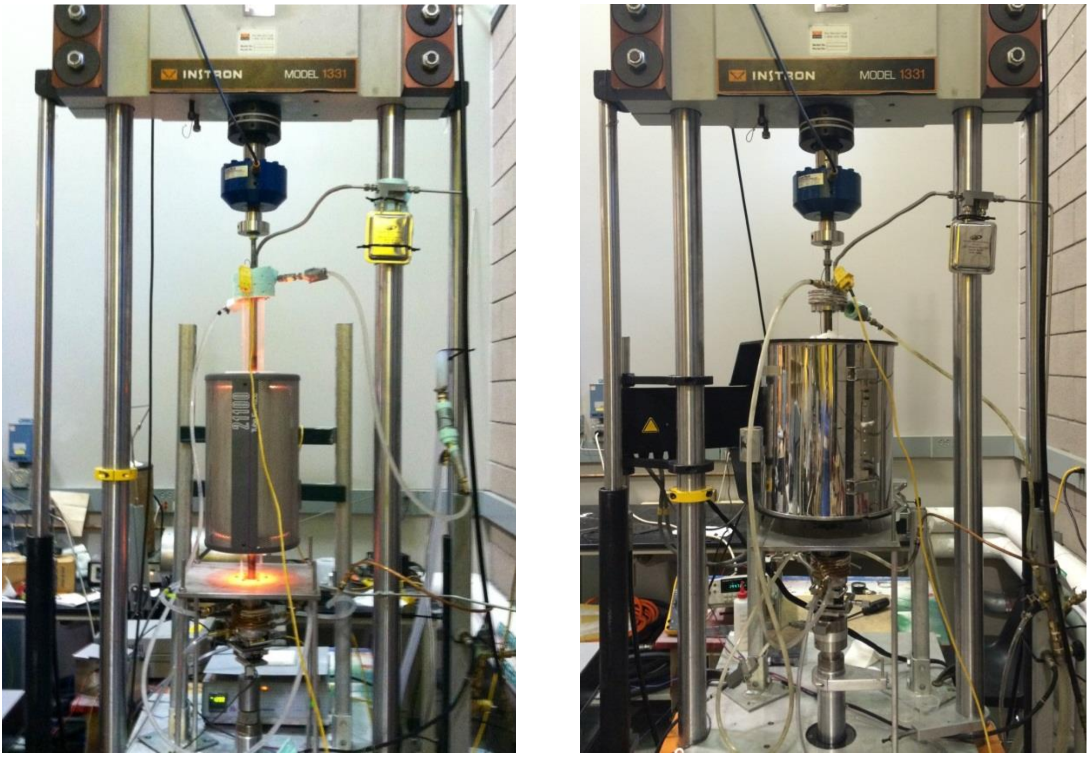

Figure 4.4: Left- High temperature indentation assembly with ThermoScientific tube furnace. Right- Assembly with Instron split-tube furnace.

To protect the indenter and sample from rapid oxidation at high temperatures, the indentation rods were secured inside a quartz tube enclosure that fits inside the furnace and is flushed with ultra-high purity argon gas. The argon gas was passed through an oxygen getter to reduce the partial pressure of oxygen to below 10^{-15} atm. During the experiments, the oxygen partial pressure was continually monitored using oxygen sensors at both the inlet and outlet of the quartz enclosure. It was essential to keep the oxygen partial pressure below 10^{-15} atm for the duration of the experiment. If the oxygen partial pressure was above this level, the UO_2 would begin oxidizing. Figure 4.5 shows the U-O phase diagram with isobars for oxygen partial pressure, and it is clear that the system must be as oxygen-free as possible. Therefore to maintain a constant, uniform atmosphere for each experimental run, inert gas was slowly passed through the assembly for the duration of the experiment.

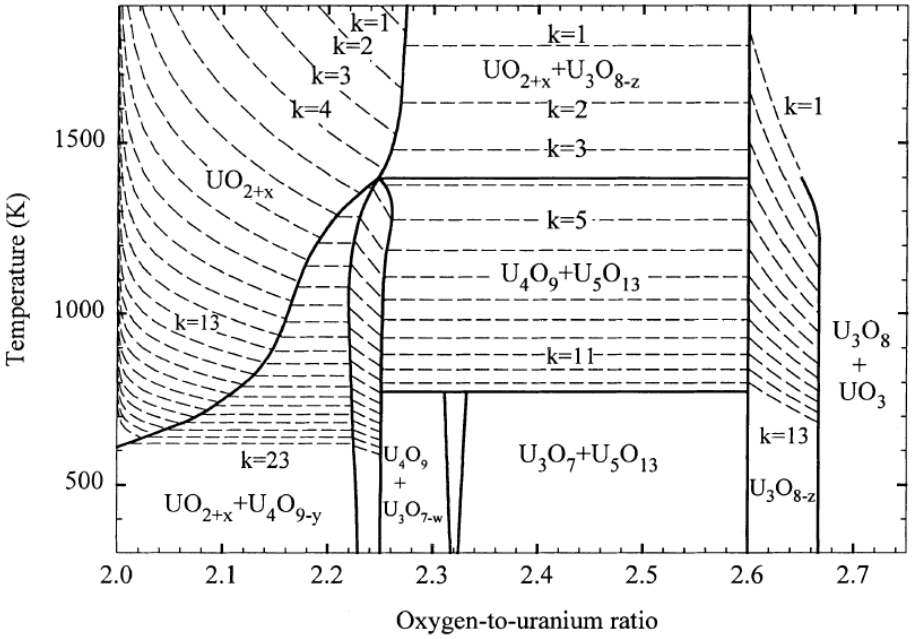

Figure 4.5: Phase diagram of U-O system with oxygen pressure isobars. The *k* term refers to p (atm) = 10^{-k} [18].

In the assembly, the sample rod and indenter rod were machined from a titanium-zirconium-molybdenum (TZM) refractory alloy. The indenter rod had a threaded end that allowed the experimenter to attach a variety of different indenters, granted that the threaded ends matched correctly.

Several issues arose during the high temperature indentation experiments. Even with an oxygen-gettered UHP argon environment, the diamond indenters deteriorated during the experiments. This often resulted in poor-quality indents towards the end of each experiment, occasionally producing indents that could not even be properly analyzed. It was discovered that the indenter was reacting with the sample during each indent and would bond with the material and pull UO_2 from the surface. The excess UO_2 on the indenter surface would cause each subsequent indent to be lower in quality.

In the work by Wheeler [63] different indenter materials were studied and it was shown that 6H-SiC is less chemically reactive in contact with oxide materials, and was less prone to degradation at high temperatures in an oxygen environment. Hence, the chemical interaction problem encountered in this work was solved by switching the indenter material from diamond to 6H-SiC. A company called Synton-MDP in Zurich, Switzerland manufactured a custom SiC indenter for this project.

Another persistent problem in the high temperature experiments was caused by lateral misalignment between the sample and the indenter. When setting up the assembly, it was necessary to align the sample under the indenter and establish the grid pattern for the indents prior to putting on the quartz tube and furnace. Yet it was likely that the sample rod would be bumped or shifted while putting these pieces on the assembly, thus leading to lateral misalignment. To improve on this issue, an Instron split-tube furnace was refurbished and used to replace the original ThermoScientific tube furnace. Using a split-tube furnace that can be opened and closed around the quartz tube greatly simplified the assembly process. In particular, sample alignment could be done after the quartz tube was in place, and the furnace could then be closed around the tube. This significantly reduced the likelihood of any sample misalignment and this was found to be the case after the upgrade.

An example image of a room temperature indent done on the Leco Microindenter machine is given on the left in Figure 4.6. An image showing a typical “indent grid” from a high temperature indent experiment is provided on the right in Figure 4.6.

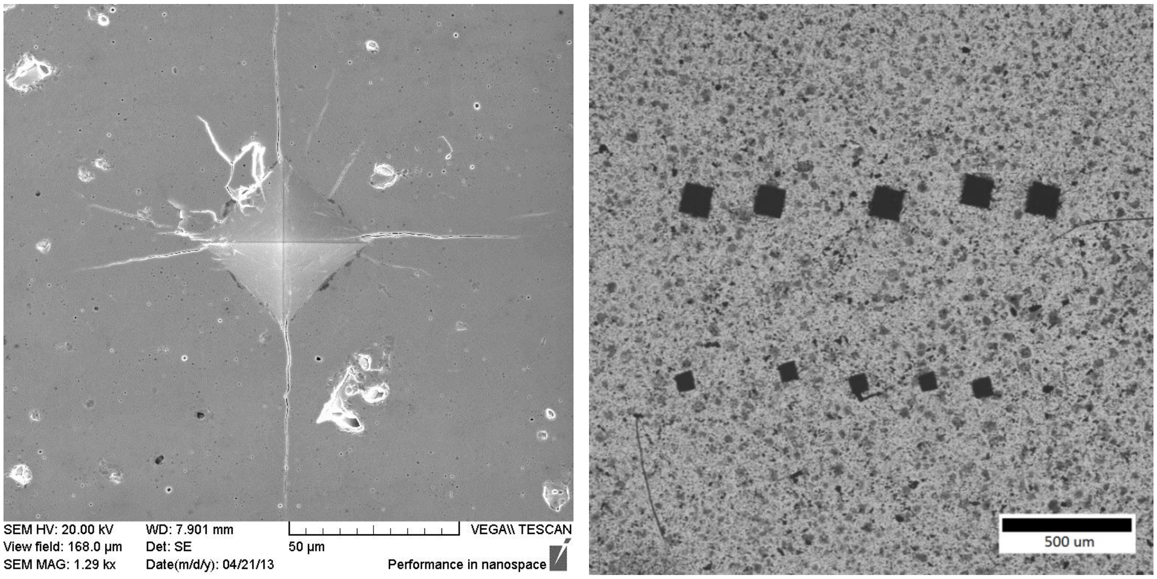

Figure 4.6: Left- Room temperature Vickers indent. Right- Vickers indent grid, top row done at 1200 °C, bottom row done at 500 °C.

Indentation is the primary experimental method used in this thesis to analyze the mechanical properties of the doped-UO2 samples. By analyzing the room temperature and high temperature indents, several different mechanical properties can be obtained. The following chapter describes the analytical procedures used to extract hardness, Young’s modulus, fracture toughness and yield strength values from these experiments. In conjunction with EBSD and EDS data, this information can be used to establish conclusions into how the dopants interact with and effect the properties of uranium oxide.

CHAPTER 5

ANALYTICAL PROCEDURES

Vickers Hardness

Hardness describes a material's resistance to plastic deformation. It is not an intrinsic material property, as yield strength or fracture toughness, because its value is dependent on the hardness system that is used in taking the measurement. Nevertheless, hardness is a very convenient, useful metric for making comparisons between materials, which is one of the objectives of this work. Because hardness is influenced by several material properties, such as the yield strength and fracture toughness, seeing a change in the hardness is indicative of a change in at least one of these intrinsic properties. Vickers hardness is calculated using Equation 5.1 [64].

$$HV\ (MPa) = 9.80665 * 1.8544 * (P/d^2) \qquad \text{(Equation 5.1)}$$

Vickers indents in this study were done with a load (P) of 1kgf held for ten seconds. The indent diagonal (d) is the average of the two diagonals in mm. The hardness was calculated by taking the mean average of the indents done at a single temperature. In Equation 5.1, the constant, *1.8544*, is a proportionality term to convert the projected contact area into the true contact area. The other constant, *9.80665*, converts the hardness from kgf/mm^2 to MPa [65].

Berkovich Hardness

Berkovich indenters are the most widely used indenters in nanoindentation. The Berkovich indenter is a three-sided pyramid; this was chosen for nanoindentation because it is much easier to fabricate a sharp tip with this geometry than it is with the four-sided Vickers pyramid. A precisely sharp tip is extremely important in nanoindentation, but it is not crucial to microindentation. The Berkovich indenter was developed to have the same area-to-depth characteristics as the Vickers indenter [66].

Berkovich indentation differs from Vickers in the way that each indent is typically analyzed. In a majority of Berkovich systems, the load, displacement and strain of the indentation system are continually measured and recorded, and the maximum depth of the indenter is used in calculating the area of the indent at peak load. Peak load and the area at maximum depth are then used to determine the Berkovich hardness (HB) of the material. Measuring the residual area (projected indent area after experimentation), assuming an ideal equilateral triangle imprint, can result in a meaningful error (4-5%) in the hardness measurement [66]. To calculate the indent area at peak load, Equation 5.2 is used [67].

$$A = 3\sqrt{3}h^2 tan^2\theta = 24.494h^2 \qquad \text{(Equation 5.2)}$$

In Equation 5.2, the maximum depth (h) is used to determine the contact area (A) of the indenter. To calculate HB, the max load (P_{max}) is divided by the contact area [68].

In the indentation system used for this thesis, the load cell did not have a high enough precision to detect the initial contact between the sample surface and the indenter, thus there was a very large error associated with measuring the maximum depth. For this reason, careful measurements of the residual area had to be used to determine the HB value. To reduce the error in using the residual area, it was necessary to account for the material pile-up around the indents. Material pile-up causes the shape of the indent to deviate from that of a standard triangle and instead resemble a triangle with bowed-out edges [66]. This is shown in the left image of Figure 5.1 below, where the yellow overlaid lines represent a triangle with straight edges emanating from the corners.

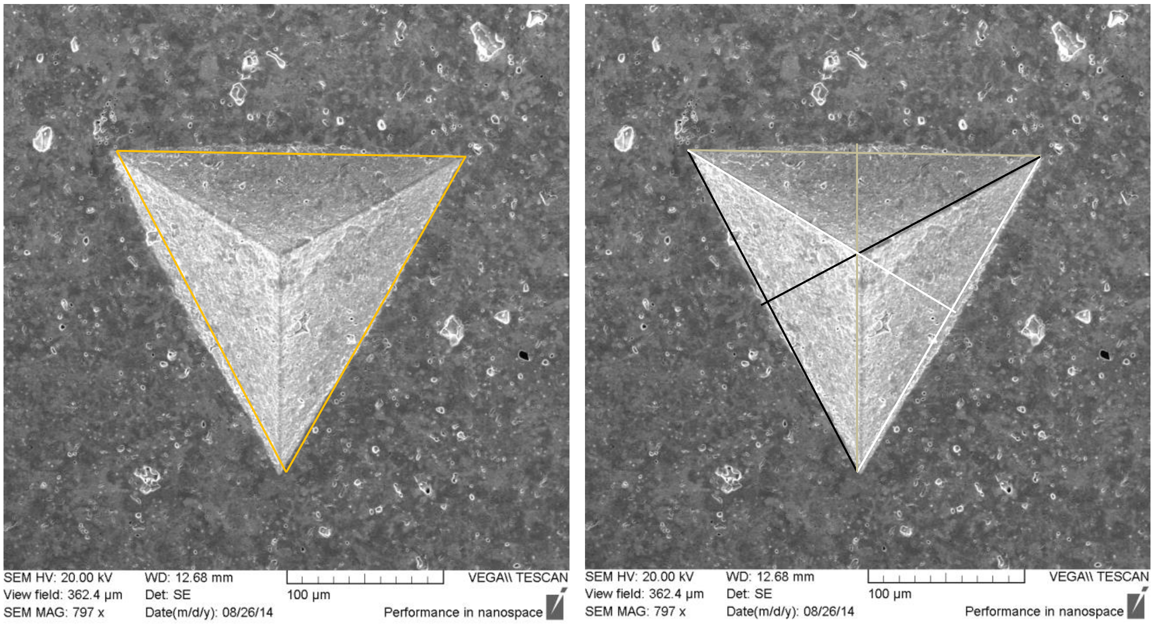

Figure 5.1: Left- Example of pile-up around a Berkovich indent. Yellow overlaid triangle represents indent with no pile-up. Right- Procedure to determine the average area. Notice the three unique color combinations used to find the average area.

To get an accurate value of the residual area of each indent, three triangular areas were calculated independently and then averaged. Using the standard equation for a triangular area, $A = \frac{1}{2} b * h$, the area was calculated using each unique set of base and height and measurements. Figure 5.1 above shows the methodology for these measurements. Area was calculated from each base-height color combinations and averaged. The height measurement accounts for any excess contact area due to bowing, and the average of these values results in hardness values consistent with what was found using Vickers indentation.

Fracture Toughness

Fracture toughness can be calculated when indentation causes cracking from the indent corners. In this thesis, fracture toughness analysis was performed on every sample at room temperature. The most accurate equation for calculating K_{IC} fracture toughness from Vickers indents was found to be one derived by Niihara et al. [49]. In the equation below, $\emptyset$ is a constraint factor ($\simeq$ 3), E is the Young's modulus (in MPa), H is the Vickers hardness (in MPa), a is the half-diagonal of the Vickers indent (in mm), and l is the length of the surface crack (in mm) from indent corner to crack tip.

$$K_{IC} = \frac{0.035}{\emptyset} H\sqrt{a} \left(\frac{H}{\emptyset E}\right)^{-0.4} \left(\frac{l}{a}\right)^{-0.5} \qquad \text{(Equation 5.3)}$$

To accurately report the fracture toughness for each sample, the value was averaged from several individual indents done under the same conditions. With room temperature indentation, typically ten indents were done on each sample, and at elevated temperatures, four or five indents were done. For each indent, the average crack length and half-diagonal length with the corresponding hardness would be used in the fracture toughness calculation. Young's modulus differs between samples, as it changes with respect to density [20].

To calculate fracture toughness from Berkovich indents, a separate equation must be used, as the mechanics of cracking differ from the Vickers indent. The methodology for analyzing fracture toughness from Berkovich indents does not differ from Vickers indents, and the equation established by Dukino [53] has been shown to yield a fracture toughness very similar to what is found from Vickers indents. The equation used in this thesis to determine fracture toughness from Berkovich indents is taken from a paper by Dukino [53] and utilizes a modification established by Ouchterlony [55]. The final form of the equation is shown in Equation 5.4.

$$K_{IC} = 0.02595 \left(\frac{a}{l}\right)^{1/2} \left(\frac{E}{H}\right)^{2/3} \frac{P}{c^{3/2}} \qquad \text{(Equation 5.4)}$$

In Equation 5.4, the terms *a*, *c*, and *l* refer to geometric constants described in Figure 5.2 below.

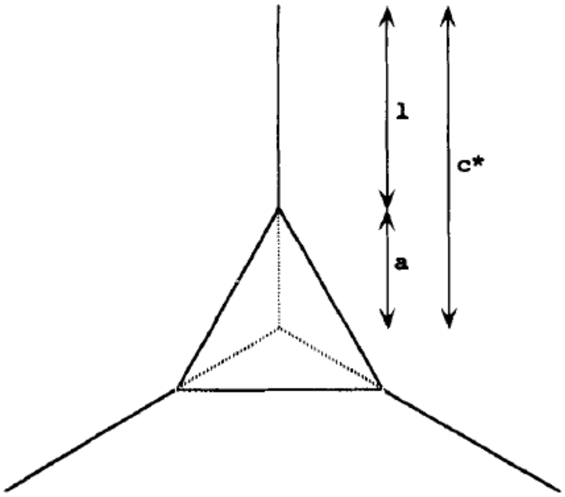

Figure 5.2: Measurements used in fracture toughness analysis of a Berkovich indent [53].

Yield Strength

In indents done at 500°C and above, material pile-up often occurs around the outer edge of the indent. The extent of the pile-up region can be measured to obtain quantitative properties such as the yield strength [58, 66]. A Zygo ZeScope optical profilometer is used to measure the height and average radius of the pile-up region. The ZeScope optical profilometer uses optical interference to make surface topographs at 3x, 5x, or 10x magnifications. These maps have sub-micron spatial resolution. This is a great tool for capturing the extent of material pile-up around a high temperature indent. The yield strength of a material is calculated using Equation 5.5 [58]. Equation 5.5 has been show to work for both Vickers and Berkovich indents [58, 66].

$$\sigma_y = \frac{P}{\pi r_P^2} \qquad \text{(Equation 5.5)}$$

Using the analytical tools presented in this chapter, it is possible to gain a strong understanding of the mechanical performance of the doped and pure UO_2 samples used in this research. By accounting for hardness, fracture toughness and yield strength at both high and low temperatures, this research is able to characterize the mechanical qualities of each sample and make comparisons between the different dopant species. With the quantitative and qualitative information gathered using these tools, it is possible to conclusively determine the best dopant for improving the mechanical performance in UO_2.

CHAPTER 6

RESULTS AND DISCUSSION

This chapter covers the experimental data collected over the course of this research. It is important to note that the samples were produced in separate batches with different fabrication methods. Therefore, direct comparisons can only be made between samples from a particular batch. Each batch came with an un-doped sample, so that the different additives can all be individually compared to a pure UO_2 specimen fabricated using the same methods. Of the three different batches, Batch 1 and Batch 2 were fabricated most similarly, and the results show that the samples are comparable on some levels.

Each dopant type is covered independently in its own sub-section, where the measured properties are quantitatively compared to that of the corresponding un-doped sample. A rating system is applied to determine whether or not the dopant had a positive, negative or neutral effect on a specific property. After establishing the results for each individual dopant type, an over-arching discussion section will compare these results. While direct comparisons can only be made between samples from the same batch, it is possible to make relative comparisons among samples using the rating system.

Prior to presenting the experimental results of this research, it is important to highlight and discuss the experimental difficulties and some uncertainties that arose during the research that may affect the results.

Experimental Difficulties

As it was mentioned in the experimental procedures chapter, there were some difficulties that had to be overcome during the high temperature Vickers indentation experiments. The primary issue that had to be dealt with was indenter degradation. During each high temperature indent, uranium oxide would gradually stick to the surface of the diamond indenter. This was likely caused by a high temperature reaction between the uranium and carbon forming a uranium carbide compound. With each indent, this layer of material on the surface would continue to build up and would degrade the quality of each subsequent indent. Ultimately, this would lead to unreliable indents, which could not be used for extracting mechanical property data. To overcome this, it was necessary to switch indenter types. A 6H-SiC Berkovich indenter was substituted for the diamond Vickers indenter.

Another difficulty that affected the experimental results was the lateral misalignment between the indenter and the sample. Before each experiment, the indenter was lined up over the center of the sample. This was to ensure that the indenter probed the “bulk” of the sample, so that the hardness and other properties were not influenced by any edge effects. For the experiments that used the original tube furnace, the alignment had to be done prior to putting the furnace on to the assembly. Sometimes, during the rest of the assembly process, the sample would get shifted and misaligned. This led to some indents hitting near the edge of the sample. These indents would often result in a lower hardness and yield strength. Some of these indents would be greatly distorted, as the sample could easily deform on the side closest to the edge. The indents that showed a high-level of distortion were removed from the dataset. Indents somewhat close to the edge were kept in the dataset, but often showed a slightly lower hardness than other indents done in the bulk of the sample. To remove this issue from the experiment, the original tube furnace was replaced with a split-tube furnace that made assembly much simpler and reduced the possibility of accidental misalignment substantially.

Even with these experimental difficulties, this research produced a large body of data covering several different sample types and mechanical properties over a wide range of temperatures. Through indentation experiments, this work was able to extract three distinct mechanical properties that are used to describe the overall strength of the material. Before discussing the effects of the dopants, the mechanical properties of the pure UO_2 samples must be established, as discussed next.

Pure UO_2 Samples

The pure UO_2 samples are very important, since these samples provide the base-line values to evaluate the mechanical properties of doped-UO_2. There were five un-doped samples in this study. Samples 38 and 39 came with Batch 1, samples 129 and 130 came with Batch 2, and sample 374 came with Batch 3. The density, percentage of theoretical density (%TD), average grain diameter, and Young's modulus of each un-doped sample is provided in Table 6.1 below. Density is known to affect the Young's modulus, so in this thesis, the equation established by Igata and Domoto is used to adjust the Young's modulus accordingly [20].

Table 6.1: Density, grain diameter and Young's modulus of un-doped samples.

Fabrication Batch	Un-doped Samples	Density (g/cm^3)	% TD	Avg. grain diameter (μm)	Young's modulus (GPa)
1	Sample 38	10.72	97.78	11.1	205
1	Sample 39	10.58	96.55	N/A	198
2	Sample 129	10.28	93.81	N/A	182
2	Sample 130	10.31	94.07	6.3	184
3	Sample 374	10.58	96.50	12.9	198

As part of preliminary characterization, IPF maps of a majority of the un-doped samples were created using EBSD. Mapping the microstructure reveals any irregularities in pore distribution, grain size, and grain texture. As expected, the un-doped samples did not show any preferential texture and pore were found to preferentially exist at grain boundaries and triple junctions.

Figure 6.1 contains two examples of IPF maps of the un-doped samples. These maps were taken from Sample 38 and Sample 374. Some very small "grains" can be seen near the center of the IPF map of Sample 38 in Figure 6.1. These are artifacts of a Vickers indent and they do not represent actual grains in the sample. From OIM scans, artifacts such as these are systematically partitioned out of any quantitative analysis that is done on the scan data, including determining the average grain size. An example of partitioning can be seen in Sample 374 in Figure 6.1. The scattered black spots on the microstructure are areas where low-quality data was removed.

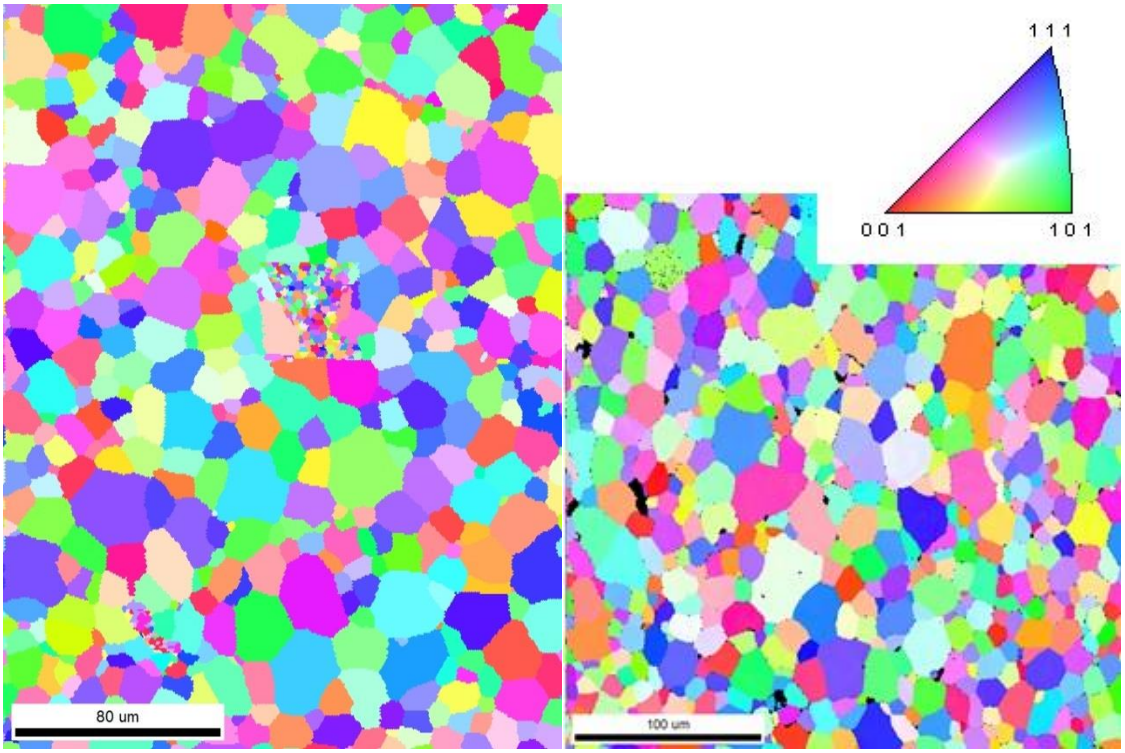

Figure 6.1: IPF map of Sample 38 (left) and Sample 374 (right). The colors correspond to grain orientations parallel to the out of plane direction and are given by the standard IPF triangle legend (shown top right).

Hardness

Each un-doped sample was hardness tested at room temperature and at various elevated temperatures. The average hardness at room temperature for each un-doped sample is shown in Figure 6.2. Room temperature hardness for Sample 130 was never determined; this sample was used in another research project and subsequently destroyed.

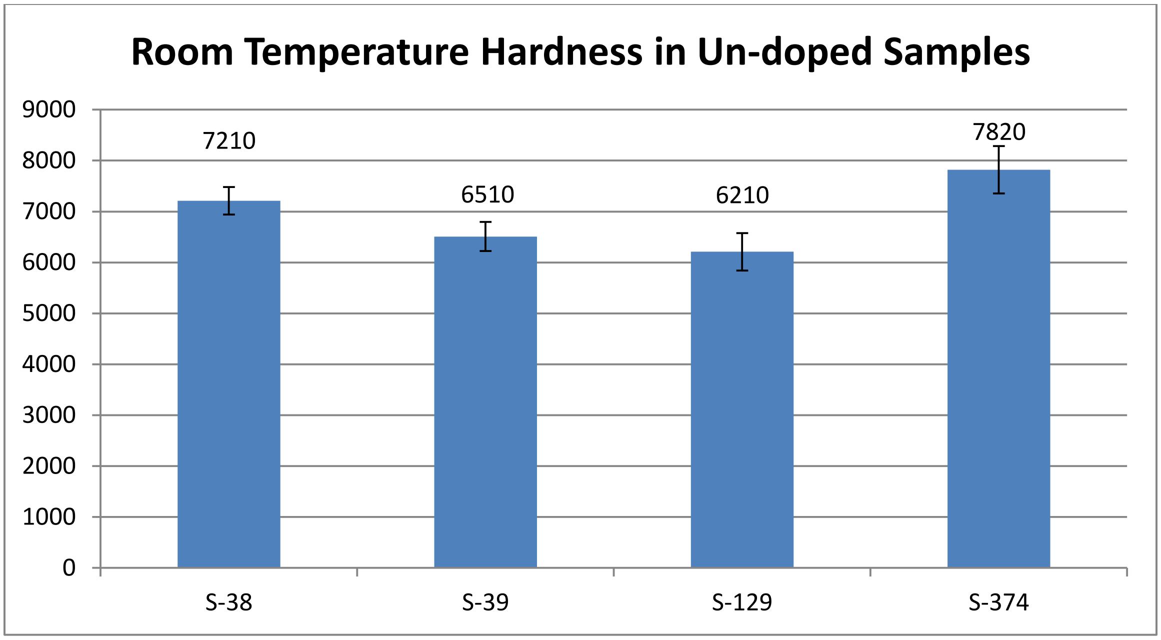

Figure 6.2: Vickers hardness for the un-doped UO_2 samples used in this research.

Samples 38 and 39, fabricated using identical methods, show a significant difference in hardness. The average hardness of Sample 38 was 7210 ± 270 MPa. The average hardness of Sample 39 was 6510 ± 290 MPa. The difference in hardness can likely be attributed to the difference in density between the samples. Recall from Table 6.1 that Sample 38 had a density of 10.72 g/cm^3 and Sample 39 had a density of 10.58 g/cm^3. Yet Sample 374 has a density similar to that of Sample 39, but shows a significantly higher average hardness. The average hardness of Sample 374 was 7820 ± 470 MPa. This increase in hardness is likely due to the differences in fabrication. Samples from Batch 3, such as Sample 374 were made using "wet" processing that included an organic binder material. This led to stronger, less fragile samples than Batch 1 and 2, which were fabricated using a "dry" processing route. Using the fabrication process as the basis for comparisons, samples made in Batch 1 and 2 can be compared, but samples made in Batch 3 are standalone in this respect.

The average hardness at room temperature typically shows a much larger deviation than the average hardness in the same samples at elevated temperatures. At room temperature, the samples are very brittle, and local changes in the microstructure around indents, such as a nearby cluster of pores or a region with smaller grains, have a pronounced effect on the hardness. As the sample temperature increases, it begins to exhibit more ductility and can better accommodate strain via plastic deformation, and thus the near-field effects of the microstructure are less pronounced.

The plot in Figure 6.3 below shows the hardness for the un-doped samples across a temperature range of 450 °C to 1160 °C. The errors bars in Figure 6.3 represent the average deviation for hardness at each temperature. The large drop in hardness seen in the temperature range of 450 to 550 °C suggests that the sample goes through its brittle-to-ductile transition (BDT) temperature. This is supported by other experimental results, since indents done at 450 °C always produce long cracks, indicative of brittle fracture, whereas indents done at 500 °C and 550 °C show far less cracking and significant plastic zone pile-up, indicative of plastic deformation.

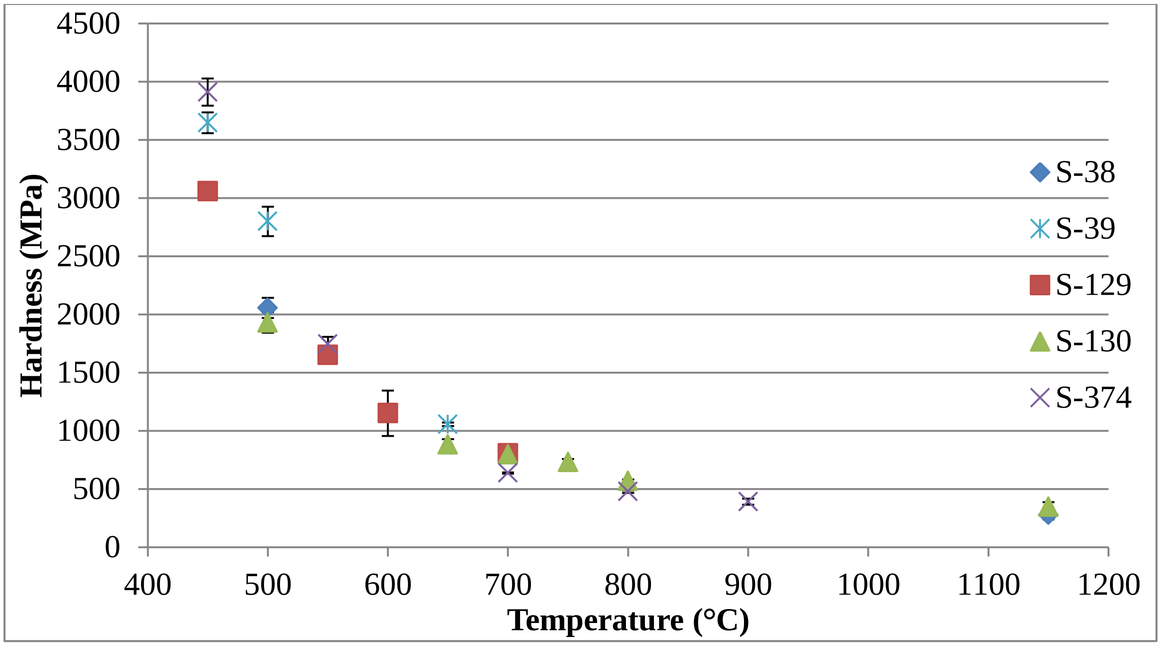

Figure 6.3: Average hardness of each un-doped sample with respect to temperature.

This finding differs from previous published results. In papers by Tottle [69] and Evans and Davidge [13], the BDT temperature is found to exist at a much higher temperature, in the range of 1200-1300 °C. The difference can be explained by understanding the experimental methods used. Tottle and Evans and Davidge used three-point bending to study the mechanical properties of UO_2 at high temperatures [13, 69]. The present work uses indentation. These experimental methods produce a largely different state of stress in the material. Three-point bending specimens will experience both tension and compression, with the tension component leading to an emphasis on cracking. Indentation produces a hydrostatic state of stress in the material. Hydrostatic stresses are known to cause plasticity to be the favored deformation mechanism. Because of this fundamental difference, the indentation experiments in this present work cause plastic deformation to occur at much lower temperatures than the work done previously. This explains the large shift in the BDT temperature.

Fracture Toughness

Fracture toughness was calculated from the room temperature indents using the methods described in the analytical procedures section of this report. The average fracture toughness of each sample is shown below in Table 6.2.

Table 6.2: Room temperature fracture toughness in un-doped samples

Un-doped samples	Sample 38	Sample 39	Sample 129	Sample 374
K_{IC} (MPa√m)	1.4 ± 0.1	1.36 ± 0.04	1.36 ± 0.04	1.69 ± 0.08

Samples 38, 39, and 129 all showed extremely similar values for fracture toughness. Sample 374, made with a different fabrication process, shows a higher fracture toughness than the rest. The results clearly indicate that the fabrication process used in Batch 3 is a large improvement over the process used in prior batches.

Yield Strength

Based on the study done by Giannakopolous [58], yield strength can be calculated from the plastic zone pile-up around an indent. The yield strength was calculated at various temperatures for Samples 129, 130, and 374. Unfortunately, yield strength data were not collected for Samples 38 and 39. Regardless, the data collected are sufficient for comparisons with the doped samples. In Figure 6.4 below, the yield strength data of the various samples is provided. There is fairly good agreement among all three samples.

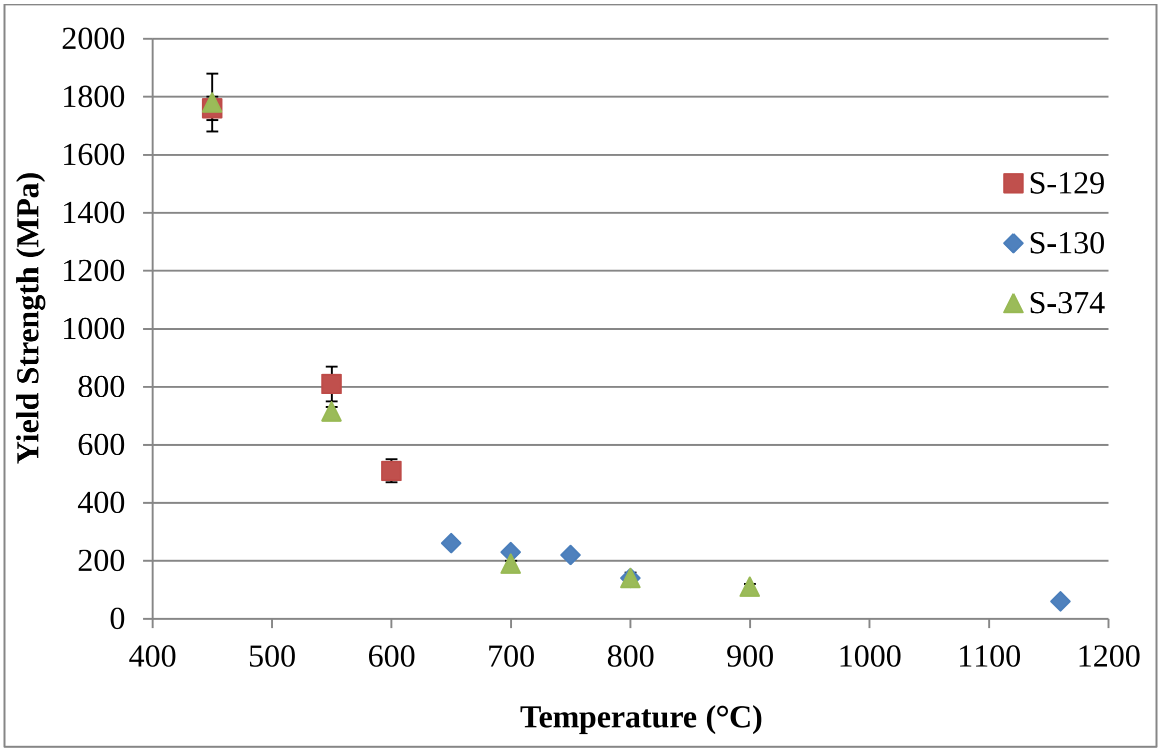

Figure 6.4: The average yield strength of several un-doped samples. Note that there is fairly good agreement among samples made using different fabrication processes.

Comparison with Literature Results

Before proceeding with the results of the doped samples, the results from the pure UO_2 samples should be compared with previously published results. As shown in the Literature Review, there is a large body of reputable data on the mechanical properties of un-doped UO_2.

A paper by Yamada [70] found the Vickers hardness of UO_2 with 8 – 10 µm grains and 14% porosity to be 4.6 ± 0.6 GPa. This research found the average Vickers hardness to range from 6.2 to 7.8 GPa. This difference is likely caused by the large difference in porosity. The Yamada work used samples with 14% porosity [70]. In the work presented here, the most porous un-doped sample was 6.19% porous, and showed an average Vickers hardness of 6.2 ± 0.4 GPa. Hardness is shown to decrease with increasing porosity, so the trend on hardness data collected here is consistent with the data presented by Yamada [70].

Yamada also calculated the fracture toughness in the 14% porous samples to be 1.1 ± 0.2 MPa√m [70]. The findings in this work found the fracture toughness to be consistent with a value around 1.4 ± 0.4 MPa√m, with Sample 374 being an outlier with higher fracture toughness. A paper by Kutty et al. [23] found fracture toughness to be dependent on porosity, and used large-load indents to create radial cracks that were evaluated using equations established by Anstis et al [24]. Kutty found fracture toughness to range from 0.88 to 1.20 MPa√m, depending on the porosity [23]. These values are likely lower due to the different cracking types in these indents. The present work saw only Palmqvist cracking from indentation, whereas Kutty reports only radial cracking [23].

Evans and Davidge [13] calculated the yield strength in UO_2 at temperatures from 650 °C to 1300 °C using three-point bend test experiments. Figure 6.5 show the results from this thesis in comparison to the results of Evans and Davidge. The values determined by Evans and Davidge are very similar to the data collected here using indentation. This indicates that there is good agreement between the different experimental methods.

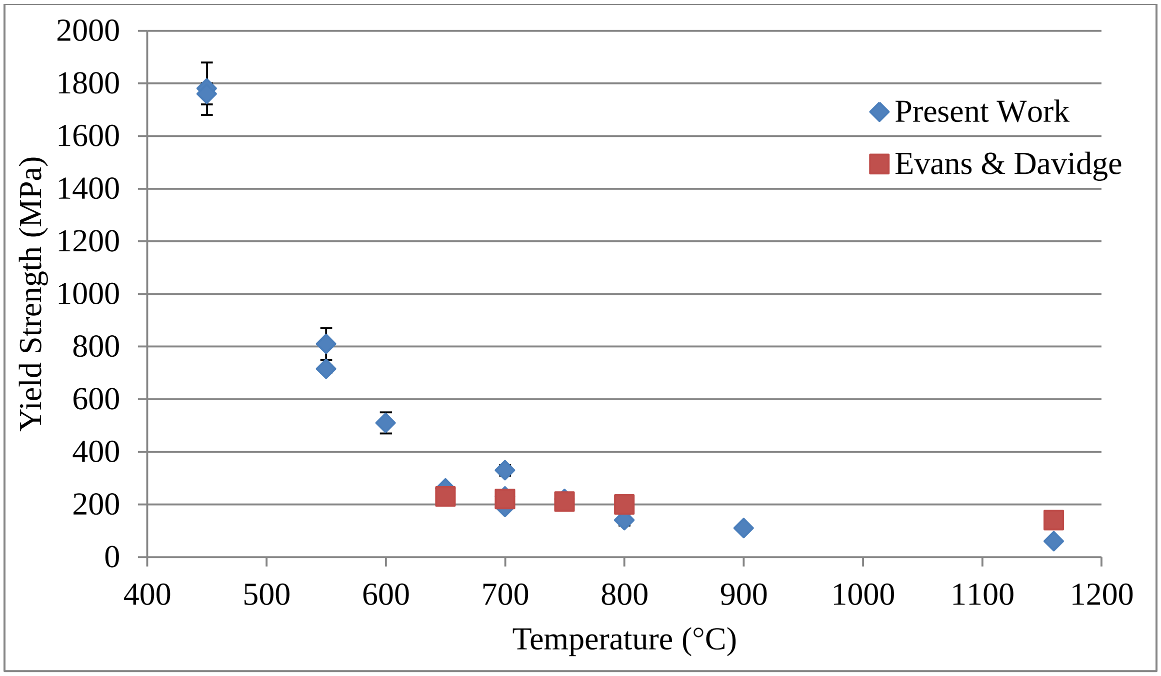

Figure 6.5: Comparison of yield strength data from the present work and research done by Evans and Davidge [5].

Now that the un-doped properties have been established and shown to fall in range with previously published results, it is possible to make comparisons between the doped samples and their un-doped counterparts. Moving forward, it is important to note which sample batch each doped sample came from, as that determines which un-doped sample it can be compared to. The results for each dopant type are covered individually, and a discussion section follows where each dopant is qualitatively ranked.

<u>Titanium Oxide Doping</u>

Two TiO_2-doped samples came in the first batch of samples sent by LANL. Sample 32 and Sample 33 contained 0.1 wt% TiO_2 and 0.2 wt% TiO_2, respectively. The un-doped samples from this batch were Samples 38 and 39. Information on the TiO_2-doped samples can be found in Table 6.3 below.

Table 6.3: Physical characteristics of the TiO_2-doped and un-doped samples.

Sample #	Dopant conc.	Density (g/cm^3)	% TD	Avg. grain diameter (µm)	Young's modulus (GPa)
S-32	0.1 wt% TiO_2	10.41	94.95	26.2	188
S-33	0.2 wt% TiO_2	10.41	94.97	27.9	189
S-38	Un-doped	10.72	97.78	11.1	205
S-39	Un-doped	10.58	96.55	N/A	198

Microstructure

The un-doped samples had an average grain diameter of approximately 11 µm, whereas Sample 32 (containing 0.1 wt% TiO_2) had an average grain diameter of 26.2 µm and Sample 33 (containing 0.2 wt% TiO_2) had an average of 27.9 µm. This massive increase in grain size in the doped samples was expected, as it is well established in the literature that TiO_2 will act as a sintering and grain coarsening aid for UO_2 [38, 39]. The IPF map of the Sample 33 microstructure is shown in Figure 6.6. The distorted diamond shape near the center of the IPF map is a Vickers indent. As stated previously, the area of the Vickers indent is partitioned out of the microstructural data in any quantitative analysis that is performed.

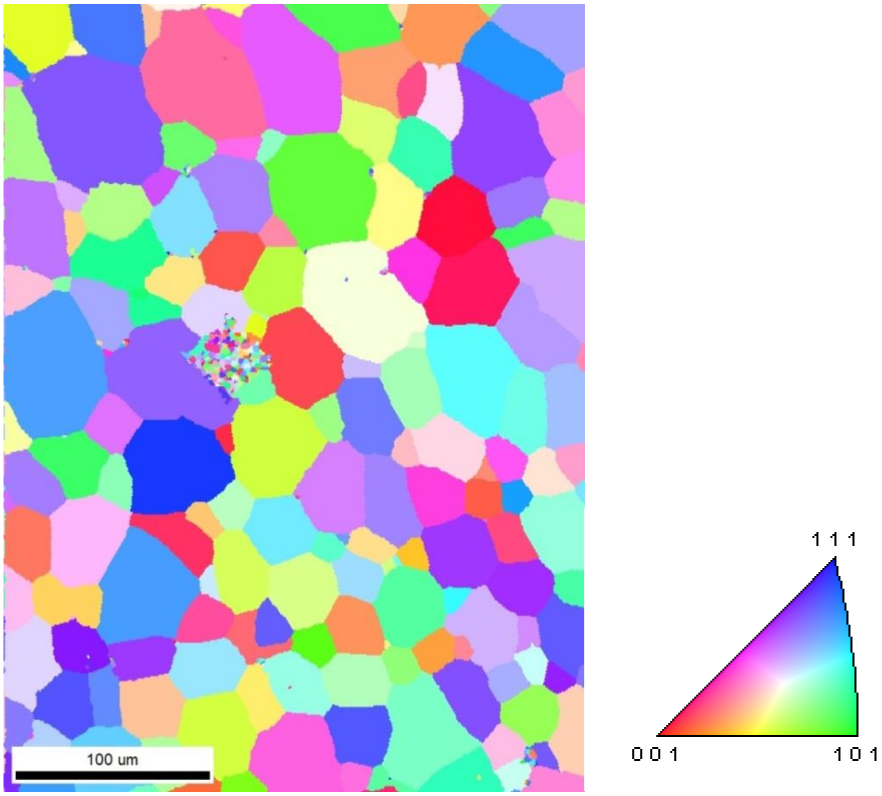

Figure 6.6: IPF map of Sample 33, containing 0.2 wt% TiO_2. Grain orientations are determined by the standard IPF triangle, shown to the right.

Chemical analysis of these samples revealed some highly interesting insights. By using EDS, it was discovered that the sample contained secondary phase domains rich in titanium oxide. These secondary phases were scattered throughout the microstructure, and there was not a perceived preference as to where the secondary phases would form. The secondary phases ranged in diameter from 1-10 µm, but were often found to be 1-3 µm in diameter. In Figure 6.7 below, a secondary electron image of the surface of Sample 33 is shown next to a titanium-concentration map. The bright green spots indicate a region of high titanium concentration. Looking closer at the secondary electron image shown on the left in Figure 6.7, one will notice that light-colored regions periodically exist within the central grain. These are caused by fluctuations in the titanium concentration within the grain. The darker regions have a higher concentration (~0.4 wt%), and the lighter regions have lower concentration (0.15-0.2 wt%).

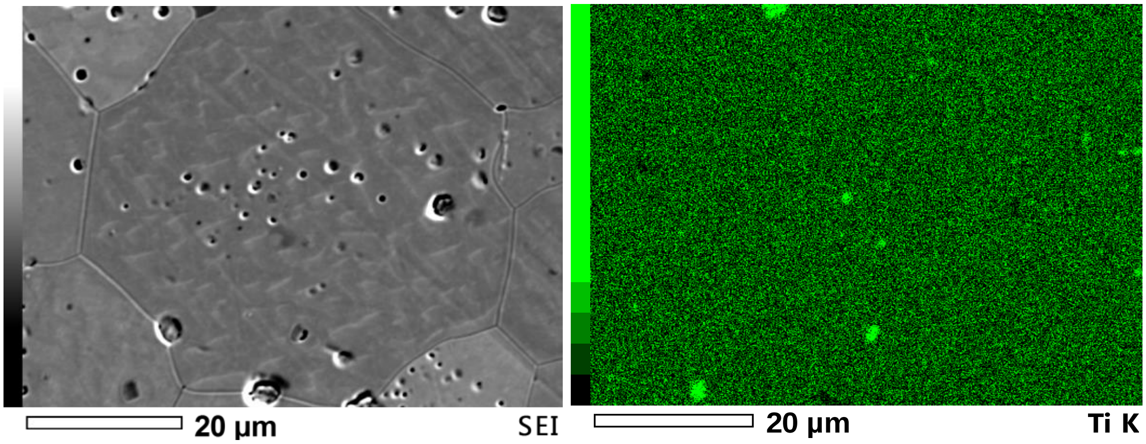

Figure 6.7: Left- Secondary electron image of Sample 33 surface.
Right- Ti-concentration map from EDS. Notice the dispersed secondary phases.

The TiO_2-rich secondary phases were seen numerous times in the path of cracks emanating from Vickers indents. In this event, the crack would almost always divert around the particle, rather than traverse through it. Therefore, the TiO_2-rich particles should lead to an increase in the fracture toughness. However, since the particles are so small, the effect of diverting the indentation crack is only marginal. An example of this effect is shown in Figure 6.8 below. This electron micrograph was taken at 20,000x magnification, and the TiO_2-rich particle is approximately 2 µm in diameter.

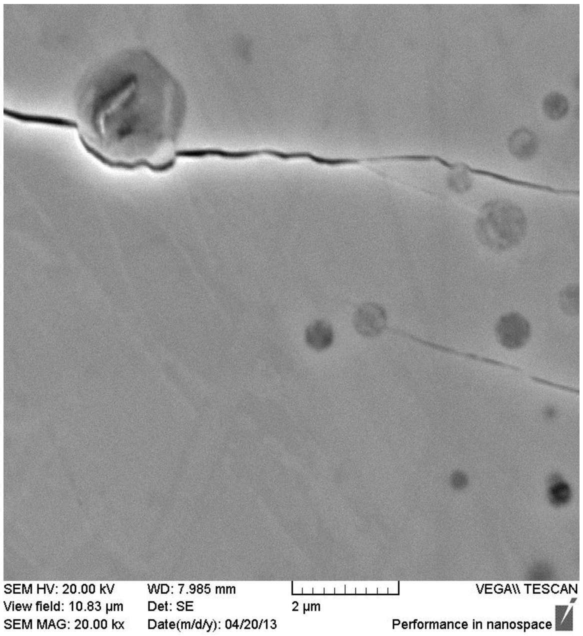

Figure 6.8: Indentation crack being deflected by Ti-rich particle at 20kx magnification.

Furthermore, from EDS analysis of Sample 33, it was revealed that the sample contained between 0.1 and 0.3 wt% Al_2O_3. Leckie and Luther reported similar results in their previous studies of fabricating doped-UO_2 specimens [60]. This is likely due to contamination during the fabrication process. The Al_2O_3 was found in greater concentrations within the TiO_2-rich phases, and only existed in minimal concentrations outside of the secondary phases. Beyond that, quantitative EDS consistently showed that Sample 33 contained 0.4 wt% TiO_2, twice the intended concentration of 0.2 wt%.

Hardness

The TiO_2-doped samples showed a higher material hardness than the un-doped samples across the entire temperature range. Table 6.4 gives Vickers hardness at 500, 800, and 1160 °C for the TiO_2-doped samples along with the un-doped samples from Batch 1.

Table 6.4:Vickers hardness for the TiO_2-doped samples.

Vickers Hardness (MPa)		20°C	500°C	800°C	1160°C
S-32	0.1 wt% TiO_2	7890	2410	1240	710
S-33	0.2 wt% TiO_2	8640	2010	---	730
S-38	Pure UO_2	7210	2060	570	350
S-39	Pure UO_2	6510	---	---	---

It is clear that by adding TiO_2 to the sample pellets, the hardness and grain size markedly increased. This result matches what was seen by Amato et al in 1966 [38]. Recall that the paper by Amato [38] established that the increased grain size in TiO_2-UO_2 specimens was a result of the titanium dioxide "lending" excess oxygen to the uranium oxide. This excess oxygen caused a large increase in the grain growth kinetics, and this led to larger grains overall.

Fracture Toughness

Fracture toughness was calculated in Sample 32 and Sample 33 at room temperature. The fracture toughness data (with the average deviation) is given in Table 6.5 on the following page.

Table 6.5: Room temperature fracture toughness of TiO_2-doped and un-doped samples.

Sample #	Dopant Conc.	KIC (20 °C) (MPa√m)
S-38	Un-doped	1.4 ± 0.1
S-39	Un-doped	1.36 ± 0.04
S-32	0.1 wt% TiO_2	1.4 ± 0.1
S-33	0.2 wt% TiO_2	1.40 ± 0.09

From the data presented in Table 6.5, it is clear that TiO_2-doping does not affect the fracture toughness significantly. The room temperature fracture toughness is identical for both un-doped and TiO_2-doped samples. So even though the inclusion of secondary phase particles should have theoretically increased the fracture toughness via local crack deflection, the effect does not seem to be substantial enough to make a difference at the macroscopic level.

Yield Strength

The addition of TiO_2 was found to significantly alter the yield strength of the material at high temperatures. In Sample 32, the yield strength was found to be roughly three times that of the un-doped sample. In Sample 33, it was nearly double. The yield strength data of Samples 32, 33 and 130 are presented in Figure 6.9.

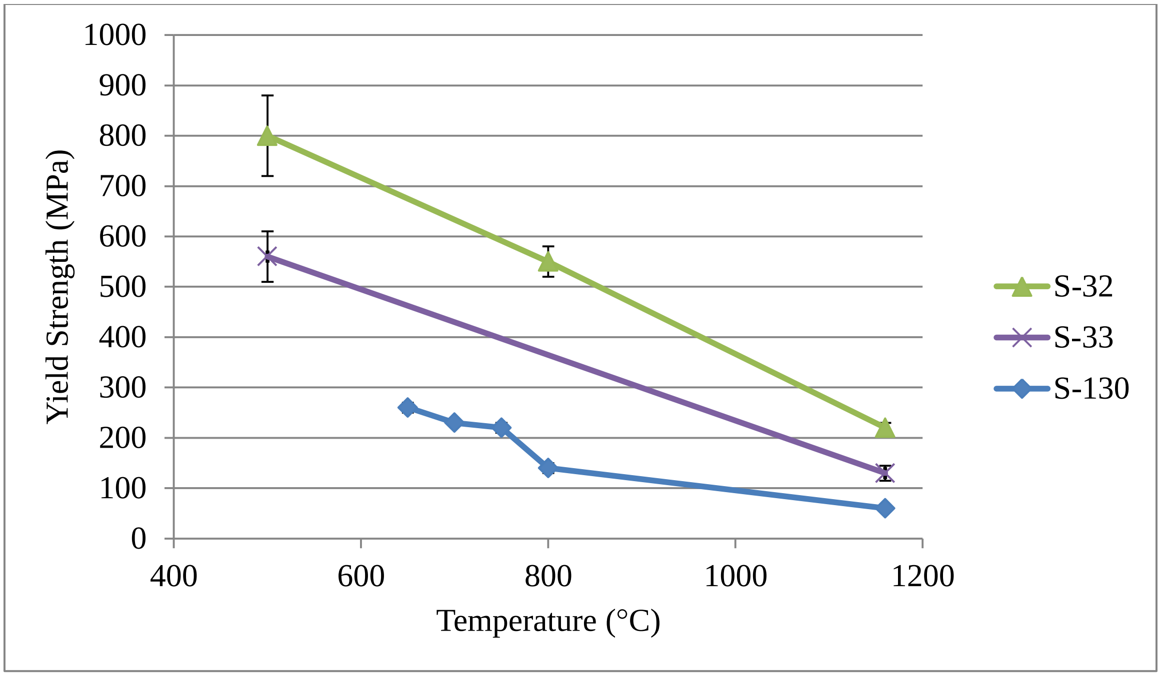

Figure 6.9: Yield strength measurements for Sample 32 (0.1 wt% TiO_2), Sample 33 (0.2 wt% TiO_2) and Sample 130 (pure UO_2).

While it is clear that doping with titanium oxide causes an increase in yield strength, it is interesting to note that the sample containing 0.1 wt% TiO_2 clearly shows a greater increase than the sample doped with 0.2 wt% TiO_2. It can be speculated that the lesser-doped sample shows higher yield strength because it has smaller, but more numerous, secondary phase particles dispersed within the matrix material. The dispersed secondary phases extrinsically increase the yield strength in a quasi-Hall-Petch mechanism, since dislocation motion is inhibited in the local volume around each secondary phase particle.

As Amato [38] previously reasoned for the mechanisms behind enhanced grain growth, the addition of TiO_2 may also influence the hardness of the sample by altering the sample's oxygen content. Hyperstoichiometric UO_2 has been shown to have a notably higher hardness than stoichiometric UO_2 [19], and this reasoning may explain why the TiO_2-doped samples have higher hardness values across the temperature range.

These results show that titanium oxide doping will greatly increase the grain size, make the material harder at all temperatures, have a neutral effect on the fracture toughness, and greatly increase the yield strength. Doping with titanium oxide has both an intrinsic and extrinsic effect on the properties; the dopant-rich secondary phases likely inhibit dislocation motion, which increases yield strength, while the dopant within the lattice “lends” oxygen to uranium oxide at high temperatures to drive the material into the hyperstoichiometric regime and cause a higher hardness.

Yttrium Oxide Doping

Two samples in Batch 1 were doped with Y_2O_3. Sample 34 and Sample 35 were doped with 0.05 wt% Y_2O_3 and 0.1 wt% Y_2O_3, respectively. Unlike the rest of the doped samples in this study, Y_2O_3 was added in smaller quantities to the specimens. Introducing less of this dopant was an interesting decision, from a manufacturing point of view, since research done by Christie [71] on enhancing the high-temperature plasticity of UO_2 through the addition of 0.5 wt% and 1.0 wt% Y_2O_3 concluded that the dopant was not present in sufficient quantities to cause a noticeable change in the mechanical properties.

Microstructure

Information on these two samples is provided in Table 6.6. The average grain diameters of the Y_2O_3-doped samples are very similar to the un-doped samples.

Table 6.6: Physical characteristics of the samples doped with Y_2O_3.

	Dopant conc.	Density (g/cm^3)	% TD	Avg. grain diameter (μm)	Young's modulus (GPa)
Sample 34	0.05 wt% Y_2O_3	10.63	97.01	N/A	201
Sample 35	0.1 wt% Y_2O_3	10.64	97.10	12.0	201

As with the other doped samples, EDS was used to analyze the chemistry of the Y_2O_3-doped specimens and investigate how the dopant may be dispersed throughout them. In Sample 34, only trace amounts of yttrium were found using EDS. From twenty-two individual point scans, only three picked up on the presence of yttrium. The average concentration of Y_2O_3 in Sample 34 was determined to be 0.03 wt% with a standard deviation of 0.01 wt%. This is somewhat close to the intended concentration of 0.05 wt% Y_2O_3. Interestingly enough, EDS analysis was unable to detect any yttrium in Sample 35. Figure 6.10 is an EDS spectrum taken from a map of the sample surface at 400X. The spectrum shows no sign of yttrium, but it does pick up a minor presence of both silicon (~1.74 keV) and aluminum (~1.49 keV). This analysis was repeated in three map scans and several point scans. The conclusion reached from EDS analysis is that yttrium may exist in Sample 35 at a concentration below the detectable limit (< 0.01 wt%).

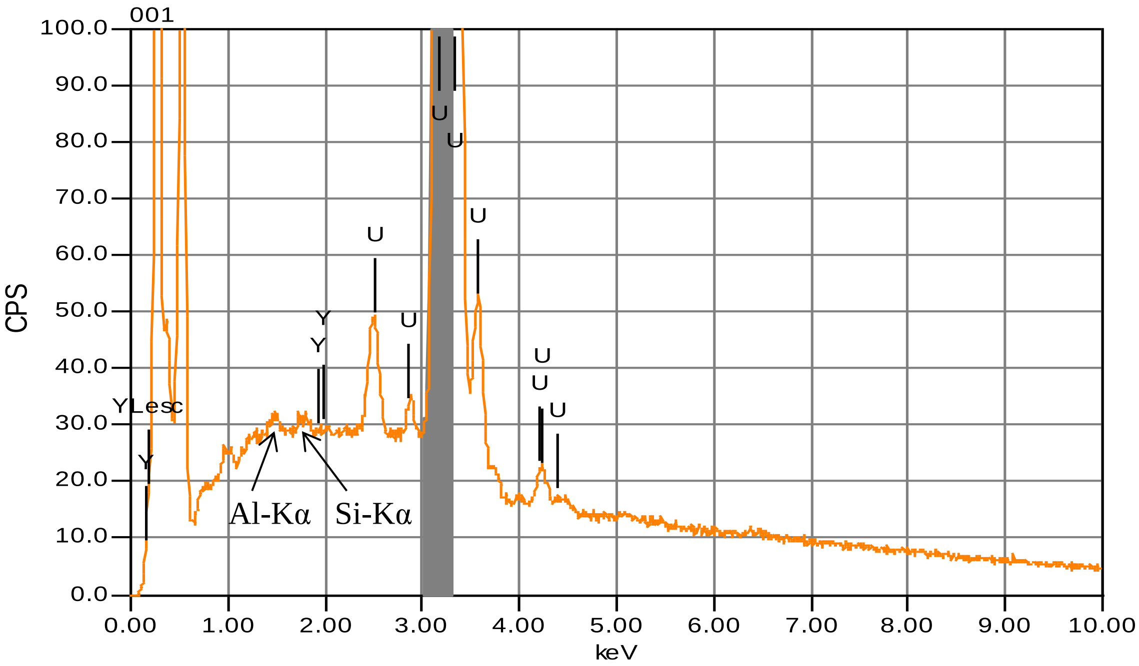

Figure 6.10: EDS spectrum of Sample 35. Note the two peaks corresponding to Al (1.49 keV) and Si (1.74 keV) being present in the sample.

Even though EDS did not provide any evidence that yttrium was present in these samples, hardness testing was still performed, because any differences in mechanical properties could potentially be attributed to low-concentrations of Y_2O_3-doping.

Hardness

The hardness of Sample 34 (0.05 wt% Y_2O_3) and Sample 35 (0.1 wt% Y_2O_3) can be compared with the un-doped samples fabricated using similar conditions: Sample 38, 39, 129, and 130. Sample 34 was tested at room temperature and a range of temperature between 500 °C and 1160 °C. Sample 35 was tested at room temperature, 450 °C and 550 °C. Results are presented in Figure 6.11, along with the un-doped sample hardness' for comparison.

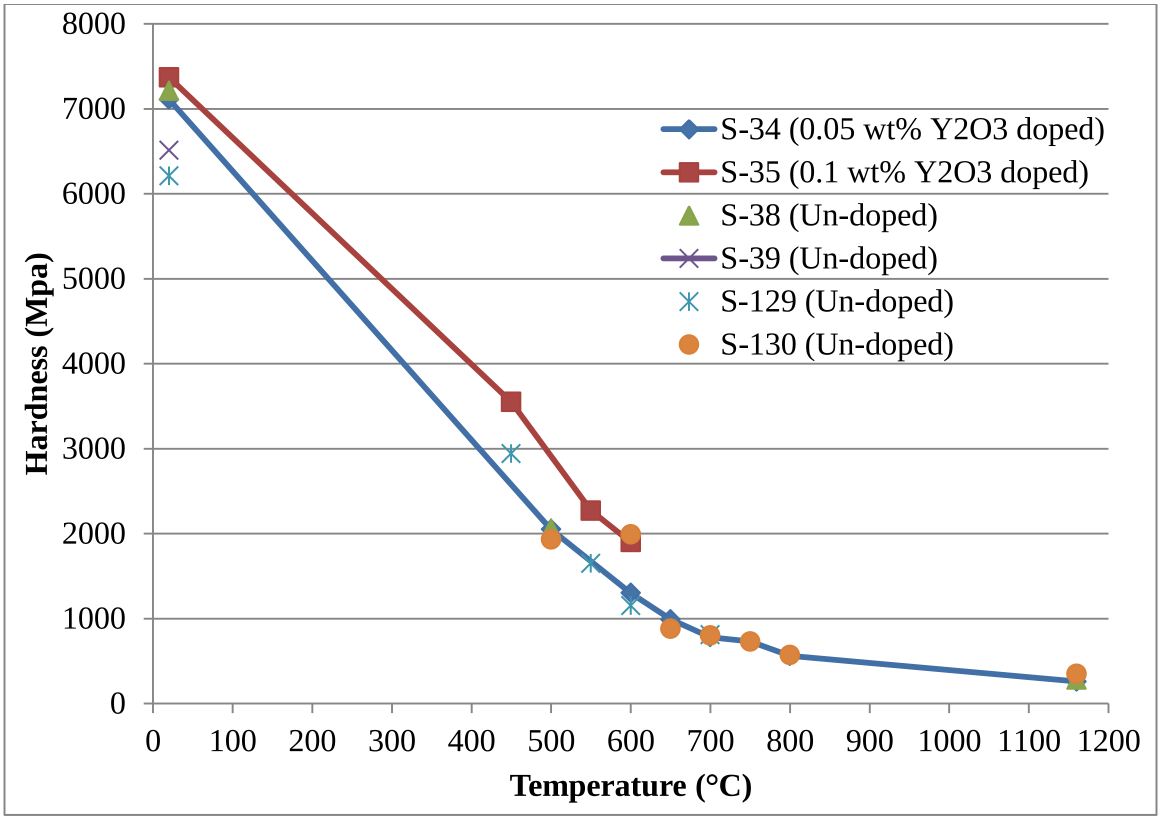

Figure 6.11: Results of hardness testing in yttria-doped samples compared to results from un-doped samples. Range of data extends from room temperature to 1160 °C.

For direct comparisons between the hardness in the doped samples and un-doped samples, it is best to look at the samples with the most similar densities. Thus, the Y_2O_3-doped samples are primarily compared to Sample 38, but Samples 129 and 130 are also used to supplement these findings. From Figure 6.11, it is clear that the hardness of the doped samples does not significantly differ from that of the un-doped samples. At room temperature, the hardness’ of Sample 34, 35 and 38 were all found to be equal within the margin of error. At the other end of the spectrum, the hardness’ of Sample 34 and Sample 38 at 1160 °C were also found to be extremely similar. In the rest of the elevated temperature range, the hardness data of Sample 34 is similar to Sample 130.

These findings reinforce the hypothesis that the samples only contain trace amounts of Y_2O_3. Previously published theoretical models by Belle [29] predict that adding sufficient quantities of yttrium oxide to uranium dioxide will effectively introduce Y^{3+} ions to the cation sites and therefore create a defective anionic lattice. Work done by Belle [29] on $U_{0.9}Y_{0.1}O_{1.98}$ showed that oxygen diffusion in this compound was much higher than oxygen diffusion in UO_{2+x}. An increase in the oxygen mobility can be attributed to defects in the anionic lattice. This was also hypothesized in a paper by Armstrong [72] where it was predicted that the Y^{3+} ions would enter the lattice as substitutional defects that were charge-compensated by the appropriate number of oxygen vacancy defects. A defective lattice will cause an increase in ductility, which would lead to a reduced hardness at high temperatures. Therefore, it is expected that doping with Y_2O_3 causes an intrinsic change in the lattice that introduces excess vacancies, thus lowering the hardness and yield strength.

While hardness testing in these experiments did not show any difference between un-doped and Y_2O_3-doped samples, it is still important to look at the fracture toughness, as it may highlight the effects of trace dopants.

Fracture Toughness

In Figure 6.12 below, fracture toughness for the Y_2O_3-doped samples and the un-doped samples is provided, with the error bars representing the average deviation. The fracture toughness values for the doped and un-doped samples were all equivalent within the error bars. Still, Sample 34, which showed trace amounts of Y_2O_3, showed a slight improvement in fracture toughness. While it is still within the error bars of Sample 38, it is outside of the error bars of Sample 39. This slight improvement may be attributed to the presence of Y_2O_3. As previously stated, the theoretical model by Belle predicted that the addition of yttrium oxide would improve the plasticity of UO_2, which should decrease the hardness and increase the fracture toughness [29]. Since this slight increase was seen in the sample containing definite trace amounts of Y_2O_3, yet not seen in the sample where EDS did not detect Y_2O_3, it is the opinion of the author that Y_2O_3-doping warrants further research with higher concentrations of the dopant.

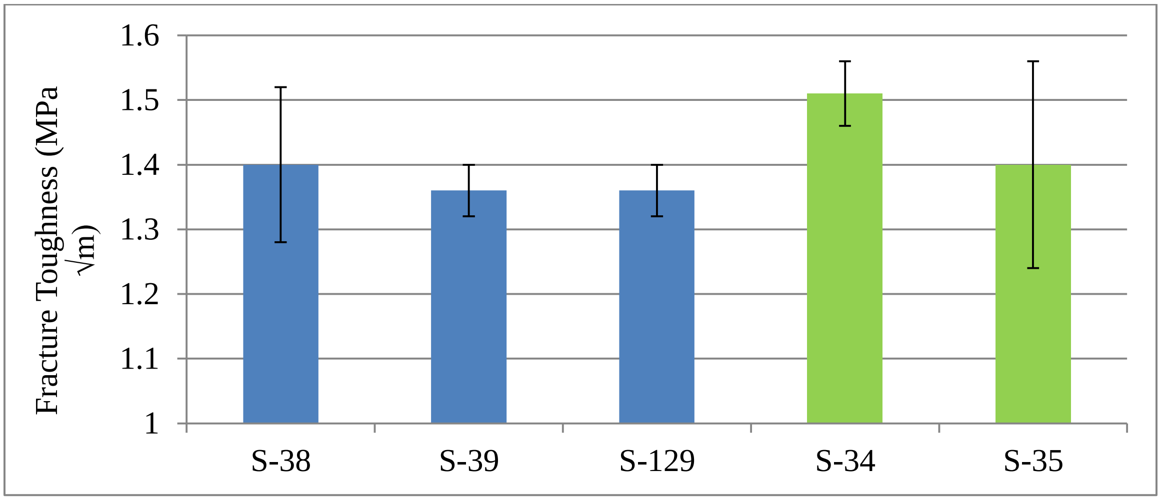

Figure 6.12: Average fracture toughness for the Y_2O_3-doped and un-doped samples.

Yield Strength

Yield strength data were only gathered for Sample 34 in the temperature range of 650-750 °C. In comparison to the un-doped Sample 130, Sample 34 exhibited a 30% decrease in yield strength. This limited data shows Y_2O_3-doping may have a positive impact on the yield strength of the material.

Aluminum Oxide Doping

Sample 372, doped with 0.2 wt% Al_2O_3, came with Batch 3. Recall here that the samples in Batch 3 were fabricated using a "wet" processing route, different than the samples in Batch 1 and 2. Thus, Sample 372 will be compared to the un-doped sample from Batch 3, Sample 374. Table 6.7 below lists the physical properties of Sample 372 and 374.

Table 6.7: Physical properties of the Al_2O_3-doped and un-doped sample from Batch 3.

	Dopant conc.	Density (g/cm^3)	% TD	Avg. grain diameter (µm)	Young's modulus (GPa)
Sample 372	0.2 wt% Al_2O_3	10.39	94.84	8.4	188
Sample 374	Un-doped	10.58	96.5	10.9	198

Sample 372 showed a relatively normal grain size distribution in the OIM scan. The average grain diameter was found to be 8.4 µm. The grain size distribution in Sample 372 is similar to the grain size distribution in Sample 374, but shifted to the left. In Figure 6.13, the grain size distribution for both samples is provided.

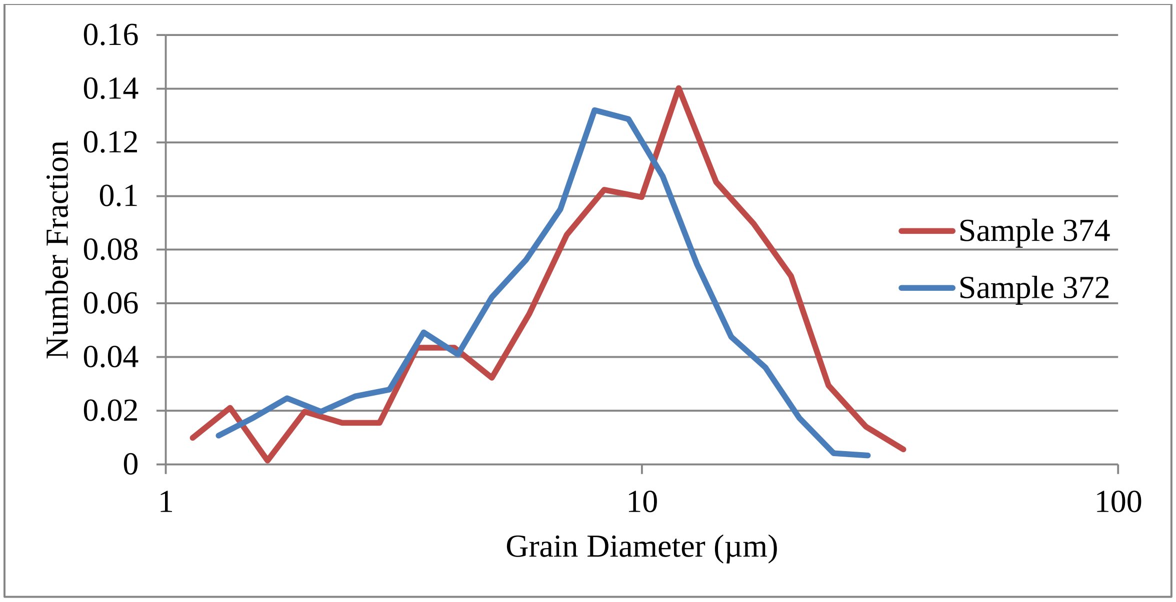

Figure 6.13: Histogram of grain diameters for S-372 (doped) and S-374 (un-doped).

From EDS analysis on Sample 372, it was discovered that Al_2O_3 formed secondary phases rich in the dopant. Similar to the TiO_2-doped sample, the secondary phases were randomly scattered throughout the sample and did not show any microstructural preference. Using quantitative EDS, it was determined that the secondary phases contained between 36-40 wt% Al_2O_3, with the balance being UO_2. The second-phase particles were between 2-5 µm in diameter. Figure 6.13 shows the EDS intensity map for the Al-Kα signal and the corresponding backscattered electron micrograph. The secondary phase regions are also easily detectable using the backscatter electron detector.

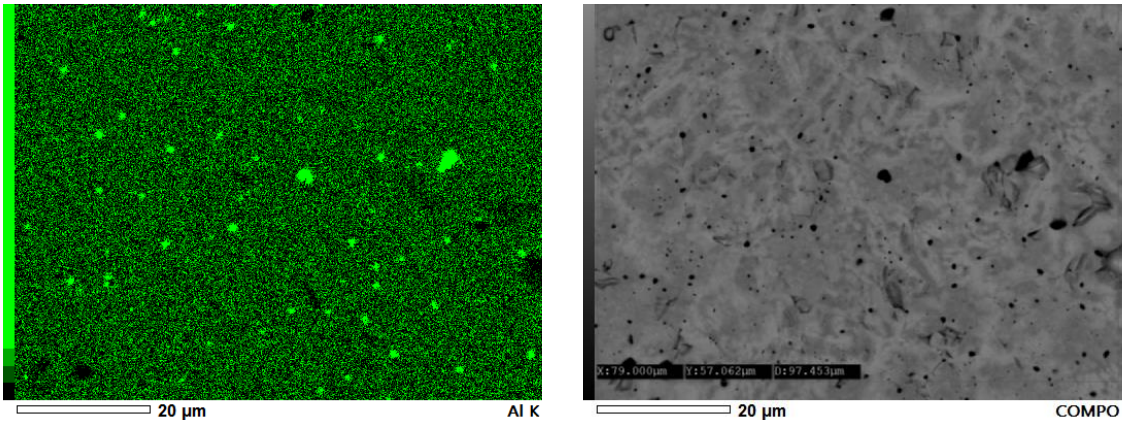

Figure 6.14: Left- Al-concentration map showing dispersed secondary phases rich in Al. Right- Backscatter electron image corresponding to the intensity map shown on left.

The smaller average grain size seen in the Al_2O_3-doped sample is likely caused by the scattered secondary phase regions. It is hypothesized that the secondary phases are effective in restricting grain boundary movement, thus reducing the overall grain growth seen during the sintering process.

Hardness

Room temperature indentation testing in the Al_2O_3-doped Sample 372 produced interesting results when compared with the un-doped Sample 374. The hardness of Sample 372 was found to be 7260 ± 240 MPa, which is lower than the hardness of Sample 374 (7820 ± 470 MPa). A lower hardness at room temperature is a positive indicator of improvements in fracture toughness and yield strength. Thus to build up the body of data for this sample, extensive high temperature testing was performed on Sample 372.

Sample 372 was tested at several temperatures between 450 °C and 950 °C. Figure 6.15 below shows a graph of hardness versus temperature for Samples 372 and 374. There was no significant change in the hardness for the Al_2O_3-doped Sample 372 compared to the un-doped Sample 374 in the elevated temperature range. Overall, this indicates a positive effect. The hardness at room temperature has been decreased, and the hardness at elevated temperatures is unaffected.

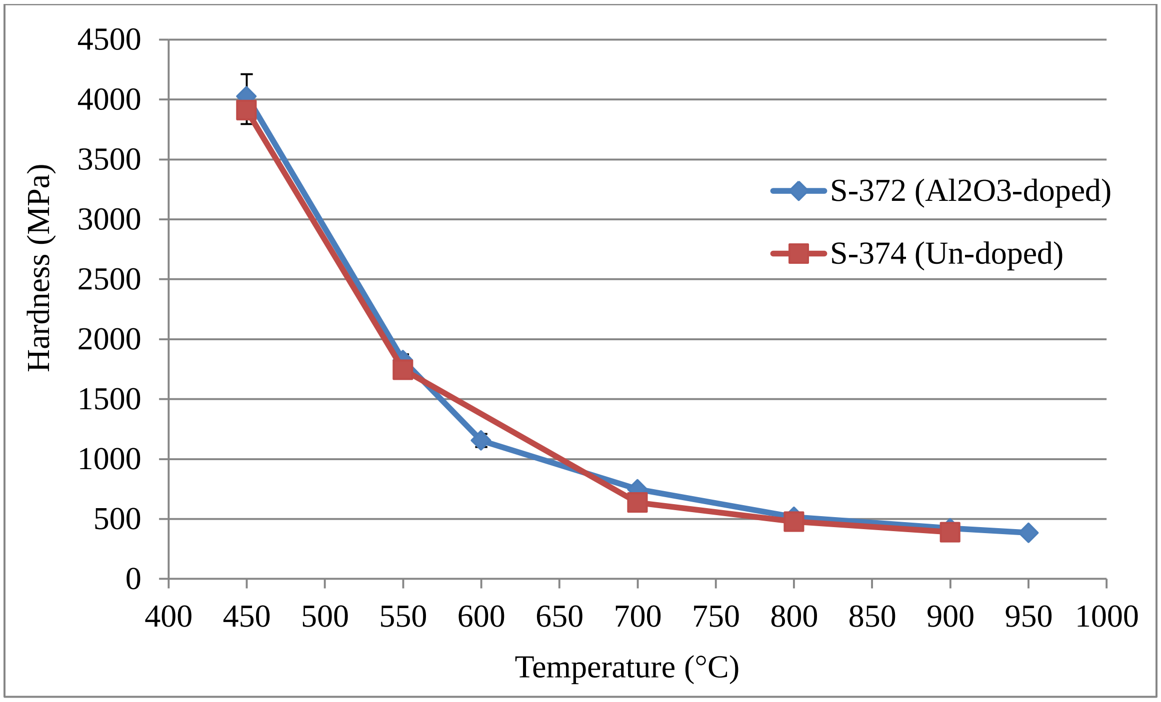

Figure 6.15: Comparisons of the average hardness in Sample 372 and Sample 374.

Even though the hardness at high temperatures was not affected from Al_2O_3-doping, the indentation experiments produced interesting results with respect to fracture toughness and yield strength.

Fracture Toughness

In comparison to the un-doped sample, Sample 372 showed an improvement in fracture toughness at room temperature. It was determined that Sample 374 had a fracture toughness of 1.69 ± 0.08 MPa√m, and Sample 372, doped with 0.2 wt% Al_2O_3, had a fracture toughness of 1.82 ± 0.08 MPa√m. This is a positive result, since an improved fracture toughness will reduce the risk of brittle fracture. Also recall that Sample 372 had a lower hardness than Sample 374 at room temperature. Therefore, Al_2O_3-doping has been shown to positively affect the room temperature mechanical properties of UO_2. In order to gauge how the dopant affects high temperature properties, it is necessary to look into the yield strength of the sample.

Yield Strength

For Sample 372, it was possible to calculate yield strength from indent pile-up at 700, 800, 900 and 950 °C. For comparison, this has also been done in Sample 374 at 700, 800, and 900 °C. The results for these two samples are plotted in Figure 6.16.

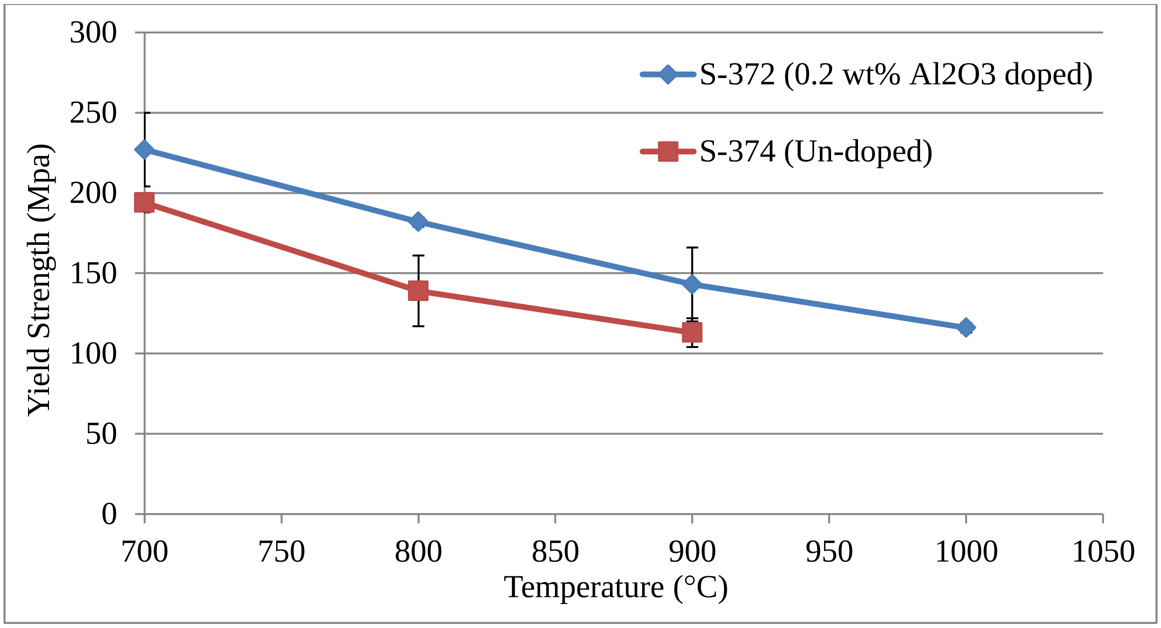

Figure 6.16: Comparisons of the average yield strength in Sample 372 and Sample 374.

Sample 372 shows higher yield strength than Sample 374 at all temperatures between 700 and 1000 °C. The difference here can be considered a 100 °C shift in the strength, meaning that the Al_2O_3-doped sample shows the same strength at 800 °C as the un-doped sample at 700 °C. The same goes for the strength at 900 °C in Sample 372 versus the strength in Sample 374 at 800 °C. Therefore, Al_2O_3-doping has been shown to strengthen the material at elevated temperatures.

The results presented here show that the doped sample is overall stronger due to the additions of Al_2O_3, exhibiting a higher fracture toughness and yield strength. The strengthening is likely a result of the dispersed secondary phase particles, which have been shown in other ceramics to cause material strengthening and toughening. This is an extrinsic effect of the dopant. As established by Kashibe [17], Al_2O_3 has a very minimal solubility in UO_2 so the only effect the dopant has on the properties must be caused by the dopant-rich secondary phases that it forms. This is unlike doping with TiO_2, since it is thought that TiO_2-doping produces both intrinsic and extrinsic changes in the material.

Silicon Dioxide Doping

Sample 373, containing 0.2 wt% SiO_2, came with Batch 3. Just as the Al_2O_3-doped sample above, this sample can be compared with the un-doped specimen, Sample 374. The physical characteristics of Sample 373 and Sample 374 are provided in Table 6.8 below.

Table 6.8: Physical properties of SiO_2-doped sample with Sample 374 for comparison.

Sample #	Dopant conc.	Density (g/cm^3)	% TD	Avg. grain diameter (µm)	Young's modulus (GPa)
373	0.2 wt% SiO_2	10.53	96.11	9.2	195
374	Un-doped	10.58	96.5	10.9	198

From EDS analysis of this sample, it was determined that both SiO_2 and Al_2O_3 are present in equal quantities. The EDS spectrum in Figure 6.17 illustrates the presence of both Al and Si within this sample. Quantitative analysis showed that both oxides are present in concentrations of 0.12 wt%. Using OIM, the average grain size in this sample was determined to be approximately 9.2 µm.

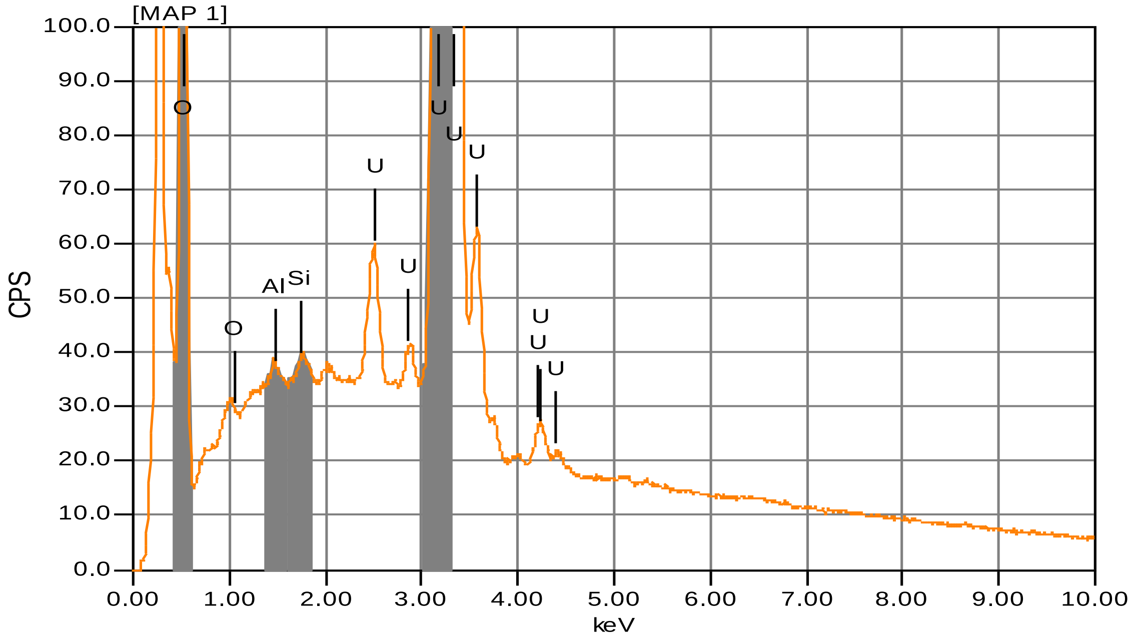

Figure 6.17: EDS spectrum showing the presence of Al in Sample 373.

Using EDS mapping, it was determined that the dopants are evenly distributed throughout the sample and no dopant-rich secondary phases were found. This is interesting, since it was seen in Sample 372 (containing 0.2 wt% Al_2O_3) that aluminum oxide preferred to form dopant-rich secondary phases. This may indicate that the aluminum and silicon oxides coexist as an Al-Si-O compound.

Hardness

The room temperature hardness in Sample 373, containing the aluminosilicate dopant, was lower than the hardness in un-doped Sample 374. The hardness of Sample 373 was determined to be 7230 ± 80 MPa, compared to 7820 ± 470 MPa for Sample 374. In the elevated temperature range, Sample 373 showed a slight increase in hardness. In Figure 6.18 below, the hardness values of both samples are compared.

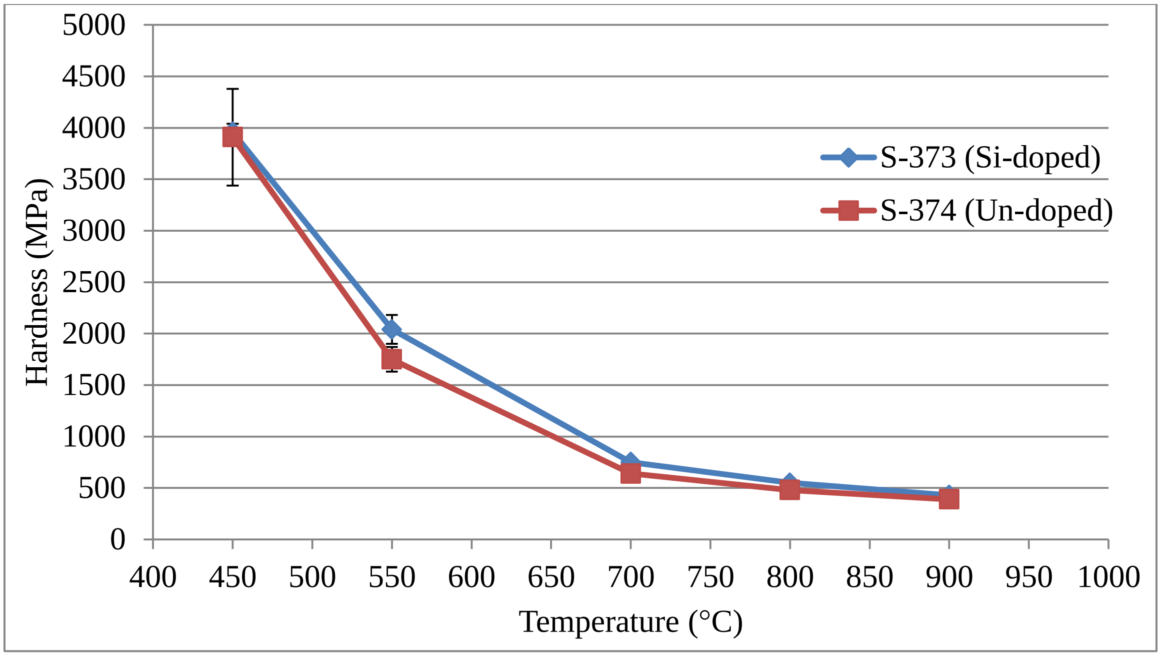

Figure 6.18: Average hardness for Sample 373 and 374 from 450-900 °C.

Even though the change in hardness is somewhat minor, the decrease in hardness at room temperature is still a positive indicator that the Sample 373 has improved mechanical properties. If prior trends hold true, the Sample 373 should exhibit higher fracture toughness than the un-doped sample at room temperature.

Fracture Toughness

From the room temperature indents, the fracture toughness of Sample 373 was extracted. As expected from the hardness measurements, the fracture toughness in the aluminosilicate-doped Sample 373 was higher than that of the un-doped Sample 374. Sample 373 had a fracture toughness of 1.95 ± 0.06 MPa, the highest fracture toughness seen in the samples so far. Recall that Sample 374 had a fracture toughness of 1.69 ± 0.08 MPa. This is a 15% improvement in the fracture toughness. Therefore, doping with Al-Si-O has been shown to strongly improve the fracture toughness of UO_2. It is speculated that the dopant could form into a glassy phase during the sintering process and improve the cohesion between adjacent grains. This would strengthen the intergranular forces and lead to strengthening on the macro-scale. The data collected from EDS did not show any signs of the dopant preferentially gathering at grain boundaries, but it would take analysis with transmission electron microscopy to conclusively determine whether or not that is the case.

Yield Strength

The high temperature indentation experiments also revealed how aluminosilicate-doping affects the yield strength of the material. In Figure 6.19, the yield strength of doped Sample 373 and un-doped Sample 374 are compared at temperatures between 450 °C and 900 °C.

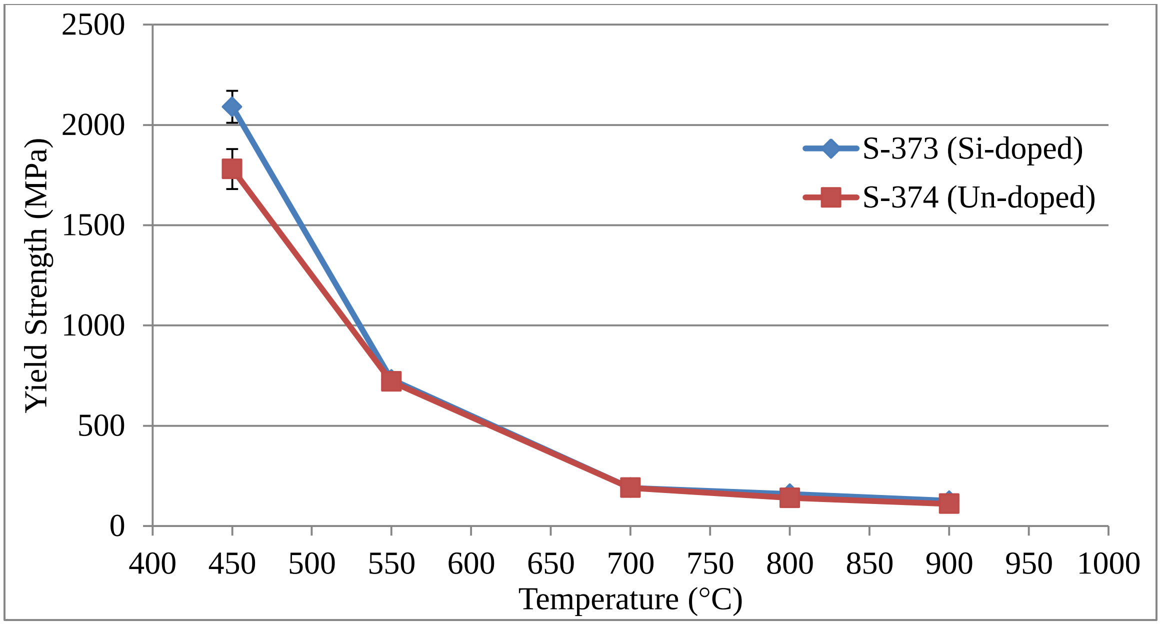

Figure 6.19: Average yield strength for S-373 and Sample 374 from 450 to 900 °C.

The doped sample (Sample 373) showed a higher yield strength than the un-doped sample at 450 °C, but held the same yield strength at the rest of the elevated temperatures. Even with the change in the 450-500 °C temperature range, the effect of the dopant on yield strength is considered to be generally neutral.

This sample showed an improvement in fracture toughness at room temperature and did not show a significant change in yield strength at elevated temperatures. It is suggested that the Al-Si-O dopant will form a liquid phase during sintering and improve the cohesion between grains at the grain boundaries. In a study on Xe diffusion through UO_2 doped with Al-Si-O [73], it was found using transmission electron microscopy that dislocations would inhomogenously accumulate at the grain boundaries of the doped specimens. Grain boundary strengthening may be the mechanism behind the increased fracture toughness in this doped sample.

<u>Chromium Oxide Doping</u>

Batch 3 also came with a sample doped with 0.2 wt% Cr_2O_3. Sample 371, doped with 0.2 wt% Cr_2O_3, had a density of 10.63 g/cm^3 which equates to a 97.02% TD. The average grain diameter was determined to be 9.6 µm. Recall that the average grain diameter in un-doped Sample 374 was 10.9 µm.

Microstructure

Figure 6.20 shows the grain diameter distribution for Samples 371 and 374. Notice that the distribution trend is similar, but Sample 371 is shifted to the left of Sample 374. Furthermore, where Sample 374 shows a large number of grains in the 10 –

12 µm range, Sample 371 has an even distribution of grains between a wider range of 8 – 11.5 µm. This is interesting, since doping with Cr_2O_3 has been shown in several papers to greatly enhance grain growth [16, 45]. Work done by Dugay [45] and Arborelius [16] found that UO_2 doped with 0.1 wt% Cr_2O_3 would consistently produce grains 5 – 7 times larger than grains in pure UO_2 samples, which is not the case here.

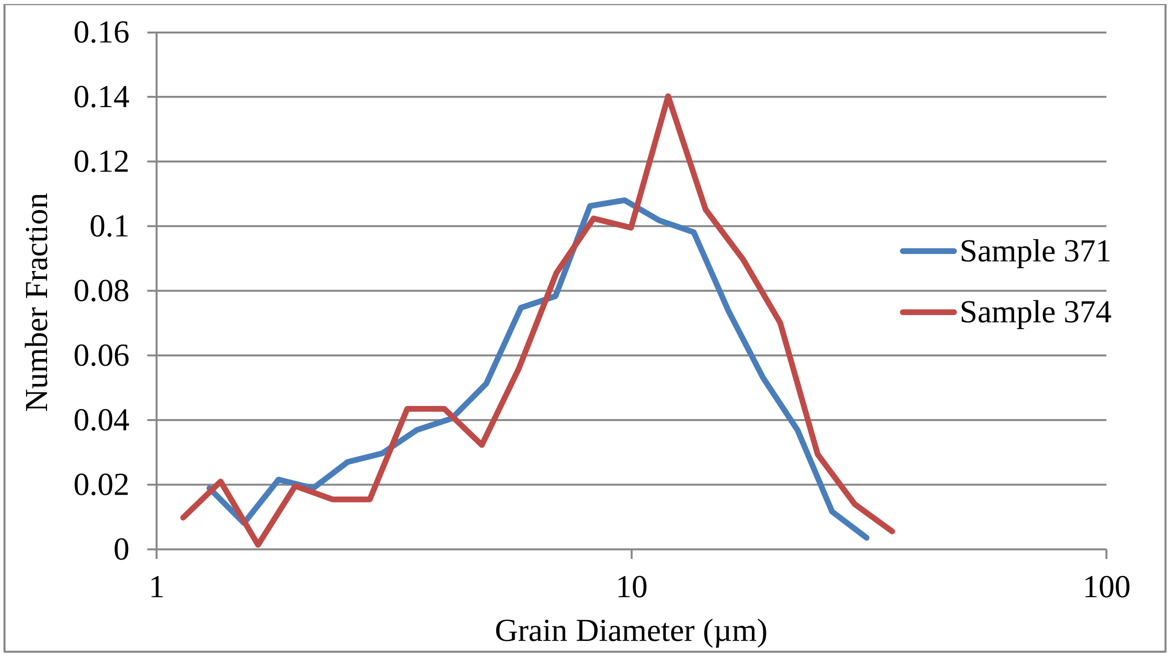

Figure 6.20: Histogram of grain diameters for un-doped sample (S-374) and Cr_2O_3-doped sample (S-371).

The EDS analysis of this sample revealed a couple interesting facts about the chemical make-up. The EDS spectrum from several different large area scans showed the presence of silicon and aluminum. Since these are the other two dopants used during the fabrication of this batch of samples, it is unsurprising to find these elements, and their presence may be a result of cross-contamination during fabrication. Quantitative EDS analysis also revealed that there is less Cr in this sample than expected. Analysis continually found 0.09-0.1 wt% Cr_2O_3 and up to 0.12 wt% of SiO_2 and Al_2O_3. From EDS mapping, it was also determined that there are no secondary phases present on the sample surface. The EDS results, coupled with the fact that the grain size was on the order of the un-doped samples, indicates that the aluminum, silicon, and chromium are interacting in a unique way, producing a sample different from what has been seen previously when just doping with Cr_2O_3.

Hardness

The average hardness in Sample 371 at room temperature was determined to be 8110 ± 430 MPa. This is higher than the average hardness in Sample 374 (7820 ± 470 MPa), but still within the margin of error. At elevated temperatures, Sample 371 generally showed a higher hardness than Sample 374 as well. The hardness data for these samples in the temperature range of 450 °C to 900 °C is plotted is Figure 6.21 below. Overall, this sample showed a more gradual reduction in hardness with respect to temperature.

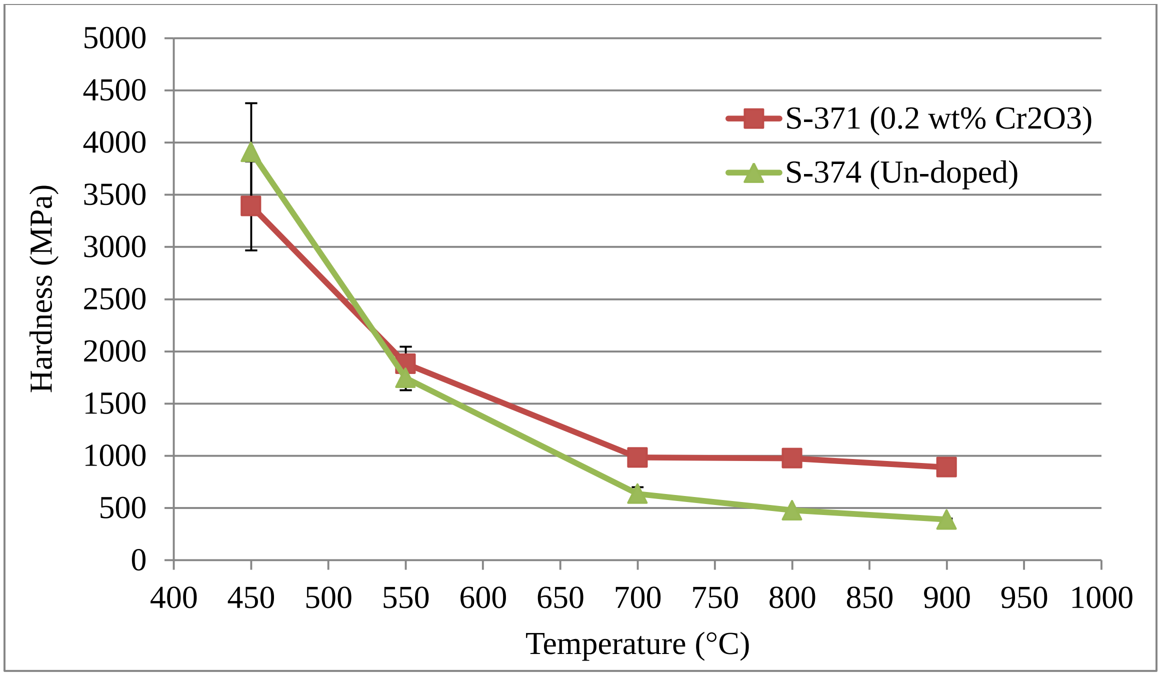

Figure 6.21: Average hardness for Sample 371 and 374 in elevated temperature range.

For a wide range of temperatures, Sample 371 showed a higher hardness than the un-doped sample. At room temperature, and from 550-900 °C, this was the case. Yet at 450 °C, the doped sample was softer than the un-doped sample. This is an interesting feature in the data, and more experiments in the temperature range of 400-500 °C would reveal more about this anomalous data point. A reduction in hardness at the lower range of elevated temperatures is very note-worthy, as it should indicate increased ductility in that temperature range.

Fracture Toughness

The room temperature fracture toughness in Sample 371 was marginally higher than that of Sample 374. From ten indents in Sample 371, the average fracture toughness was calculated to be 1.72 ± 0.05 MPa√m. Recall that the average fracture toughness in

Sample 374 was 1.69 ± 0.08 MPa√m. So there was a small increase in the average fracture toughness, yet it still falls within the error bars of the data.

Yield Strength

Sample 371 showed a very large change in the yield strength at high temperatures. Relative to the un-doped sample, the yield strength essentially doubled in the temperature range of 700 – 900 °C. Figure 6.22 illustrates the yield strength of both samples with respect to temperature.

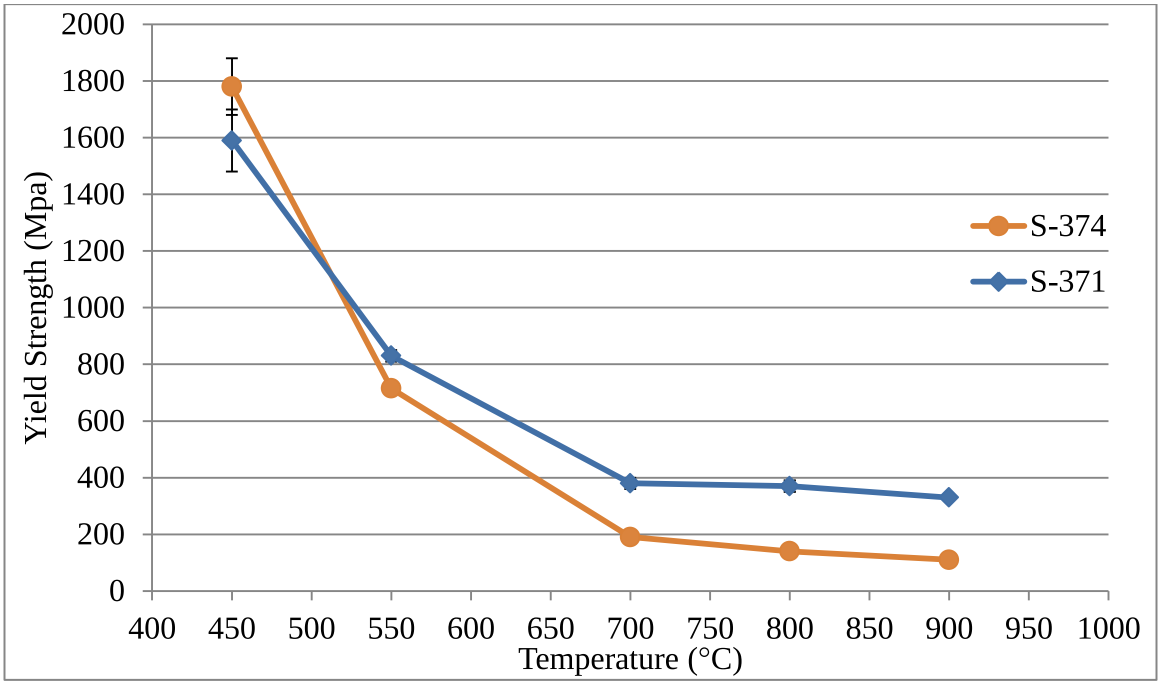

Figure 6.22: Average yield strength of Sample 371 (0.2 wt% Cr_2O_3) and 374 (un-doped) from 450 to 900 °C.

Doped Sample 371 retains its strength much better than un-doped Sample 374. Just as seen in the hardness data, Sample 371 behaves oddly at 450 °C. Just as it was shown in the hardness results, the yield strength in the doped sample at this temperature is lower than the un-doped sample. This could potentially indicate a physical change brought on by the dopant, such as a modified BDT temperature. It would be ideal to run the experiment again to confirm the anomalous behavior at this temperature.

The yield strength data for Sample 371 shows a mixed response to the dopants. At the low-temperature range, a decrease in yield strength indicates improved ductility. Yet at the high temperature range (>500 °C) the converse is shown to be true. Having a reduction in yield strength and hardness below 500 °C can be taken as a positive contribution because it would mean that a doped-UO_2 pellet, in reactor conditions, would have a softer outer edge more prone to deformation rather than cracking.

This sample and the sample doped with Al-Si-O contain similar dopants that likely form a glassy phase during sintering. Nevertheless, they exhibit unique and different mechanical properties. To determine how the “glassy phase” dopants are dispersed through the microstructure, whether it is an even dispersion through the lattice or possibly sub-micron precipitates at grain boundaries, one would have to use transmission electron microscopy.

Overall Discussion

By now, each doped sample has been individually compared with a corresponding pure UO_2 to determine how the dopant influences the different mechanical properties. To determine which dopant is best for improving the mechanical performance of UO_2, it is necessary to look back and summarize the results of this work.

The goal of this research was to find a dopant that led to an increase in fracture toughness at low temperatures. At elevated temperatures, the ideal dopant would result in a sample with decreased yield strength and increased ductility. So ultimately, the ideal doped sample would show increased fracture toughness at low temperatures, and higher ductility at high temperatures.

Titanium dioxide doping caused a massive increase in grain size in the samples. It also formed micron-sized secondary phases that were dispersed through the sample. At room temperature, the dopant did not affect the fracture toughness in the sample, as it was found to be effectively equal to that of the un-doped samples. Therefore, TiO_2-doping had a neutral effect on fracture toughness. At elevated temperatures, TiO_2-doping caused an increase in yield strength. In Sample 32, containing 0.1 wt% TiO_2, the yield strength was found to increase by a factor of 3. In Sample 33, containing 0.2 wt% TiO_2, the yield strength doubled. So TiO_2-doping had a negative effect on yield strength.

In the case of yttrium oxide doping, EDS results determined that insufficient amounts of yttium were even present in the samples. Unsurprisingly, these samples showed mechanical properties very similar to their un-doped counterparts. There was a slight improvement in the fracture toughness of Sample 34, containing approximately 0.02 wt% Y_2O_3. Since the dopant was not present in sufficient quantities, the work presented here cannot establish any substantiated conclusions as to how Y_2O_3-doping affects the mechanical performance of UO_2.

Doping with aluminum oxide resulted in a small improvement in fracture toughness at room temperature. At elevated temperatures, it led to a minor increase in the yield strength. An important note about this dopant is that it formed micron-sized secondary phases throughout the sample, similar to TiO_2-doping, but it did not greatly increase the average grain size. The secondary phase particles likely led to grain boundary pinning during sintering which restricted grain growth. The secondary phase particles likely play an influential role in increasing the fracture toughness. Increasing the density of the secondary phases could greatly improve the fracture toughness by leading to a high chance of crack deflection. Overall, doping with aluminum oxide had only a small positive effect on fracture toughness and a minor negative effect on yield strength.

The samples doped with SiO_2 were actually found to contain Si and Al. So in actuality, the results presented here are for samples doped with an aluminosilicate. This dopant was found to greatly increase the fracture toughness at room temperature. Of all the samples, this dopant led to the largest increase in fracture toughness. For yield strength at elevated temperatures, the dopant caused only a slight increase. The average yield strength in the doped sample was greater than that of the un-doped sample at some temperatures, yet it always fell within the range of error. Therefore, aluminosilicate doping had a neutral effect on yield strength, and a positive effect on fracture toughness.

The final sample examined in this research was the sample doped with chromium oxide. Using EDS analysis, it was determined that this sample actually contained approximately 0.1 wt% of chromium, and 0.12 wt% of aluminum and silicon. Even with the presence of aluminum and silicon, this sample only showed a minimal increase in fracture toughness at room temperature. This is interesting, since the sample containing Al-Si-O showed the greatest increase in fracture toughness. In some manner, the addition of chromium must be negating that effect. In the elevated temperature regime, doping with Al-Si-Cr-O led to a large increase in yield strength. At 450 °C the yield strength was reduced, but at temperatures greater than 500 °C, the yield strength was essentially doubled. Therefore, doping with Al-Si-Cr-O led to a slightly positive change in the fracture toughness and had mixed outcomes for yield strength.

Since TiO_2-doping was shown to negatively impact the mechanical performance, and the results of Y_2O_3-doping were found to be inconclusive, the three final samples are the only ones that warrant further discussion and investigation. Of these three samples, the results are very interesting to say the least. As it turned out, Sample 372 contained Al_2O_3, Sample 373 contained Al-Si-O, and Sample 371 contained a compound of Al-Si-Cr-O. Each sample exhibited very unique mechanical and material properties. To make a final decision on the best dopant (or combination of dopants) for improving the mechanical properties of UO_2, it is necessary to look at all of the facts presented in this thesis. In the conclusion chapter, the experimental results presented here and the findings presented in the literature review are all taken into account to determine the optimal dopant for improving the mechanical performance of uranium dioxide.

CHAPTER 7

CONCLUSION

Several conclusions can be drawn from the work presented in this thesis. In general, it is shown that the addition of oxide dopants to uranium oxide will strongly affect the microstructure and mechanical properties in different ways. Each dopant type studied in this work caused a unique change in the sample properties.

The results presented here indicate that the sample doped with aluminosilicate shows the largest change in properties useful for improving the mechanical performance of UO_2 in its application as nuclear fuel. This sample showed a 15% increase in the room temperature fracture toughness and the presence of the dopant did not negatively affect the yield strength.

Two of the dopants, TiO_2 and Al_2O_3, formed dispersed micron-sized secondary phase particles rich in each particular dopant. Both of these samples showed large increases in yield strength and significant increases in fracture toughness. From these results, it is hypothesized that the presence of secondary phase particles leads to strengthening in the doped uranium dioxide.

From the results on the samples doped with Al_2O_3, Al-Si-O, and Al-Si-Cr-O, it has been deduced that combining oxide dopants is likely to lead to binary and tertiary oxide compounds that show synergistic effects that differ from the effects of the individual oxide components. Adding Al-Si-O rather than Al_2O_3 removed the presence of micron-sized secondary phases. Doping with Al-Si-Cr-O produced a sample with physical and mechanical properties that significantly differ from properties seen in previous studies on UO_2 doped with Al-Cr-O [16]. In the final chapter of this thesis, a series of experiments are proposed to improve upon and drive forward this research effort.

CHAPTER 8

FUTURE WORK

The work presented in this thesis represents the beginning of a larger effort to improve the mechanical properties of UO_2. There are several aspects of this research that can be improved and expanded upon.

It is essential that new samples for future research are fabricated with better control over the dopant concentrations and better control over possible contaminants. In order to truly analyze the effects of dopants, it is necessary that the doped sample not contain significant amounts of any contaminants. For example, the Cr_2O_3-doped sample in this work actually contained higher concentrations of aluminum and silicon than it did chromium. Therefore, this work ultimately studied the effects of Al-Si-Cr-O and could not reach conclusions on the effects of Cr_2O_3 by itself. By improving the fabrication process, and establishing better consistency between samples, the results and analysis will be much more concrete and exact.

Furthermore, it is important to perform research similar to this body of work on samples solely doped with Cr_2O_3, SiO_2, and Y_2O_3. This research would help expand upon the body of knowledge in the realm of doping UO_2 and would ultimately lead to better educated decisions on doping research projects in the future.

It is in the opinion of the author that mixing other dopants will likely lead to interesting samples with other unique properties. Research of this type would expand the knowledge of doping in oxide materials by building an understanding of the way dopants interact and change material properties. In knowing this, and also knowing the individual effects of the dopants, it would be possible to establish a predictive basis for further advanced-doping research efforts.

WORKS CITED

[1] "World Uranium Mining Production," World Nuclear Association, July 2013. [Online]. Available: http://www.world-nuclear.org/info/Nuclear-Fuel-Cycle/Mining-of-Uranium/World-Uranium-Mining-Production/. [Accessed June 2014].

[2] "Nuclear Power in the World Today," April 2014. [Online]. Available: http://www.world-nuclear.org/info/Current-and-Future-Generation/Nuclear-Power-in-the-World-Today/. [Accessed June 2014].

[3] "Nuclear Power in the USA," World Nuclear Association, June 2014. [Online]. Available: http://www.world-nuclear.org/info/Country-Profiles/Countries-T-Z/USA--Nuclear-Power/. [Accessed June 2014].

[4] M. Luke, "The Breakthrough Institute," 3 September 2013. [Online]. Available: http://thebreakthrough.org/index.php/programs/energy-and-climate/nuclear-and-gas-account-for-most-carbon-displacement-since-1950/. [Accessed August 2014].

[5] "Power Reactors," United States Nuclear Regulatory Commission, December 2013. [Online]. Available: http://www.nrc.gov/reactors/power.html. [Accessed June 2014].

[6] "Nuclear Regulatory Commission," 29 March 2012. [Online]. Available: http://www.nrc.gov/reading-rm/basic-ref/students/animated-pwr.html. [Accessed June 2014].

[7] D. Olander, "Nuclear fuels - Present and future," *Journal of Nuclear Materials,* vol. 389, pp. 1-22, 2009.

[8] J. K. Shultis and R. Faw, "Nuclear Power," in *Fundamentals of Nuclear Science and Engineering,* p. 356.

[9] D. Banks, "Some observations of density and porosity changes in UO_2 fuel irradiated in water-cooled reactors," *Journal of Nuclear Materials,* vol. 54, pp. 97-107, 1974.

[10] D. Olander, Fundamental Aspects of Nuclear Reactor Fuel Elements, Oak Ridge: Technical Information Center, Office of Public Affairs, Energy Research and Development Administration, 1976.

[11] S. Phillpot, "Thermal Conductivity of UO_2 Fuel: Predicting Fuel Performance from

Simulation," *Journal of Materials,* vol. 63, no. 8, pp. 73-79, 2011.

[12] K. Edsinger, "LWR Pellet-Cladding Interactions: Material Solutions to SCC," *Journal of Materials*, vol. July, pp. 9-13, 2001.

[13] A. G. Evans and R. W. Davidge, "The Strength and Fracture of Stoichiometric Polycrystalline UO_2," *Journal of Nuclear Materials,* vol. 33, pp. 249-260, 1969.

[14] W. D. Kingery, Introduction to Ceramics, New York: John Wiley & Sons, Inc., 1976.

[15] I. Amato, R. L. Colombo and A. P. Balzari, "Grain growth in pure and titania-doped uranium dioxide," *Journal of Nuclear Materials,* vol. 18, pp. 252-260, 1966.

[16] J. Arborelius, "Advanced doped UO_2 pellets in LWR applications," *Journal of Nuclear Science and Technology,* vol. 43, no. 9, pp. 967-976, 2006.

[17] S. Kashibe and K. Une, "Effects of additives (Cr_2O_3, Al_2O_3, SiO_2, MgO) on diffusional release of 133-Xe from UO_2 fuels," *Journal of Nuclear Materials,* vol. 254, pp. 234-242, 1998.

[18] Y. Kim, "A thermodynamic evaluation of the U-O system from UO_2 to U_3O_8," *Journal of Nuclear Materials,* vol. 279, pp. 173-180, 2000.

[19] B. E. Schaner, "Metallographic determination of the UO_2-U_4O_9 phase diagram," *Journal of Nuclear Materials,* vol. 2, no. 2, pp. 110-120, 1960.

[20] N. Igata and K. Domoto, "Fracture stress and elastic modulus of uranium dioxide including excess oxygen," *Journal of Nuclear Materials,* vol. 45, pp. 317-322, 1972/73.

[21] C. Placek, "Uranium Dioxide Nuclear Fuel," Mallinckrodt Nuclear Corp., Hematite, Mo., 1960.

[22] H. Idriss, "Surface reactions of uranium oxide powder, thin films and single crystals," *Surface Science Reports,* vol. 65, pp. 67-109, 2010.

[23] T. Kutty, "Fracture toughness and fracture strength energy of sintered uranium dioxide fuel pellets," *Journal of Materials Science Letters,* vol. 6, pp. 260-262, 1987.

[24] G. R. Anstis, "A critical evaluation of indentation techniques for measuring fracture toughness: I, direct crack measurements," *Journal of American Ceramic Society,* vol. 64, no. 9, pp. 533-538, 1981.

[25] R. Warren, "Measurement of the fracture properties of brittle solids by Hertzian indentation," *Acta Metallurgica,* vol. 26, pp. 1759-1769, 1978.

[26] H. J. Matzke, T. Inoue and R. Warren, "The surface energy of UO_2 as determined by Hertzian indentation," *Journal of Nuclear Materials,* vol. 91, pp. 205-220, 1980.

[27] C. Ronchi, "Thermal conductivity of uranium dioxide up to 2900 K from simultaneous measurement of the heat capacity and thermal diffusivity," *Journal of Applied Physics,* vol. 85, no. 2, pp. 776-789, 1999.

[28] J. K. Fink, "Review: Thermophysical properties of uranium dioxide," *Journal of Nuclear Materials,* vol. 279, pp. 1-18, 2000.

[29] J. Belle, "Oxygen and uranium diffusion in uranium dioxide," *Journal of Nuclear Materials,* vol. 30, pp. 3-15, 1969.

[30] B. T. M. Willis, "Structures of UO_2, UO_{2+x} and U_4O_9 by neutron diffraction," *Journal de Physique France,* vol. 25, pp. 431-439, 1964.

[31] R. J. Thorn and G. H. Winslow, "Nonstoichiometry in uranium dioxide," *Journal of Chemical Physics,* vol. 44, no. 7, pp. 2632-2643, 1966.

[32] R. J. Thorn and G. H. Winslow, "Oxygen self-diffusion in uranium dioxide," *Journal of Chemical Physics,* vol. 44, no. 7, pp. 2822-2823, 1966.

[33] A. B. Lidiard, "Self-diffusion of uranium in UO_2," *Journal of Nuclear Materials,* vol. 19, no. 1, pp. 106-108, 1966.

[34] R. J. Hawkins and C. B. Alcock, "A study of cation diffusion in UO_{2+x} and ThO_2 using a-ray spectrometry," *Journal of Nuclear Materials,* vol. 26, pp. 112-122, 1968.

[35] H. J. Matzke, "Gas release mechanisms in UO_2 - a critical review," *Radiation Effects,* vol. 53, pp. 219-242, 1980.

[36] G. T. Lawrence, "A review of the diffusion coefficient of fission-product rare gases in uranium dioxide," *Journal of Nuclear Materials,* vol. 71, pp. 195-218, 1978.

[37] K. Une, I. Tanabe and M. Oguma, "Effects of additives and the oxygen potential on the fission gas diffusion in UO_2 fuel," *Journal of Nuclear Materials,* vol. 150, pp. 93-99, 1987.

[38] I. Amato, R. L. Colombo and A. P. Balzari, "Grain growth in pure and titania-doped uranium dioxide," *Journal of Nuclear Materials,* vol. 18, pp. 252-260, 1966.

[39] G. Arthur and D. Scott, "The effect of TiO_2 additions on the sintering of UO_2," *British Ceramic Society Transactions,* vol. 63, pp. 417-429, 1964.

[40] I. Amato, M. Ravizza and R. L. Colombo, "The effect of vanadium oxide additions on sintering and grain growth of uranium dioxide," *Journal of Nuclear Materials,* vol. 23, pp. 103-106, 1967.

[41] K. C. Radford and J. M. Pope, "UO_2 fuel pellet microstructure modification through impurity additions," *Journal of Nuclear Materials,* vol. 116, pp. 305-313, 1983.

[42] P. G. Klemens, "Thermal resistance due to point defects at high temperatures," *Physical Review,* vol. 119, no. 2, pp. 507-509, 1960.

[43] A. R. Massih, "Effects of additives on uranium dioxide fuel behavior," Swedish Radiation Safety Authority, Uppsala, Sweden, 2014.

[44] P. T. Sawbridge, G. L. Reynolds and B. Burton, "The creep of UO_2 fuel doped with Nb_2O_5," *Journal of Nuclear Materials,* vol. 97, pp. 300-308, 1981.

[45] C. Dugay, "High temperature mechanical tests performed on doped fuels," pp. 409-425, 1998.

[46] C. Nonon, "PCI behaviour of chromium oxide doped fuel," in *International Seminar on Pellet-Clad Interaction in Water Reactor Fuels,* Provence, France, 2004.

[47] Y. W. Rhee, "Effect of SiO_2-CaO-Cr_2O_3 on the creep property of uranium dioxide," *Nuclear Engineering and Technology,* vol. 37, pp. 287-292, 2005.

[48] J. Matsunaga, "Fundamentals of GNF Al-Si-O additive fuel," in *Proceeds of Top Fuel,* Paris, France, 2009.

[49] K. Niihara, R. Morena and D. Hasselman, "Evaluation of K_{IC} of brittle solids by the indentation method with low crack-to-indent ratios," *Journal of Materials Science*

Letters, vol. 1, pp. 13-16, 1982.

[50] S. Palmqvist, "Indentation hardness and fracture toughness in single crystal," *Jernkontorets Ann,* pp. 300-306, 1957.

[51] A. G. Evans and E. A. Charles, "Fracture toughness determinations by indentation," *Journal of the American Ceramic Society,* vol. 59, no. 7-8, pp. 371-372, 1976.

[52] J. Lankford, "Indentation microfracture in the Palmqvist crack regime: implications for fracture toughness evaluation by the indentation method," *Journal of Materials Science Letters,* vol. 1, pp. 493-495, 1982.

[53] R. Dukino and M. Swain, "Comparative measurement of indentation fracture toughness with Berkovich and Vickers indenters," *Journal of the American Ceramic Society,* vol. 75, no. 12, pp. 3299-3304, 1992.

[54] M. T. Laugier, "Palmqvist indentation toughness in WC-Co composites," *Journal of Materials Science Letters,* vol. 6, pp. 897-900, 1987.

[55] F. Ouchterlony, "Stress intensity factors for the expansion loaded star crack," *Engineering Fracture Mechanics,* vol. 8, pp. 447-448, 1976.

[56] D. Tabor, "A simple theory of static and dynamic hardness," *Proceedings of the Royal Society of London,* vol. 192, no. 1029, pp. 247-274, 1948.

[57] K. L. Johnson, "The correlation of indentation experiments," *Journal of the Mechanics and Physics of Solids,* vol. 18, pp. 115-126, 1970.

[58] A. Giannakopoulos, P. Larsson and R. Vestergaard, "Analysis of Vickers indentation," *International Journal of Solids Structures,* vol. 31, no. 19, pp. 2679-2708, 1994.

[59] J. Cahoon, W. Broughton and A. Kutzak, "The determination of yield strength from hardness measurements," *Metallurgical Transactions,* vol. 2, no. 7, pp. 1979-1983, 1971.

[60] R. Leckie and E. Luther, "Report on controlling the microstructure of UO_2 pellets," Los Alamos National Lab, Los Alamos, NM, 2012.

[61] A. Schwartz, M. Kumar and B. Adams, Electron Backscatter Diffraction in

Materials Science, New York, NY: Kluwer Academic/Plenum Publishers, 2000.

[62] "ASTM Standard E112, 2013. "Test Methods for Determining Average Grain Size"," ASTM International, West Conshohocken, PA, 2013.

[63] J. Wheeler and J. Michler, "Indenter materials for high temperature nanoindentation," *Review of Scientific Instruments,* vol. 84, pp. 1-11, 2013.

[64] "ASTM Standard C1237, 2008, "Standard Test Method for Vickers Indentation Hardness of Advanced Ceramics"," ASTM International, West Conshohocken, PA, 2008.

[65] R. L. Smith and G. E. Sandland, "An accurate method of determining the hardness of metals, with particular reference to those of a high degree of hardness," in *Proceedings of the Institution of Mechanical Engineers*, 1922.

[66] P. L. Larsson and A. E. Giannakopolous, "Analysis of Berkovich indentation," *International Journal of Solids Structures,* vol. 33, no. 2, pp. 221-248, 1996.

[67] M. M. Khrushchov and E. S. Berkovich, "Methods of determining the hardness of very hard materials: the hardness of diamond," *Industrial Diamond Review,* vol. 11, pp. 2-49, 1951.

[68] W. C. Oliver and G. M. Pharr, "An improved technique for determining hardness and elastic modulus using load and displacement sensing indentation experiments," *Journal of Materials Research,* vol. 7, no. 6, pp. 1564-1583, 1992.

[69] C. R. Tottle, "Mechanical properties of uranium compounds," National Bureau of Standards, Springfield, VA, 1965.

[70] K. Yamada, S. Yamanaka and M. Katsura, "Mechanical properties of (U,Ce)O_2," *Journal of Alloys and Compounds,* pp. 697-701, 1998.

[71] G. Christie and J. Williams, "The effect of small additions of yttria on the plasticity of uranium oxides at 940 C," *Journal of Nuclear Materials,* vol. 5, no. 1, pp. 1-4, 1962.

[72] W. M. Armstrong and W. R. Irvine, "Creep of urania base solid solutions," *Journal of Nuclear Materials,* vol. 12, no. 3, pp. 261-270, 1964.

[73] K. Une, "Rim structure formation and high burnup fuel behavior of large-grained UO_2 fuels," *Journal of Nuclear Materials*, vol. 278, pp. 54-63, 2000.

APPENDIX A

RADIOACTIVE SAMPLE POLISHING PROCEDURE

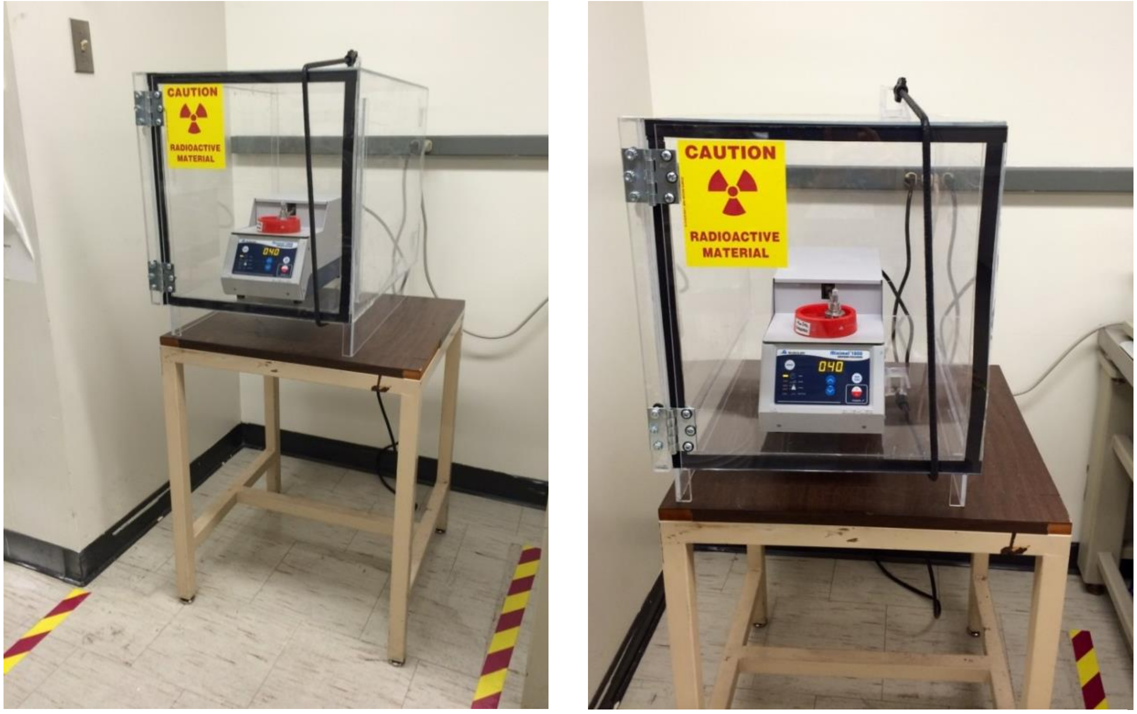

Figure A.1: Radioactive sample polishing containment box located in ERC-368.

Read instructions fully and thoroughly prior to starting any polishing. Do not leave polishing unattended. This procedure assumes the user has some knowledge of polishing guidelines. The Pace Technologies Metallographic Handbook is the recommended reference for polishing. Record your polishing steps and any notes in the Minimet Polishing Procedures notebook.

Preparing your workstation

1) Prepare everything that you may need for this procedure prior to starting the polisher.
2) Each polishing step requires: the proper polishing pad, a clean glass back, a clean polishing tray.
3) Polishing pads must be cut down to size (4 Minimet pads per large Pace pad)
4) Prep each polishing step: pad on glass, glass in tray. Trays are labeled.
5) Keep 2-3 spare glass backings and trays on hand with extras of each polishing pad.

6) Stack clean trays in order of use.
7) You will need a cleaning station. Place sheets in order from bottom to top: Versi-dry lab soaker spill-proof sheet, yellow treated dusting cloth, SPC green absorbent pad, large kimwipe.
8) You will need strong tweezers for removing the polishing pads from the glass backing.
9) You will need to a 4” x 4” square of spill-proof sheet and green absorbent pad for each polishing step. These are used when removing the glass backing from the polishing tray after each step.
10) You will need at least two 1-gallon bags for waste disposal. Fold the bags appropriately. Place a smaller bag in the polishing containment box. Keep extra smaller bags available near the workstation.
11) You will change gloves after cleaning each tray. Use well-fitting gloves. Keep extras nearby.
12) Cut a green pad into small squares. I cut them into a variety of sizes. These will be used to clean the polishing trays; some will absorb the polishing suspension, others will wipe out the remaining liquid and clean the glass backings.
13) Have Fantastik, de-ionized water and acetone on hand in the workstation. Have small and large Kimwipes in the workstation. Have cotton-tipped applicators in the workstation.

Preparing the sample

1) Prior to doing any polishing work, carefully weigh the sample that is to be polished. Record the mass prior to polishing. This will be used later to calculated the total activity removed.
2) For polishing, the sample must be mounted to an aluminum stub using Crystalbond. Make sure the stub fits in the polishing fixture because some do not fit.
3) Place the aluminum mounting piece on the hot tray and place the aluminum stub on the mounting piece.

4) Heat the hot tray to 150 deg. C.
5) Check the temp. on the top of the stub. It must exceed 130 °C for the Crystalbond to melt.
6) Press the Crystalbond against the stub to form a thick layer of melted Crystalbond.
7) Place the sample in the center of the aluminum stub, in the liquid Crystalbond.
8) Using a small folded-up Kimwipe, push down on the sample so that it sinks into the adhesive.
9) Use tongs to remove the mounting piece from the hot plate so that it may cool.
10) Wait for the Crystalbond to crystallize before removing the stub from the mounting piece.
11) Ensure that the sample is strongly secured to the stub.

Minimet sample polishing

1) With the sample secured to the stub and the workstation prepared, you are now able to polish.
2) Set a 3x5 inch green pad on top of the Minimet and place a small Kimwipe on top of that. This will be where you place the polishing piece between steps.
3) At the workstation, secure the sample stub into the polishing piece.
4) Adjust the sample surface to be just above the bottom of the polishing piece.
5) Set the first polishing tray in the Minimet.
6) Spray the pad with polishing solution and ample water (if necessary). The pad MUST be wetted. Note: Do not use water on colloidal silica steps, as it lowers the pH and can crystallize the silica.
7) Place the rest of the polishing trays in a nearby location.
8) Place polishing piece on polishing rod and secure the polishing piece to the Minimet.
9) Set your desired settings.
10) Press START and close containment door. Latch the door with the bungee cord.
11) Watch sample polishing to make sure it is going correctly.

12) Wearing clean gloves? Scan them and check.
13) After polishing time runs out, un-latch and open containment door.
14) Unscrew and remove the polishing piece. Rinse it off thoroughly with DI water. Ensure that the DI water is dripping into the polishing tray, not onto the Minimet.
15) On colloidal silica steps, use cotton applicators or small Kimwipes to wipe down the surfaces. Use Kimwipes to dry it all off.
16) Gently place the polishing piece on Kimwipe/green pad on top of Minimet.
17) Remove and set the dirty polishing tray at work station.
18) Use small green absorbent pads to soak up the water and polishing solution in the tray. Get as much as possible. Tip the polishing tray to retrieve any solution stuck behind the glass backing.
19) Carefully flip the polishing tray onto a green pad with the spill-proof sheet beneath it.
20) Clean off the edge and rim of the tray, then spray the inside of the tray with Fantastik and set it aside.
21) Wipe down the back side of the glass backing. Be careful with what you touch. The goal is to keep both hands clean, so use Kimwipes to protect your hands whenever possible. Clean the back with Fantastik.
22) Use a small Kimwipe to grab the glass backing and use tweezers to remove the polishing pad.
23) Dispose of the polishing pad, the green pad, and the spill-proof backing.
24) Place the glass backing on a small Kimwipe and clean both sides and the edges. Make sure to clean the notch in the glass backing.
25) Scan the glass backing with the radiation detector to make sure it is clean, and put it aside.
26) Clean the tweezers.
27) Soak up the Fantastik in the polishing tray and fully clean it out.
28) Scan it with the radiation detector before putting it aside with the glass backing.
29) Switch gloves.
30) Check your hands and forearms.

31) Place the next polishing tray in the Minimet.
32) Return to Step 5 and repeat the process.

Polishing clean-up

1) After completing the polishing process, you must clean the Minimet, the workstation, and the polishing piece.
2) Start with the polishing piece. Bring it to your workstation.
3) Use a cotton swab to hold it in place, wipe everything down. Be thorough.
4) Use small allen key to remove the sample stub.
5) Set the sample stub aside for now.
6) With cotton swabs and small Kimwipes, use acetone to thoroughly clean the polishing piece.
7) Scan the polishing piece after cleaning and set it aside.
8) Use acetone on a cotton swab to clean the sample and the stub. Acetone dissolves Crystalbond.
9) You may want to check the sample surface before removing it from the stub.
10) Place the stub in a small dish with acetone and soak it to remove the sample.
11) Use a green pad square and a Kimwipe with Fantastik to clean the top and sides of the Minimet.
12) Wipe down the containment box as well and use Rad-Wipe Smears to survey it. I survey the top, the polishing tray area, and the front of the Minimet, as well as the containment door.
13) Remove the sample from the stub and store the clean sample.
14) Clean the sample stub and scan it.
15) Soak up the acetone and properly dispose of all your waste.
16) Remove your gloves last and seal up the waste bags. Dispose of these.
17) Scan your hands, forearms, and body. Wash your hands and wrists with soap and water.
18) Carefully weigh the sample and calculate the total mass removed due to polishing.

19) Log the outcome of the polishing and calculate the total activity removed. Record the activity removed on the waste bucket and in the radiation safety information binder. To calculate the total activity removed, see paragraph below.
20) Double-check your working area and make sure everything is properly put away.

If necessary, the wide-field binocular microscope should be used to check sample surfaces between polishing steps. It is ideal to minimize the number of times the sample needs to be removed from the containment box. Check the sample surface quality before deciding that the polishing is finished.

The sample trays must remain wet during polishing. It is necessary that you keep a close eye on the polisher to ensure that it stays wet, the polishing pad does not rip or tear, and the polishing piece does not come loose.

Calculating activity removed

After polishing is completed, it is required to determine the amount of material removed and calculate the total activity (mCi) removed during polishing. The best way to determine this is to calculate the total mass removed during polishing. Therefore it is essential to weigh the sample before and after polishing. With that information, multiply the mass by 14.8 Bq/mg and then convert this to mCi (1 Bq = 2.7*10-8 mCi).

If you did not measure the sample weight prior to polishing, there is an alternative method that can be used to calculate the activity removed. The rule-of-thumb used here is that each polishing step removes a thickness of material equivalent to two times the size of the abrasive. So, the 3 µm diamond suspension would remove 6 µm from the thickness, and the 0.02 µm colloidal silica would remove 0.04 µm. Add up the sum total of the thickness removed and multiply it by the cylindrical area of the sample to get the total volume removed. Multiply this value by the theoretical density of UO_2 (10.96 g/cm3), and then by the %TD of the particular sample to get the total mass removed. To determine the activity removed from the given mass, multiply the mass by 14.8 Bq/mg and then convert this to mCi (1 Bq = 2.7*10-8 mCi).

The activity (in mCi) needs to be recorded on the appropriate page in the radiation safety information binder, as well as on the appropriate waste bucket log.